SAPIENZA
UNIVERSITÀ DI ROMA

Synthesis and characterization of novel hybrid perovskites featuring quaternary organoammonium cations with extended conjugation

PhD in Chemical Sciences

XXXV cycle

Supervisor

Dr. Andrea D'Annibale

Candidate

Lorenza Romagnoli

Table of contents

Abstract

The last decade has seen an unprecedented interest in hybrid metal halide perovskites semiconductors, as active layers in photovoltaic cells, with extraordinarily high efficiency values achieved, and for various different optoelectronic applications, especially light emission and radiation detection.

In fact, these materials have the advantage of being synthesized from affordable precursors by solution techniques, and of allowing a fine tuning of their photophysical properties through the modification of their composition. Regretfully, their utilization on a large scale is still hindered by their poor environmental stability, owed to the ammonium cations contained in them, which undergo hydrolysis reactions in the presence of water; for this reason, the main goal of the current research in the field of hybrid perovskites is represented by the improvement of their tolerance to moisture and other environmental agents (such as high temperature and O_2).

The aim of this work was therefore the study of the possibility to enhance perovskite stability and performances, through the introduction of novel organic cations featuring the following characteristics: an extendedly conjugated structure, in order to modulate the optoelectronic properties of the materials, and the absence of hydrolysable protons, to avoid decomposition in the presence of moisture.

In particular, the synthesis and characterization of two novel water-insensitive and thermally stable hybrid metal halide perovskites, containing 4,4′-(anthracene-9,10-diylbis(ethyne-2,1-diyl))bis(1-methyl-1-pyridinium), $(C_{30}H_{22}N_2)^{2+}$ cation, is described in Chapters 3 and 4. The two materials, both of which showed intense photoluminescence, were prepared using different metals, lead in the first case and bismuth in the second, with the aim of exploring the possibility of replacing a toxic element such as lead (which is however the most frequently used metal in hybrid perovskites) with a safer alternative.

Moreover, the synthesis of a series of additional environmentally stable lead-based and bismuth-based hybrid materials, sharing the presence of quaternary conjugated bipyridinium cations is described in Chapter 5, together with a preliminary evaluation of their potentialities for applications.

Chapter 1: Introduction

1.1 Hybrid materials

The need for functional materials possessing unique characteristics, specifically tailored for the most disparate technological applications, has since long led to the idea of combining already existing substances, thus taking advantage of their individual properties, to create the so-called hybrid materials, featuring properties between those of the precursors or resulting in completely different ones.[1,2,3]

In fact, the approach of mixing different components, typically an organic and an inorganic one, is not anything new: human beings have been doing this for centuries, for example to obtain paints, and there are also some natural materials which can be regarded as hybrid, since they are constituted by organic and inorganic components intimately merged, such as bones and nacre. However, the development of new synthetic procedures, especially the sol-gel process,[4,5] studied since the early twentieth century and fully exploited from the middle of the century, and characterization techniques for both organic and inorganic materials, paved the way to the blossoming of a myriad of new hybrid compounds.[6,7]

As regards the existing types of hybrids, a first, broad difference can be recognized between nanocomposites and actual hybrid materials: although there is no sharp demarcation, the first term is generally used when one of the constituents has at least one dimension in the nanometer range,[8] and typically under 100 nm; when, in turn, molecular species are used to form *in situ* one of the units, especially the inorganic one, the denomination "hybrid materials" is most often applied. A further classification can be made on the basis of the interaction between the components: in some cases, the organic and the inorganic compounds are held together, at least in a certain degree, by covalent or ionic bonds, while there are many others in which the different species are only linked through weaker interactions, such as hydrogen bonds, van der Waals forces or π-π interactions.[9] Clearly, since the strength and the character of the interactions change in a continuous way, the distinction between the two types is not so strictly defined.

Given the extraordinary, and always increasing, variety of existing hybrid materials, it is impossible to provide a comprehensive list of them; however, among the most known

examples there are organoclays,[10,11] polymer-clay nanocomposites,[12] organic derivatives of silica,[13,14] polysilsesquioxanes,[15] polyoxometalate-polymer adducts,[16] mixed organic-inorganic polymers.[17,18] These examples of hybrid materials are represented schematically in **Figure 1.1**.

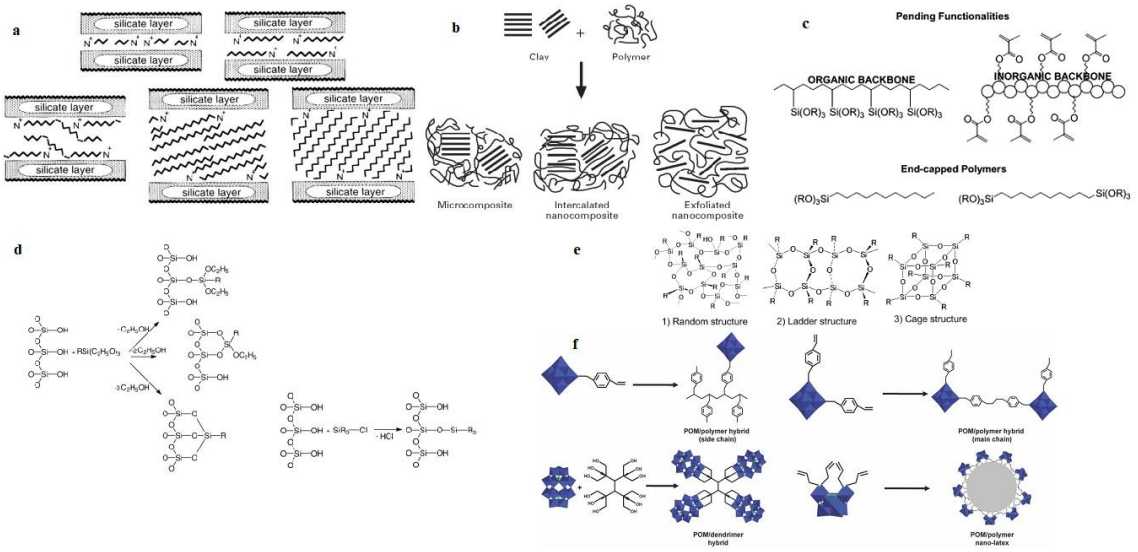

Figure 1.1 Different types of hybrid materials: a) organoclays; b) polymer-clay nanocomposites; c) organic-inorganic polymers; d) organically modified silica; e) polysilsesquioxanes; f) polyoxometalate-polymer adducts.

Similarly, because of the immense heterogeneity of this field, it is almost impossible to enumerate all of the possible applications of hybrid materials. It is important to note, however, that there are structural and functional materials: while the first are mainly synthesized and employed for their mechanical properties, the so-called "functional hybrid materials", which are currently the most studied ones, possess very different applications, among which there are catalysis, membranes, dyes, sorbents, electronic and optoelectronic devices.

1.2 Hybrid perovskites

Among the many functional materials that have recently come forth in this scenery, a prominent role is certainly held by hybrid perovskites, that is, organic-inorganic hybrids,

formed by transition or post-transition metal halides and organic cations, possessing a perovskite-type structure, represented in **Figure 1.2**, or a related one.

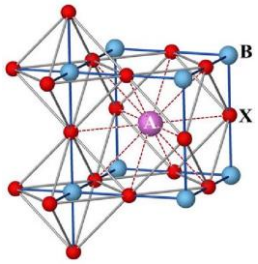

Figure 1.2 Perovskite crystal structure.

Differently from host-guest hybrids, in which organic molecules are intercalated in a preordered inorganic structure, which is little influenced by their presence, sharing the inorganic framework (host) and the organic species (guest) only weak interactions, these compounds are characterized by strong ionic bonds between the organic ions and the inorganic components. Organic-inorganic perovskites are, in fact, ionic crystals, featuring precise composition and ratio between the two constituents and a strong dependence on the organic cation, both of the crystal structure and of the physical properties.[19,20]

Hybrid perovskites have many interesting and useful photophysical properties and, as such, are very promising candidates for a variety of optoelectronic and energy applications:[21,22] indeed, the attention raised by this type of materials spans from solar cells[23,24,25] to light emitting devices,[26,27] from lasers[28,29] to radiation detectors,[30] so they are currently one of the most studied classes of hybrid semiconductor materials.

As regards photovoltaic applications, by far the most popular ones, since the first hybrid lead halide perovskite was embedded in a solar cell, in 2009,[31] this new type of cells has experienced a remarkable growth in the obtained values of power conversion efficiency (PCE), that is, the fraction of solar radiation which can be converted into electricity, from 3.8% for the first methylammonium lead iodide solar cell to the latest certified value of 25.7%,[32] so perovskite solar cells are currently the fastest-progressing emerging photovoltaic technology, as **Figure 1.3** shows.[33,34]

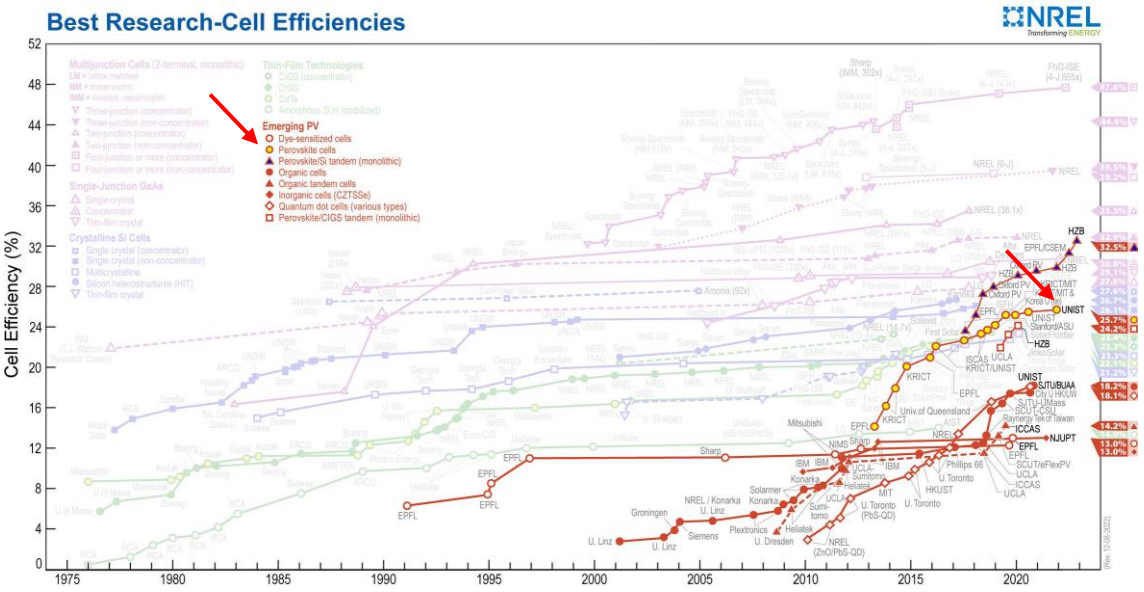

Figure 1.3 Progress in PCE values for emerging photovoltaics; values for perovskite solar cells are indicated by the red arrow.

1.2.1 Perovskite structure and composition

The name "perovskite", with which these compounds are identified, comes from the name of the mineral $CaTiO_3$ and has become a general term for all-inorganic or hybrid organic-inorganic materials described by the formula ABX_3, where A and B are two cations, A being larger than B, and X is an anion. In a proper perovskite crystal, every B cation is octahedrally coordinated to six X anions, while A cations, residing in the cavities between the octahedra, are surrounded by twelve B cations in a cuboctahedral symmetry, as shown previously in **Figure 1.2**.[35]

Although the ideal structure is cubic, most synthetic perovskites, in addition to many naturally occurring ones, adopt lower symmetry crystal structures, due to relative A and B size, which do not satisfy the so-called "tolerance factor" *t*, defined as:

$$t = \frac{(R_A + R_X)}{\sqrt{2}(R_B + R_X)} \quad (1)$$

R_A, R_B and R_x in the formula represent, respectively, the ionic radii of the A cation, B cation and X anion; the tolerance factor should be 1 for a perfectly cubic structure, though it is often found that $0.89 < t < 1$ in cubic perovskites.[36]

A perovskite structure is found in nature in a large number of mixed oxides, usually containing an alkaline earth metal and a transition metal; however, in synthetic perovskites, A cation can be both inorganic (although practically restricted only to Cs^{+}) and organic, while B cation is generally a post-transition metal (most often Pb^{2+}), and X anion is a halide ion. The most studied examples of hybrid perovskites are represented by methylammonium lead iodide[37,38] and formamidinium lead iodide,[39,40,41] since organic cations containing more than two carbon or nitrogen atoms would not fit the A sites in the crystal; however, many other materials featuring different ammonium cations, which are also called perovskites, even though they possess a different structure, have been prepared and investigated.

1.2.2 Perovskites' semiconductor properties

The most relevant attribute which makes hybrid perovskites so interesting is their being semiconductors; for this reason, they can be regarded as a very attracting alternative both to silicon and other elemental semiconductors and to compound semiconductors, such as ZnO, GaAs, InP or CdSe. In particular, unlike crystalline silicon, which is still, however, at the base of the semiconductor industry, perovskites do not need dopants, and they also possess direct band gaps,[42] allowing a convenient use both in light emitting devices and in photovoltaics.

In fact, as regards photovoltaic performances, the above-mentioned haloplumbate materials have shown optimal properties in terms of band gap values (1.55 eV for methylammonium lead iodide and 1.48 eV for formamidinium lead iodide, respectively), very close to the ideal value of 1.34 eV, which would correspond to the maximum PCE value of 33.7% for a single p-n junction, as predicted by the Shockley-Queisser limit, reported in **Figure 1.4**.[43]

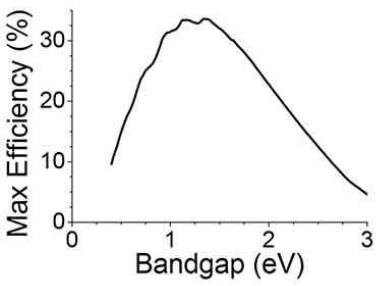

Figure 1.4 Shockley-Queisser limit.

In addition, they are characterized by low exciton binding energies[44] and long charge carrier diffusion lengths,[45] and they have been demonstrated able to transport effectively both electrons and holes;[46] moreover, they possess high absorption coefficients,[47] and their band gaps are easily tunable, by changing material composition.[48,49]

Among the advantages of hybrid perovskites, there are also the affordability of precursor compounds and the possibility to prepare and process them both as single crystals and as thin films from low temperature-solution methods,[50,51] in contrast to high temperatures required to obtain ultrapure silicon, necessary for traditional solar cells.

1.3 Perovskite solar cells

As for solar cells employing this type of materials as active layers, which are nowadays the most investigated application for hybrid perovskites, since 2009, multiple architectures have been designed and tested; the main distinction, however, is between mesoporous (or sensitized) and thin-film (or planar) perovskite solar cells, represented schematically in **Figure 1.5**:[52]

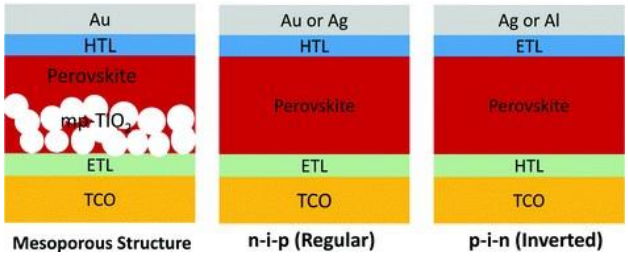

Figure 1.5 Schematic representation of perovskite solar cells; planar cells can have both a regular and an inverted configuration.

1.3.1 Solar cells structures

The first configuration, devised by Miyasaka, featured the haloplumbate ($CH_3NH_3PbI_3$ or $CH_3NH_3PbBr_3$) deposited as scattered particles onto a semiconducting mesoporous scaffold made of TiO_2. In this cell, the perovskite material only worked as a light absorber (as in dye-sensitized solar cells), while the photogenerated electrons, generated in it, were then injected into the mesoporous oxide, through which charge transport took place; the

photogenerated holes were in turn transported to the cathode through an electrolyte solution.

This perovskite-sensitized solar cell had, however, a very limited stability, since the polar solvent in the hole transport layer caused the dissolution of the active material: this led to the idea of replacing the liquid electrolyte with a solid hole transporting material, that is 2,2',7,7'-tetrakis(*N*,*N*-di-*p*-methoxyphenylamine)-9,9'-spirobifluorene (also known as spiro-MeOTAD), shown in **Figure 1.6**, which enhanced both cell efficiency and durability.[53]

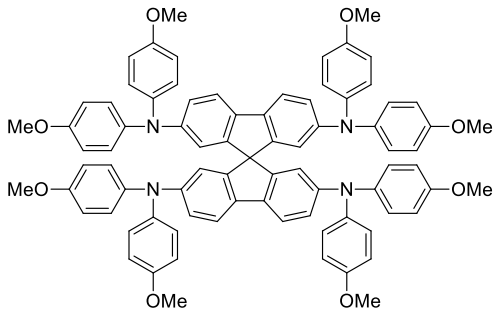

Figure 1.6 Structure of spiro-MeOTAD HTM.

Also, the mesoporous TiO_2 layer was later substituted with a non-conductive scaffold material, namely Al_2O_3, with an improvement in performance, demonstrating that perovskite layer can serve not only as a sensitizer, but also as a transport layer for electrons.[54]

The discovery of perovskite ability to function as an ambipolar charge carrier paved the way to the latter type of cells, which do not need the mesoporous TiO_2 layer, nor any scaffold material:[55,56] in planar configuration, not only electron-hole pairs are generated into a compact perovskite layer, upon light absorption, but they are also extracted through this active layer to adjacent ETM and HTM (electron- and hole-transport materials). The position of these two layers, acting as an *n*-type and a *p*-type semiconductor, respectively, while the perovskite is an intrinsic one, relative to that of the metal cathode and the FTO (fluorine-doped tin oxide) anode, is not fixed, since the preparation, in 2013, of the first perovskite solar cell featuring an "inverted" geometry, that is a HTM deposited onto the FTO, then a perovskite film and, after that, an ETM, in contact with the metal electrode.[57]

The absence of the mesoporous semiconducting oxide in the thin-layer configuration facilitates cell manufacturing, since lower temperatures and less complex techniques can be employed in the process, and allows good PCE values to be achieved, so, in the last years, planar configuration, both in the conventional (n-i-p) and in the inverted form (p-i-n) has received more and more attention and has become as popular as the mesoporous one.[58]

1.3.2 Drawbacks

Unfortunately, there are still several obstacles to perovskite solar cell diffusion on a large scale, especially those related to poor stability of these materials towards water and other environmental agents, such as oxygen, moderately high temperatures and light,[59] which result in a rapid loss of efficiency in solar cells and other perovskite-based devices when set in real operational conditions.

Since hybrid perovskites generally contain ammonium cations, moisture has obviously a detrimental effect, because it leads to hydrolysis reactions, turning them into the corresponding amines and so destroying the active material.[60] As an example, the most studied haloplumbate material, methylammonium lead iodide, reacts with water as follows:

$$CH_3NH_3PbI_{3(s)} + H_2O_{(l)} \rightleftarrows PbI_{2(s)} + H_3O^+_{(aq)} + CH_3NH_{2(aq)} + I^-_{(aq)} \quad (2)$$

The decomposition of the perovskite is also revealed by a color change of the material in presence of moisture, from black to yellow, due to the formation of PbI_2.

Oxygen is a troublesome element for this material as well, since it can react with photo-generated electrons to form superoxide ion, which can in turn deprotonate the methylammonium cation, eventually producing methylamine, together with PbI_2, I_2 and H_2O;[61] the reaction is, of course, promoted by light irradiation and it is also greatly enhanced by the presence of non-conducting Al_2O_3 (that does not absorb light in the solar spectrum), while the use of a TiO_2 ETL protects perovskite against this degradation path, because it is a strong absorber in the UV region ($\lambda < 400$ nm).

As concerns thermal stability, it is important that a perovskite does not undergo degradation processes up to temperatures around 85° C, for its profitable use in a

photovoltaic device, since this is the highest temperature normally reached in such equipment; unfortunately, methylammonium lead halides have shown serious decomposition phenomena even in encapsulated devices, that is in conditions where the interaction with external agents such as water and oxygen is suppressed.[62,63,64] For example, the most favored gas-releasing decomposition reaction at moderate temperatures for the iodide perovskite, from a thermodynamic point of view, is:

$$CH_3NH_3PbI_{3(s)} \rightleftarrows PbI_{2(s)} + NH_{3(g)} + CH_3I_{(g)} \quad (3)$$

However, the kinetic control over this reaction, owed to the high activation energy, makes the predominant degradation pathway to be:[65]

$$CH_3NH_3PbI_{3(s)} \rightleftarrows PbI_{2(s)} + CH_3NH_{2(g)} + HI_{(g)} \quad (4)$$

The stability can be improved by changing one or more of the components in the crystal: for example, mixed halide methylammonium lead perovskites have been proved to have a better stability, compared to their iodide counterparts;[66,67] moreover, the use of a different organic cation is another valuable approach to cope with perovskites' weak points. In this way, formamidinium ion can be employed both in conjunction with other A-type cations and alone, with beneficial effects for perovskite thermal and environmental stability.[68,69,70]

Strategies addressing these crucial issues so far have also relied very much upon perovskite protection from degradation sources, through encapsulation of the active layer by passivating agents or inclusion of additives in the precursor materials.[71,72]

Besides the lack of long-term thermal and chemical stability, a concern hindering the diffusion of perovskite-based devices on a commercial scale arises from the presence of hazardous substances, which could be released in the environment at any stage, starting from materials fabrication, throughout devices' lifetime, up to their disposal.[73,74,75] In particular, research on hybrid perovskites has focused until now mostly on lead-based materials, despite the fact that lead is a well-known environmental pollutant and a toxic element for human health; for these reasons, since the early days of lead halide

perovskites enthusiasm, the risk posed by their employ in real conditions has been investigated.[76]

Although the available studies indicate that the amount of lead in hybrid perovskite devices does not represent a worse danger than those coming from other components of such devices, from other types of photovoltaic materials (such as CdTe) and from other sources of lead in the environment, still the possibility to replace this hazardous metal remains a critical challenge to make hybrid perovskites ever more sustainable.

1.4 Lead-free perovskites

The success of lead in perovskites up to now has been determined by different factors: firstly, by its abundance, which contributes to material affordability; moreover, lead halide perovskites have shown optimal semiconductor properties, as already mentioned, and currently available alternatives to lead have not reached comparably satisfactory performances yet.

A considerable amount of research, however, has been carried out in recent years to obtain functional and profitable hybrid halometallates, by benefiting from other transition and post-transition metal cations, both possessing the same valence as Pb(II), in order to maintain the ABX_3 formula, and with a different valence, thus changing the stoichiometry of the compounds.[77,78,79]

As regards ABX_3 metal halide perovskites, tin is considered to be, at present time, the most promising candidate to replace lead, especially as a photo-absorber in solar cells, so the vast majority of the literature dealing with lead-free perovskites is focused on tin-based ones.[80,81] In fact, Sn^{2+} ionic radius is similar to Pb^{2+} one (1.35 Å versus 1.49 Å), so the formation of a nearly ideal perovskite structure is allowed; moreover, tin halide perovskites have shown convenient characteristics for photovoltaics, above all a direct and narrower band gap, if compared to their lead counterparts, which is a highly desirable feature in order to obtain highly efficient solar cells: for example, methylammonium tin iodide band gap is around 1.2 eV, while for formamidinium tin iodide the value is 1.41 eV.[82]

Nevertheless, the attained PCE values for tin-based perovskite solar cells are far inferior to those for lead-containing devices, with the best results being still around 14%.[83] Such disappointing performances can be ascribed, on the one hand, to the poorer film formation properties of tin halide perovskites, which make solvent choice and preparation techniques a crucial issue in the progress of these materials; on the other hand, the (+2) oxidation state in tin is not so stable as in lead, so Sn^{2+} can be easily oxidized by atmospheric oxygen to Sn^{4+}.[84] The consequent formation of additional vacancies, making organotin halides behave as *p*-type semiconductors, rather than intrinsic ones, creates an unbalanced positive charge, which accelerates material degradation, besides increasing charge carrier recombination rate, so perovskite encapsulation is fundamental.

Another group-14 element which has been evaluated as a possible substitute for lead in hybrid perovskites is germanium, though it possesses a smaller ionic radius, compared to the previous ones, and also suffers from the same oxidation tendency of its (+2) state to the more stable (+4) state; its methylammonium and formamidinium iodides, however, have shown wider band gaps than iodoplumbates and iodostannates compounds, which additionally enlarge when increasing the dimension of the organic cation, so this makes them less suitable as candidates for solar cells.[85]

Instead of replacing lead with another element in the same oxidation state, it is also possible to obtain perovskite-type materials by a heterovalent substitution, in two ways: either with the mixed-valence approach, or by using a cation with a different valence from Pb^{2+}. The first strategy requires the use of two distinct metal cations, a monovalent and a trivalent one, in an equimolar mixture, to yield compounds described by the general formula $A_2B^{I}B^{III}X_6$, the so-called "double perovskites", one example of which is represented by the all-inorganic $Cs_2AgBiBr_6$.[86] Alternatively, a metal in its (+3) oxidation state can also be used as a B-type cation, and thus the general formula becomes $A_3B_2X_9$, to ensure charge balance; the elements that have raised attention for this type of materials are especially Bi and Sb, for their suitable dimensions.

In particular, Bi^{3+} cation possesses the same electronic configuration as Pb^{2+}, that is $6s^26p^0$, and the position of bismuth in the periodic table is also adjacent to that of lead, so the dimension of the two ions is very similar, making it likely to form a perovskite-type structure; in addition, bismuth has a very low toxicity and for this reason its incorporation in functional materials is regarded as an encouraging and benign perspective.[87]

From a practical point of view, another advantage in the use of bismuth in hybrid perovskites for optoelectronic devices is represented by its excellent stability in environmental conditions, conversely from tin and germanium, since it is not oxidized by atmospheric oxygen, making materials handling and processing easier. As regards photovoltaic performances, most bismuth halide perovskites exhibit, regretfully, band gap values above 2 eV (for example, 2.1 eV for methylammonium bismuth iodide), together with defect states which lead to charge carrier recombination, thus limiting cell efficiencies;[88] film quality and interactions of perovskite layer with surrounding ETM and HTM for an optimal band matching are also important issues to be addressed, in order to improve PCE values.[89]

Clearly, since the fields of application for hybrid perovskites, apart from solar cells, are numerous, the search for new materials and the possibility to replace lead with other metals is also important when it comes to different purposes and devices and, in addition, this is an opportunity to make profitable use of those materials whose electronic properties are not optimal for photovoltaics.[9091]

1.5 Low-dimensional perovskites

The formation of a perovskite crystal structure, as seen previously, demands quite stringent geometric requisites, and it is thus clear that the choice of organic cations which can be accommodated in such a lattice is very limited. Nevertheless, the extremely versatile features shown by organic halometallates have pushed chemists to expand the scope by introducing different organic cations, resulting, from a structural point of view, in a substantial modification of the crystal lattice, but also in an extraordinary tunability of physical and photophysical properties.

The materials obtained by this strategy are defined as “low-dimensional perovskites”, since they are derived from perovskites, but do not possess the same tridimensional structure; it is important to highlight, however, that the control over the dimensionality of these hybrid materials can be obtained both on a morphological level, by fabricating nanostructured perovskite crystals (such as nanoplatelets, nanorods and quantum dots) and on a molecular level, by the formation of metal halide units consisting of planes,

wires or isolated clusters, surrounded by organic cations.[92] In particular, the attention herein will be focused on the second approach.

1.5.1 2D and quasi-2D perovskites

A valuable method in the search for more stable and tailor-made perovskite-related materials has been found in the insertion, besides "classic" A cations (usually methylammonium or formamidinium, or Cs^+ in all-inorganic perovskites), of an auxiliary organic cation, bulkier than the previous and acting as a spacer between the planes formed by corner-sharing BX_6^{4-} octahedra. The hybrid materials displaying this type of structure are the so-called 2D halide perovskites, or layered perovskites, which can be described by the general formula $R_2A_{n-1}B_nX_{n+1}$, with $n \geq 1$, where R represents the large organic cation, generally possessing one or more ammonium groups, as it is for A.[93] The number of 3D perovskite layers interposing between large organic cations is defined by the value of *n*: for example, when $n = 1$ there is a single layer of metal halide octahedra and a single type of organic cation, typically constituted by a long alkyl chain or one or more aromatic rings bearing an ammonium group.[94,95]

Moreover, as shown in **Figure 1.7**, different phases, with peculiar physical properties, can be obtained by an accurate choice of the structure and charge of the large organic cation embedded in the 2D perovskite crystal.

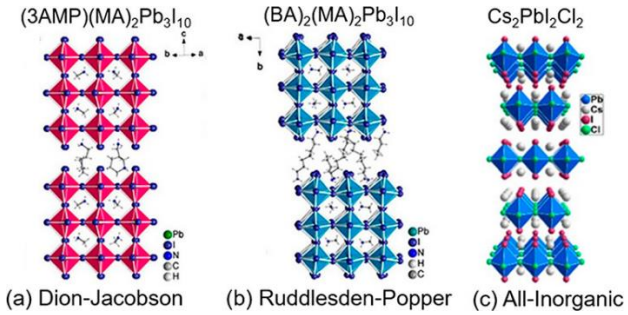

Figure 1.7 Different 2D perovskite phases.

For example, in Ruddlesden-Popper type, spacers are monovalent alkylammonium cations, forming a double layer, held together by Van der Waals forces or π-π stacking interactions (when aromatic rings are present), between metal halide octahedra; on the contrary, Dion-Jacobson type is characterized by the presence of diammonium cations inserted into the lattice, connecting adjacent planes of the inorganic framework by

electrostatic interactions, so they are characterized by a shorter distance between the inorganic portions and an overall steadier structure, owing to the stronger chemical bonds.[96,97]

In addition, quasi-2D perovskites are materials characterized by the presence of different 2D perovskite phases piled one above another: indeed, they are formed by sandwiching large organic cations between layers of 3D perovskite, each layer containing a different number of metal halide octahedra sheets, so a different *n* value; their optoelectronic properties are mainly determined by the structure and dimension of the organic spacer cation and they are particularly suited for application in LEDs.[98] An example of a quasi-2D perovskite is reported in **Figure 1.8**.

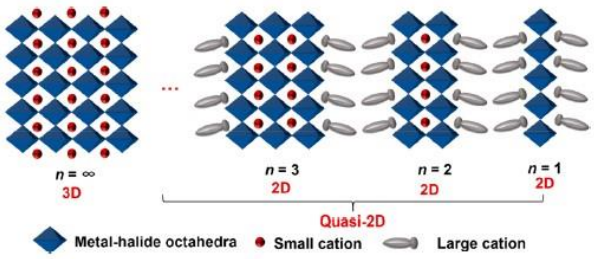

Figure 1.8 Comparison between a 3D and a quasi-2D perovskite structure.

Two-dimensional perovskites have shown enhanced stability toward ambient conditions, compared to 3D ones, thanks to higher hydrophobicity of large organic cations, in addition to good performances both in solar cells and light emitting devices, and they also allow a fine tuning of their photophysical properties, through the careful choice of the spacer and the ratio between it and the small organic cation, which determines the thickness of the layers.[99] Nevertheless, the presence of different A-type cations often leads to phase impurities, structural disorder, and additional defects, difficult to control and limiting device performances; moreover, the presence of large organic cations, together with methylammonium or formamidinium, although improving material stability, does not eliminate their inherent water reactivity, especially if the spacer cation contains acidic protons susceptible to hydrolysis reaction.

1.5.2 1D and 0D perovskites

The introduction of large organic species, which do not allow the construction of a 3D perovskite structure, can also result in the formation of infinite chains of BX_6^{4-} octahedral units connected to each other by corners, edges or faces and surrounded by organic cations, that is, in a 1D perovskite structure, on a molecular level, like those in **Figure 1.9**.

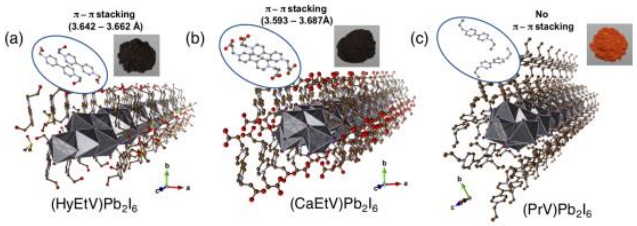

Figure 1.9 Examples of 1D perovskites.

This kind of materials is, in spite of the name, constituted by bulk crystals and not nanocrystals, since the dimensionality is referred only to the inorganic framework; however, the presence of organic units, which are usually characterized by a wider HOMO-LUMO distance, if compared to metal halide band gap, interposed between the inorganic semiconductor moieties, allows them to behave as quantum wires.[100]

If, eventually, metal and halide ions form isolated polyhedrons (as in **Figure 1.10**) or clusters in the bulk crystal, the hybrid material can be defined as a 0D perovskite.

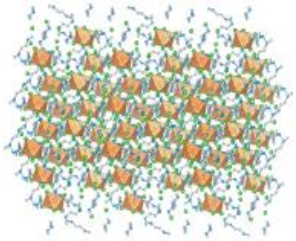

Figure 1.10 Example of a tin perovskite possessing a 0D structure.

Similarly to 1D perovskites and related organic halometallates, also this class of hybrids, in which the energy gap is generally higher than the value in 3D analogues, and consequently less favorable for solar cells, is investigated especially for their light emission properties, since they feature broadband emissions and very high PLQE, making

them very promising candidates for light emitting diodes; moreover, emission wavelength, and thus color, has been proved to be tunable by changing and mixing the halide ions.[101] Research on these innovative materials for light emission and other applications has taken advantage from a vast range of metals, besides lead and tin, to obtain an extraordinary variety of structures, both characterized by the inorganic units arranged in single polyhedrons (not just octahedra, but also pyramids or tetrahedra) and featuring polymetallic clusters, also with the introduction in the crystal of organic ions different from ammonium, such as phosphonium ions.[102,103]

1.6 Cation engineering

An insight into the literature seems to suggest that research in the field of metal halide perovskites and related hybrids, so as to achieve stable and useful materials for optoelectronic applications, has not fully profited yet from the almost unlimited variety of organic cations which can be incorporated in these structures, especially in the light of the ever-growing interest in 2D, 1D and 0D perovskites: since geometric constraints, expressed by the tolerance factor in 3D perovskites, can be overcome in lower-dimensional ones, there is no virtual limit to the size and charge of the organic cation.
With this concept in mind and given that the exploration of different metals and halides and combinations of them is already a well-established branch of research, as seen previously, a clear necessity of focusing on the design of the organic cation emerges, in order to improve both functionality and stability of perovskite materials.

1.6.1 Conjugated organic cations

The greatest amount of work on hybrid perovskites has been dedicated to the study of materials containing small organic cations; apart from the two most famous examples, a bunch of different species has been proposed as A cation, in an attempt to fit them in a perovskite lattice, if necessary, with a certain degree of distortion. Examples found in the literature include ethylammonium,[104] guanidinium[105] and azetidinium,[106] together with some non-ammonium cations, such as trimethylsulfonium[107] and tetramethylphosphonium.[108]

The emergence of low-dimensional perovskites has obviously widened the horizons to different species, with no more size restrictions, and a great deal of alkylammonium cations, featuring different lengths of the chain, has been included in hybrid halometallates; in addition, alkylammonium chains linked to aromatic rings have also been exploited, with the aim of taking advantage from enhanced cation stability.[109] The introduction of aromatic units has not been limited to phenyl rings only: for instance, a lead iodide and a tin iodide perovskite containing tropylium ion[110] (**Figure 1.11a**) and a lead iodide perovskite containing tetrathiafulvalene radical cation[111] (**Figure 1.11b**) have been synthesized and studied in recent years; moreover, a series of pyrazinium (**Figure 1.11c**) dications has been used to synthesize lead bromide perovskites.[112]

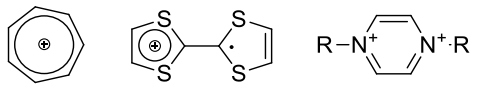

a **b** **c**

Figure 1.11 Some examples of functional organic cations in perovskites: **a)** tropylium; **b)** tetrathiafulvalene radical cation; **c)** pyrazinium.

It is important to note that in previously examined materials, in which the organic cations do not contain chromophores, the optoelectronic characteristics are essentially due to the inorganic components, while the organic moieties only play a structural role; on the contrary, by inserting an electroactive organic species, as just seen, it will have an active role in the interaction between the hybrid crystal and radiation or electric field, so the photophysical properties of the material will be ultimately determined by the interplay between the inorganic and the organic lattice.[113]

Along with the already mentioned examples, featuring quite simple conjugated organic cations in perovskite-type materials, it is also possible to embed organic dyes possessing more complicated structures. One of the first reported haloplumbates with such an organic component was AEQTPbBr$_4$, containing the doubly protonated 5,5‴-bis(aminoethyl)-2,2′:5′,2″:5″,2‴-quaterthiophene,[114] shown in **Figure 1.12**, since oligothiophenes are known for their high electrical mobilities and they are very efficiently integrated in molecular wires; moreover, their HOMO-LUMO distances are easily tuned by changing the number of thiophene rings.

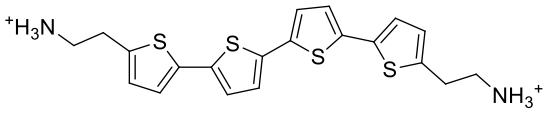

Figure 1.12 $AEQT^{2+}$ structure.

More recently, another cationic organic compound characterized by an extendedly conjugated structure and high optical absorption, that is, a cyanine derivative, with the structure represented in **Figure 1.13**, has been employed for the preparation of a one-dimensional lead iodide perovskite, possessing intense and broad NIR absorption and emission.[115]

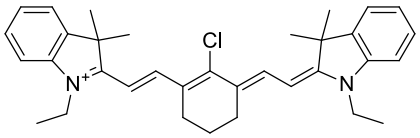

Figure 1.13 A cationic cyanine derivative employed in a hybrid perovskite.

1.6.2 Quaternary ammonium cations

Since the major drawbacks of perovskites are currently represented by their poor durability, it follows that an accurate choice of the organic species should aim to obtain intrinsically more environment-tolerant materials: the most important degradative process, in fact, undergone by hybrid perovskites containing acidic protons is represented by the hydrolysis of the ammonium cation, so a straightforward approach should imply the use of quaternary ammonium cations.

Nevertheless, this strategy has not been explored by now as much as one might think, while a considerably greater effort has been put in the design of materials for passivation and encapsulation of the perovskite layer.

However, a certain number of examples already exist of hybrid halometallates featuring cations devoid of hydrolysable protons and some of them have already been reported in the previous paragraph, including non-ammonium cations. For instance, a layered tin iodide perovskite containing a dication in which one of the ammonium groups was quaternary had been already synthesized in 2003, before the interest in hybrid perovskites for photovoltaic applications exploded.[116]

Moreover, in recent years, different alkylammonium ions with a quaternarized nitrogen atom, such as choline,[117] tetrabutylammonium[118] and tetraethylammonium[119] have been profitably used as additives in lead halide perovskites for solar cells and other devices, improving both stability and performances. As regards the simplest quaternary ammonium cation, namely tetramethylammonium, its iodoplumbate has been synthesized and characterized, to assess its chemical and thermal stability, which has proved to be far better than that of methylammonium; regretfully, its wide band gap (2.79 eV) makes this material unsuited for photovoltaic cells.[120]

Apart from these examples, in which the organoammonium cations have a quite simple structure, also some aromatic cations without acidic protons have been integrated in metal halide frameworks, to afford hybrid materials having structural as well as photophysical properties that result from the interaction of the inorganic and organic constituents. In particular, a motif which has been successfully exploited for the construction of perovskite-related hybrids with functional organic cations is that of 4,4'-bipyridinium quaternary ions, shown in **Figure 1.14**, also known as viologens: indeed, several halometallates featuring different groups on nitrogen atoms have been prepared and studied.[121,122,123,124]

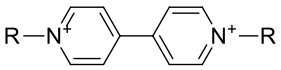

Figure 1.14 Structure of 4,4'-bipyridinium dications (viologens).

The ease of synthesis and the possibility to adjust material properties by changing the type of substituent, along with the presence of aromatic rings and the absence of protons, make viologens and derived structures an inspiring platform for the design of efficient and tunable hybrid perovskites.

Chapter 2: Aim of the work and main experimental techniques

2.1 Choice of the target cations

As seen in the introduction, the most promising strategy to obtain environmentally stable and efficient hybrid perovskites by modifying the organic cation, has proved to be the use of quaternary and conjugated ammonium cations. However, most of the materials already described in the literature have been prepared starting from commercially available organic salts, or by readily affordable ones, through a single synthetic step.

The present work was then directed to follow this path, so we decided to focus on the design of the organic cation, by exploiting common organic synthesis procedures to obtain tailor-made organic species, possessing a complex, extendedly conjugated structure with quaternary ammonium groups. The organic salts synthesized in this way were subsequently used to form hybrid iodometallates, the properties of which were finally investigated by solid-state chemistry and physics techniques.

2.1.1 Viologens

Among the previously mentioned examples of organic salts possessing the desired features there are viologens, that is, quaternary 4,4'-bipyridinium salts (**Figure 1.14**, Chapter 1); for this reason, they have already been chosen for the preparation of several metal halide perovskites.

In fact, viologens began to draw attention for their interesting properties before the middle of the twentieth century: in 1932, Michaelis recognized the possibility to use methyl viologen, also known as "paraquat", as an indicator for redox reactions,[125,126] since it can be converted, through a one-electron reduction, to an intensely colored radical cation (and it possesses three reversible and stable redox states, namely dication, radical cation and neutral), while, in the 50's, its herbicidal action was discovered. Since then, many properties of viologens have been extensively studied, for instance their formation of charge-transfer complexes,[127] their electrochromism[128] and their antibacterial activity.[129] This has led quaternarized 4,4'-bipyridines to become a common motif in a vast range of functional organic and hybrid molecules and macromolecules, with applications spanning from memory devices[130] and transistors[131] to molecular machines,[132] from gas storage and

separation[133] to energy conversion, as catalysts for hydrogen generation[134] or dyes in solar cells,[135] just to mention a few examples.

Such a variety in the types of devices containing viologen derivatives is made possible both by their already mentioned peculiarities and by their extremely flexible structure, which enables almost limitless modification and functionalization.[136] First of all, the nitrogen atoms can be quaternarized not only by alkyl chains of various length or aromatic rings, but also with more complex moieties or even polymeric chains, allowing their introduction on the side chain of preexisting polymers or the assembly of viologen-based polymers, both linear ones and dendrimers.[137,138,139]

Furthermore, the two pyridinium rings are not required to be directly linked in the *para* position, since a great number of compounds have been prepared featuring a conjugated spacer, such as a double or triple bond or an aromatic ring, between the two heterocyclic rings and retaining viologen physical properties, such as electron-accepting capability.[140,141] The same holds for bridged or fused bipyridinium dications, provided that conjugation is ensured, both for those possessing a 4,4'-connection and for the ones connected in different positions.[142,143]

The presence of a central conjugated core has also been exploited for the synthesis of multiarmed extended viologens, that is, polypyridinium cations with a branched structure,[144] which can constitute a convenient platform for the construction of cross-linked poly(extended viologens). Notably, many of these extended viologen derivatives can be conveniently prepared by simple building blocks, through straightforward synthetic routes, making use of palladium-catalyzed cross-coupling reactions.

2.1.2 New viologen-derivatives as organic cations for hybrid perovskites

The structure of the cations to be embedded in new hybrid perovskites was then designed considering the synthetic versatility of quaternary pyridinium salts and the need to establish conjugation over the entire molecular skeleton. In this sense, the recent preparation and characterization of phenyl viologen lead iodide, a thermally and water-stable semiconductor material possessing a 1D perovskite structure and a narrow band gap of 1.32 eV has shown the beneficial effect of an extension in the conjugation for the improvement of physical and optical properties.[145] The structure of phenyl viologen

cation and of the corresponding hybrid lead halide perovskite are shown in **Figure 2.1a** and **b**, respectively.

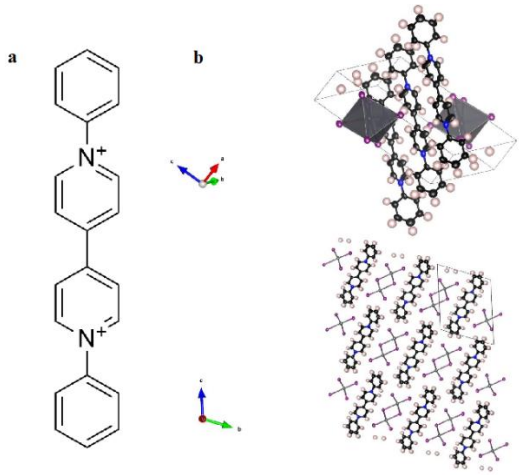

Figure 2.1 a) Phenyl viologen cation; **b)** phenyl viologen lead iodide unit cell (top) and crystal structure showing lead halide chains and organic cations (bottom), (reproduced from ref. 145).

As regards the use of extended viologens, a paper was reported a few years ago, describing a novel hybrid iodoplumbate, featuring such a type of compound, represented by the species in **Figure 2.2a**, as the organic component: in this dication, an anthracene subunit is inserted as a conjugated spacer between the two pyridinium rings; the material obtained in this way, displayed in **Figure 2.2b**, exhibits a 3D metal halide framework, with channels in which the organic cation is accommodated, and the measure of its band gap gave a value of 2.06 eV, exhibiting a semiconductor behavior.[146]

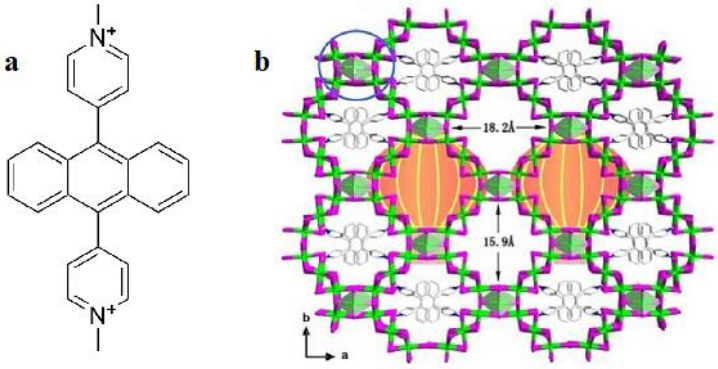

Figure 2.2 a) An extended viologen cation featuring an anthracene core; **b)** a representation of crystal structure of the lead halide derivative containing the organic species in **a** (reproduced from ref. 146).

This prompted us to synthesize a series of extended viologens, employing different central aromatic moieties, as shown in **Figure 2.3**, to verify their effect on the final characteristics of the organic salts and of the corresponding hybrid iodometallate derivatives. We decided to quaternarize pyridine rings with methyl groups in all of the synthesized compounds, both for the efficiency and affordability of methyl iodide as a methylating agent (although it was not utilized for the preparation of cations **7** and **8**, as will be shown in detail in Chapter 5, section **5.1.5**, since the synthetic pathway we followed devised a different reaction), and to maintain a structural homogeneity.

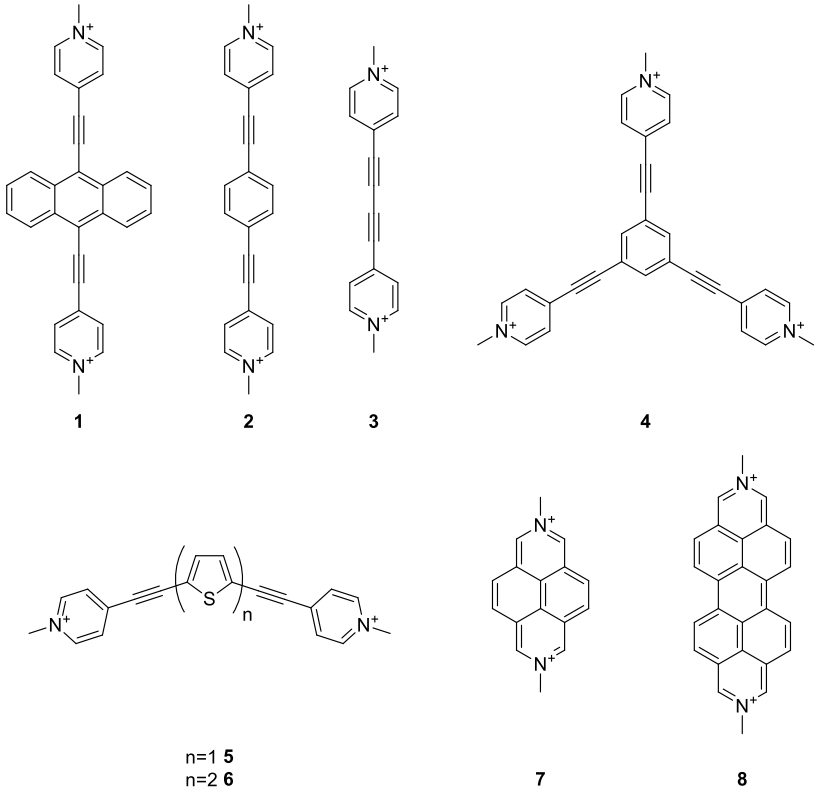

Figure 2.3 Structures of cations described in this work.

Moreover, we decided to introduce a further spacing element, connecting the core to the peripheral heteroaromatic rings with nitrogen atoms attached to methyl groups: in particular, we chose triple bonds, owing to their widely reported effectiveness in electron transport, which has made them one of the most exploited motifs in molecular electronics.[147,148] The presence of acetylenic units offers some additional interesting attributes: in the first place, they can be favorably integrated in the conjugated framework by using the well-established palladium-catalyzed Sonogashira cross-coupling and,

secondly, they possess a linear geometry, so rotation around the unsaturated bond is permitted and it can considerably affect structural and optical properties of the materials. As regards cationic species **7** and **8**, the synthesis of their salts was already described in the literature; nevertheless, they had never been employed for the preparation of metal halide perovskites. The use of fused ring viologen derivatives for the construction of this kind of materials was thus envisioned by us in reason of their complete structural rigidity: contrarily to the other cations shown in **Figure 2.3**, they do not possess any rotational degree of freedom (except for hydrogen atoms in methyl groups), so we wanted to understand the consequences of this characteristic on materials structure and properties.

2.2 General characterization techniques

After the preparation of the organic salts and the dissolution in a proper solvent, these salts were reacted with solutions of metal iodides, in particular lead iodide and bismuth iodide (the reasons for the choice of these two elements have already been explained in Chapter 1), to provide the respective iodometallates, which were isolated by precipitation and filtration. The solid materials thus obtained were characterized by various instrumental methods, to assess their physico-chemical properties and their suitability for optoelectronic applications.

It is important to note however, that, while for the two perovskites prepared with the anthracene derivative **1** an extensive characterization has been achieved, for the other hybrid perovskites just a few analyses have been performed until now, so the available information about them is still partial and they need further insight.

The fundamentals of the most important characterization methods employed in the course of the work are going then to be presented, together with the information they offer; different types of analysis, carried out by other research groups on one or both of the perovskites containing cation **1** will be briefly described in the next chapters, when discussing the characterization of the single materials.

2.2.1 Powder X-ray diffraction

Powder X-ray diffraction is one of the most common and basic analysis techniques for solid materials,[149] since it can be performed with a minimal sample preparation, consisting essentially in the reduction of the solid into an homogeneous powder, or with no preparation at all, and also on unknown solid samples;[150] in addition, it is non-destructive (except for very sensitive organic compounds)[151] and it requires quite modest amounts of sample; a drawback is however represented by the need for crystalline compounds to perform the analysis.

This fundamental characterization technique is based upon the elastic scattering, that is, scattering that occurs without absorption of energy, of X-ray radiation by atoms, and more specifically by electrons, periodically arranged in a crystal. The experimental setup, schematized in **Figure 2.4**, can be summarized as follows: a monochromatic, collimated X-ray beam is directed onto a specimen, consisting of a crystalline powder on a sample holder, and the incident rays are diffracted at specific angles, depending on the different sets of lattice planes.

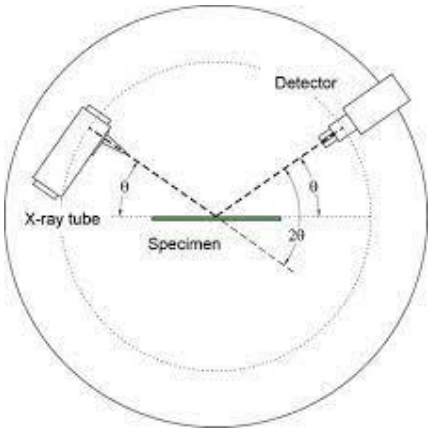

Figure 2.4 Schematic representation of a powder X-ray diffraction experiment.

If a crystal is considered as composed by parallel planes, able both to reflect and to transmit X-rays, then a constructive interference is produced by different reflected rays (1′ and 2′ in **Figure 2.5**), provided that Bragg's law is satisfied:

$$2d\sin\theta = n\lambda \quad (5)$$

where d is the distance between two adjacent lattice planes in the crystal, θ is the angle between the lattice planes and the direction of the diffracted beam, n is an integer and represents the diffraction order (although it is usual to consider only $n = 1$, or first order) and λ is the radiation wavelength, which must be comparable to interatomic distances in the crystal (some Å) in order to give diffraction phenomena.

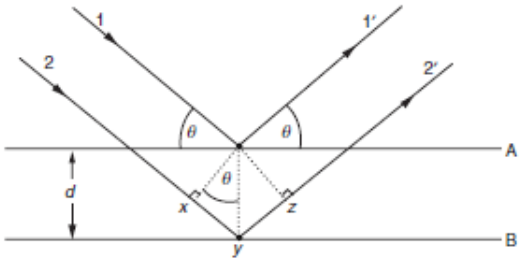

Figure 2.5 Derivation of Bragg's law.

X-rays are generated in a cathode tube by accelerating, through the application of a voltage of about 40 kV, the electrons produced by the heating of a tungsten filament and allowing them to impact on a target fixed to the anode, usually made of copper; the accelerated electrons cause an electron in the inner shell of the metal to be expelled, together with the emission of X-ray radiation. The emitted radiation contains several components, the wavelengths of which depends on the element used as target, so a filter or a monochromator crystal is used to select only the λ of interest, which corresponds to the K_α transition, or 2p→1s; in most cases Cu is used as X-ray source, so the radiation employed for diffraction is Cu K_α, possessing $\lambda = 1.54184$ Å (which is actually a weighted average of $K_{\alpha 1}$ and $K_{\alpha 2}$).

Since the sample is constituted by a great number of very small crystals, their orientation, and so the orientation of lattice planes, will be casual and there will be some of them at the Bragg angle, and thus producing diffraction, for every set of lattice planes. The diffracted beams are collected by a detector, usually a scintillation detector, connected to a computer, which performs a scan of 2θ (the angle between the incident and the diffracted beam) values, at constant angular velocity, yielding a diffractogram, or diffraction pattern, that is, a plot of the diffracted intensity as a function of 2θ.

If the crystal structure, and consequently the atomic coordinates and the type and composition of the unit cell for a compound are known, it is possible to calculate peak positions and intensities and thus assign every peak in the diffraction pattern to the corresponding lattice plane; however, this is practically feasible only for high symmetry crystals.

It follows that the diffraction pattern is characteristic of a certain substance in a certain crystal phase, and it can be used as a fingerprint for identification, if the substance is already known, or as a means to confirm its purity,[152] so it represents a fundamental information for a crystalline solid; moreover, additional information can be obtained from it, such as particle size and presence of defects, or it can be used for a quantitative analysis.[153] Anyway, the determination of the crystal structure from powder XRD is extremely challenging[154] and usually attainable with more success for inorganic compounds crystallizing in high-symmetry space groups and containing heavy elements, while it is almost impossible for crystals possessing both heavy and light atoms and a large unit cell, as is the case for metal halide perovskites containing bulky organic species; in these cases, diffraction data from single crystal are essential.

Powder X-ray diffraction analyses reported in the present work were performed with a Malvern Panalytical X'Pert Pro MPD diffractometer (Cu K_α radiation, λ = 1.54184 Å), operating in Bragg-Brentano geometry and equipped with an ultrafast X'Celerator RTMS detector, with an angular resolution in 2θ of 0.001°. The scans were collected in the 3.5-90° 2θ angular range and a beam knife was used in the 4.5−6.5° range to reduce the background.

2.2.2 Thermogravimetry-differential thermal analysis

It is of fundamental importance, for materials intended for use in photovoltaic or other optoelectronic devices, and thus subject to moderately high temperatures during operation, to investigate their behavior when they are heated, in order to assess the temperature at which their decomposition starts; for this reason, thermal analysis is another very relevant characterization method for hybrid perovskites.[155]

Thermogravimetry (TG),[156,157] in particular, is a quite old technique, based on a very simple principle, which measures the variation in mass of a substance when the temperature is changed over time: the mass of the sample is recorded continuously by a

thermobalance, while the temperature changes at a constant rate, and specifically increases, in the experiments described in this work.

Thermogravimetric analyses can be performed in different atmospheric conditions, such as in vacuum, air or an inert gas atmosphere, and the outcome may be different, that is, mass losses will take place at different temperatures, because they are due to different decomposition reactions.[158]

It is usual to couple thermogravimetry with another analytical method, in order to obtain details about the changes occurring in the substance at different temperatures: for example, TG can be used in conjunction with differential thermal analysis (DTA)[159] or differential scanning calorimetry (DSC),[160] which give information on the type of phenomenon observed, even though it does not imply a change in mass, or with techniques which allow the identification of the gaseous product obtained, such as FTIR spectroscopy[161] or mass spectrometry.[162] In the present work, thermogravimetric analyses were combined with DTA, so only this technique will be briefly presented.

In differential thermal analysis, the difference in temperature between the sample and an inert reference material, for example Al_2O_3, is measured, while they are exposed to the same thermal program, so they are placed together in a heating block, where they are heated (or cooled) in the same controlled manner: the temperature of the sample and that of the reference remain constant until some thermal event in the material under examination happens. When an absorption or release of energy by the sample occurs, a difference in temperature will be recorded, resulting in a peak in the DTA curve.

All the TG-DTA experiments described in the present work were performed using a Netzsch STA 409 PC Luxx simultaneous thermal analyzer. The analyses were performed under flowing Ar atmosphere (85 cm^3/min at STP, purity ≥ 99.9995%) in Al_2O_3 crucibles and a thermal scan rate of 10 K/min in the 30−500° C temperature range was used.

2.2.3 Diffuse reflectance UV-visible spectroscopy

Another essential characterization technique for hybrid perovskites, being their absorption of visible light fundamental for their operation in solar cells, is UV-visible spectroscopy; however, given that perovskites are crystals, and so they are formed in the solid state, it is not possible to determine their absorbance in solution, where only the dissolved precursors are present. For non-metallic solid materials for which dissolution

implies a modification or a decomposition of the absorbing species, and in particular for powders, absorption of radiation in the UV and visible region is usually determined in an indirect way, by their diffuse reflectance.[163]

In a sample composed by solid particles of which dimensions are comparable to the wavelength of the incident light, the interaction with radiation gives rise to a series of phenomena, including reflection, refraction and diffraction, in addition to absorption; for irregular particles of different dimensions which are in contact with each other, interference effects are predominant and, since it is not possible to separate the various contributions, the resulting scattering is called *multiple scattering*. For multiple scattering, there is no general solution to describe the system, but it can be treated by using two different constants, one for absorption and one for scattering, and by considering the material as a continuum, which is a fair approximation for a powder of closely packed particles.

As regards reflection, it can consist of two different types: there can be a *regular* (or *directional*) *reflection*, in which the reflected beam follows the same path as the incident one, but in the opposite direction, as happens at the surface of a plane mirror or a metal surface, or there can be a *diffuse reflection*, which has an isotropic angular distribution, that is, it is not dependent on the angle of incidence of radiation. Although for every opaque solid a regular reflection component is present, the diffuse one predominates and so the condition which is observed for this type of samples is indicated as *diffuse reflectance*.[164]

The most widely accepted and used theory to describe diffuse reflectance by a powdered sample is that of Kubelka and Munk, developed in 1931;[165] it considers as distinct the contributions from absorption and scattering, as seen before, and makes the assumption that incident radiation, as well as the reflected one, is diffuse.

The radiation flux in a layer of absorbing solid, considered as formed by parallel planes, can be regarded as the balance between the fluxes in the two opposite directions, as shown in **Figure 2.6**.

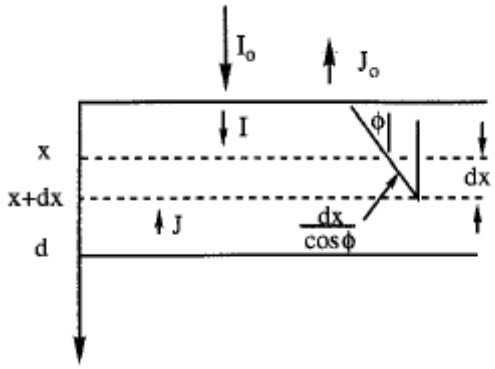

Figure 2.6 Scheme of a layer of total thickness d, composed of absorbing particles.

If a layer of thickness *x*, and an infinitesimal portion of it, of thickness *dx*, are considered, and the diffuse radiation intensities in the positive and negative *x* directions, respectively, are indicated with *I* and *J*, then the following differential equations, describing the variation of the intensities in the opposite directions, as a consequence of absorption and scattering, can be derived:

$$-\frac{dI}{dx} = (K+S)I - SJ \quad (6)$$

$$\frac{dJ}{dx} = (K+S)J - SI \quad (7)$$

where *K* and *S* are coefficients for absorption and scattering, respectively. In passing through *dx*, *I* decreases by an amount of *KIdx*, owing to absorption and by an amount of *SIdx*, owing to scattering, while it increases by an amount of *SJdx*, as a consequence of the scattered fraction of *J*; a similar analysis can be made for *J*, but it increases while going through *dx*.

Solutions to these equations have the following general form:

$$I = A(1-\beta)e^{\rho x} + B(1+\beta)e^{-\rho x} \quad (8)$$

$$J = A(1+\beta)e^{\rho x} + B(1-\beta)e^{-\rho x} \quad (9)$$

where

$$\rho = [K(K+2S)]^{\frac{1}{2}} \quad (10)$$

$$\beta = \frac{\rho}{K+2S} = \left(\frac{K}{K+2S}\right)^{\frac{1}{2}} \quad (11)$$

A and B in equations (8) and (9) are constants which depend on boundary conditions; for integration on the entire thickness of the sample, that is, from $x = 0$ to $x = d$, these are $I = I_0$ and $J = J_0$, for $x = 0$, and $I = I_d$ and $J = 0$, for $x = d$. By applying boundary conditions, expressions for A and B can be obtained:

$$A = -\frac{(1-\beta)e^{-\rho d}}{(1+\beta)^2 e^{\rho d} - (1-\beta)^2 e^{-\rho d}} I_0 \quad (12)$$

$$B = \frac{(1+\beta)e^{\rho d}}{(1+\beta)^2 e^{\rho d} - (1-\beta)^2 e^{-\rho d}} \quad (13)$$

Reflectance R of the sample can be defined as the ratio between J_0 and I_0 and is given by the following formula:

$$R = \frac{J_0}{I_0} = \frac{(1-\beta^2)(e^{\rho d} - e^{-\rho d})}{(1+\beta)^2 e^{\rho d} - (1-\beta)^2 e^{-\rho d}} \quad (14)$$

For a layer of infinite thickness, reflectance becomes R_∞ and its value is given by:

$$R_\infty = \frac{1-\beta}{1+\beta} \quad (15)$$

which is equivalent to

$$\beta = \left(\frac{K}{K+2S}\right)^{\frac{1}{2}} = \frac{1-R_\infty}{1+R_\infty} \quad (16)$$

By rearranging equation (16) it is possible to obtain the following equation:

$$\frac{K}{S} = \frac{(1-R_\infty)^2}{2R_\infty} = F(R_\infty) \quad (17)$$

which is known as Kubelka-Munk equation, while $F(R_\infty)$ is called Kubelka-Munk function.

In practice, the quantity which is measured experimentally is reflectance, and then it is converted through Kubelka-Munk equation into a *pseudoabsorbance*, which depends on the ratio between absorption and scattering coefficients. This theory holds for a layer of solid possessing a thickness of some millimeters, which approximates well the condition of an infinite thickness, so it can be generally used in experimental conditions.[166]

However, in order to obtain the actual absorption spectrum of the sample, the scattering coefficient S must be independent of wavelength, which has been verified for solid particles possessing an average grain size of about 1 μm; on the contrary, if a significant fraction of the particles is smaller than that, S shows a decrease with increasing wavelength, which leads to a flattening of the pseudoabsorbance spectrum, relative to real absorption behavior. Moreover, the absorption coefficient K decreases with increasing particle size, even though the size-dependance and its effect on reflectance measurements is different for weakly and strongly absorbing materials; anyway, the distortion is more severe when there are coarse and strongly absorbing particles.

As regards the experimental setup, reflectance measurements are performed with an internal standard, constituted by a highly reflecting substance, such as $BaSO_4$, which is subject to the same illumination conditions of the solid under investigation; the sample itself can be deposited onto a layer of the same standard material. R_∞ can be expressed as a fraction or as a percentage, although the quantity which is measured in reality is the ratio between R_∞ of the sample and R_∞ of the standard:

$$R'_\infty = \frac{R_{\infty(sample)}}{R_{\infty(standard)}} \quad (18)$$

If $K = 0$ for the standard, for the entire spectrum, that is, the standard is totally reflecting, then the experimental reflectance corresponds to that of the sample.

A diffuse reflectance spectrophotometer is represented schematically in **Figure 2.7**:

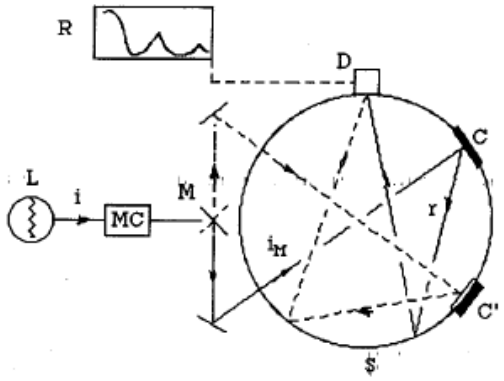

Figure 2.7 A reflectance spectrophotometer: L represents radiation source, MC is a monochromator, M is an oscillating mirror, S is the integrating sphere, C and C′ are, respectively, sample and standard, D is the detector and R is a recorder.

The reflected radiation is collected by an *integrating sphere*, S, covered by a reflecting substance, which could be the same as the standard; the mirror M sends radiation to C and C′ alternately, then, both the radiation reflected by the sample and by the standard are directed onto the detector.

An example of a reflectance spectrum, together with the corresponding pseudoabsorbance spectrum, is reported in **Figure 2.8**.

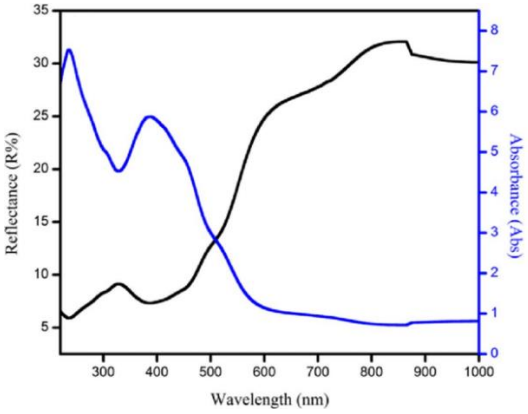

Figure 2.8 Diffuse reflectance (black curve) and absorbance spectrum (blue curve) for a semiconductor material ($LaFeO_3$).

For semiconductors, and thus also for hybrid perovskites, measurement of diffuse reflectance spectrum allows the determination of the band gap,[167] which is crucial in order to assess their suitability as absorbing materials in solar cells. The determination is made by means of the Tauc plot, which is obtained from the reflectance spectrum, converted

into the pseudoabsorbance spectrum, by applying the Kubelka-Munk function, equation (17). [168,169]

The following expression has been proposed by Tauc, which relates the energy-dependent absorption coefficient α to the band gap energy E_g:

$$(\alpha h\nu)^{\frac{1}{\gamma}} = B\left(h\nu - E_g\right) \quad (19)$$

where h is the Planck constant, ν is the frequency of radiation, B is a constant and γ is a factor depending on the nature of the electron transition,[170] whether direct or indirect, allowed or forbidden, and, in particular, γ = 1/2 for a direct allowed transition, γ = 2 for an indirect allowed transition, γ = 3/2 for a direct forbidden transition and γ = 3 for an indirect forbidden transition.

If the reflectance $F(R_\infty)$ is substituted for α in equation (19), then the relation becomes:

$$(F(R_\infty)h\nu)^{\frac{1}{\gamma}} = B\left(h\nu - E_g\right) \quad (20)$$

and the band gap value can be obtained by plotting the pseudoabsorbance, transformed according to equation (20), against photon energy $h\nu$ and subsequently drawing the tangent line to the inflection point of the obtained curve, as shown in **Figure 2.9**: the point of intersection of the tangent line with the horizontal axis gives the energy value of band gap.

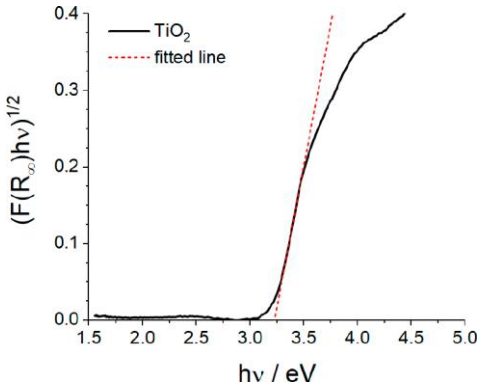

Figure 2.9 Tauc plot for TiO_2, an indirect band gap semiconductor, and determination of band gap value (reproduced from ref. 167).

If the type of transition is not known, it is possible to try different values for γ and verify which one fits best the experimental energy value of absorption edge in the pseudoabsorbance spectrum.

All the diffuse reflectance UV-visible spectra reported in the present work were performed with a Shimadzu (Japan) UV2600 UV-vis spectrophotometer, equipped with an ISR-2600 Plus integrating sphere, by using $BaSO_4$ as a reference.

Chapter 3: Synthesis and characterization of $AEPyPb_2I_6$

3.1 Synthesis and characterization of the organic salt $AEPyI_2$

Among the extended viologen structures shown in **Figure 2.3**, Chapter 2, our choice was to start with the preparation of the iodide salt of **1**, featuring an anthracenic core; its structure is shown in **Figure 3.1**:

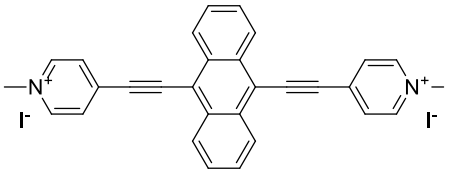

$1I_2$ ($AEPyI_2$)

Figure 3.1 Structure of **$1I_2$** salt (**$AEPyI_2$**).

The synthesis could be conveniently accomplished in four steps, making use of successive Pd-Cu catalyzed Sonogashira cross-coupling reactions,[171,172] employing commercially available building blocks, namely 9,10-dibromoanthracene, trimethylsilylacetylene (TMSA) and 4-bromopyridine (stabilized as hydrochloride).

3.1.1 Synthesis

As a first step, 4-bromopyridine was reacted with trimethylsilylacetylene, following a literature procedure,[173] as shown in **Scheme 3.1**, thus affording the desired trimethylsilyl-protected 4-ethynylpyridine **1a** as a light brown oil, with a yield of 60%, after purification through column chromatography.

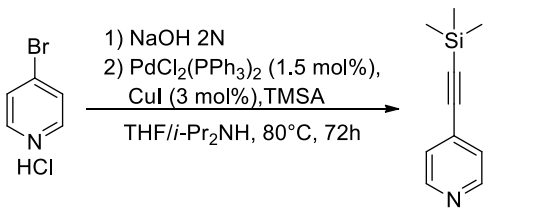

1a (60%)

Scheme 3.1

The trimethylsilyl-group was subsequently cleaved in basic conditions, again following the same reported procedure, by treating **1a** with a K_2CO_3 methanolic solution (**Scheme 3.2**), leading to 4-ethynylpyridine **1b** with a quantitative yield; the crude product, a white, photosensitive solid, resulted to be sufficiently pure for use in the next step, without the need of further purification.

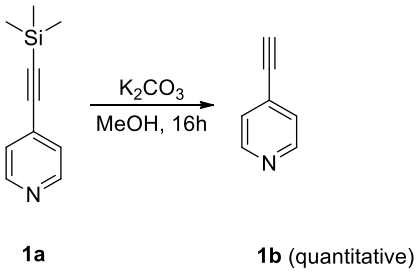

Scheme 3.2

Thus, 4-ethynylpyridine **1b** was reacted with 9,10-dibromoanthracene, according to a literature procedure,[174] in another Pd-Cu catalyzed Sonogashira reaction, as **Scheme 3.3** shows, yielding the target bipyridine compound **1c**, regretfully accompanied by a non-negligible amount of the byproduct **1d**, resulting from the coupling between 9,10-dibromoanthracene and a single molecule of 4-ethynylpyridine. The mixture containing **1c** and **1d** was however separated of column chromatography, allowing the isolation of the desired **1c**, as an orange solid, with a yield of 35%.

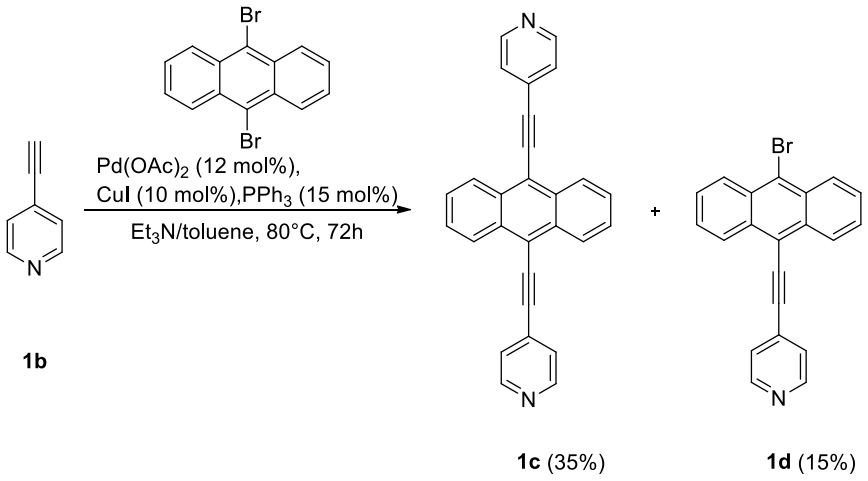

Scheme 3.3

Finally, the last synthetic step consisted in the quaternarization of nitrogen atoms of compound **1c**, leading to the formation of the corresponding bipyridinium salt **1I$_2$**; as already anticipated in the previous chapter, the formation of the dication was accomplished through a substitution reaction on pyridine nitrogen by methyl iodide. The reaction on **1c**, in **Scheme 3.4**, was carried out following a modified literature procedure,[175] in refluxing CH_2Cl_2 with an excess of methylating agent, affording compound **1I$_2$**, which will be referred to, from now onwards, as **AEPyI$_2$**. The bipyridinium salt was obtained with a yield of 72%, as a dark red solid; since it is insoluble in CH_2Cl_2, it precipitated upon formation and could be isolated from the solution through filtration, with high purity, without the need of further purification.

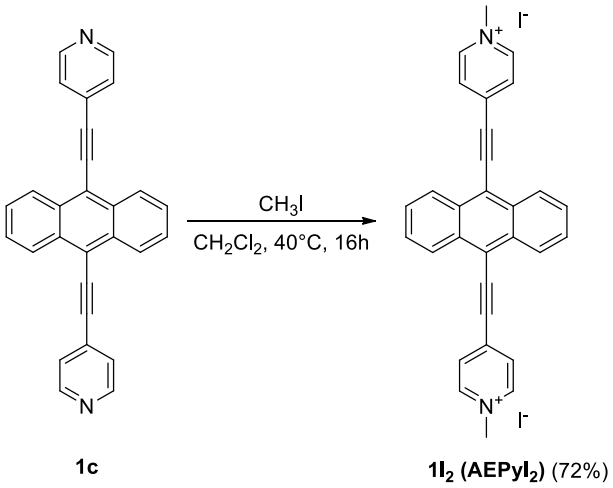

Scheme 3.4

3.1.2 Physico-chemical characterization

Once the organic salt was synthesized, and its structure and purity were assessed through ^{1}H-NMR, ^{13}C-NMR (see Appendix) and ESI-MS, shown in **Figure 3.2**, both in positive and negative mode, we dedicated to its physico-chemical characterization, focusing in particular on those properties which are the most desirable in compounds intended for the preparation of hybrid perovskite semiconductors, such as light absorption and emission and thermal stability.

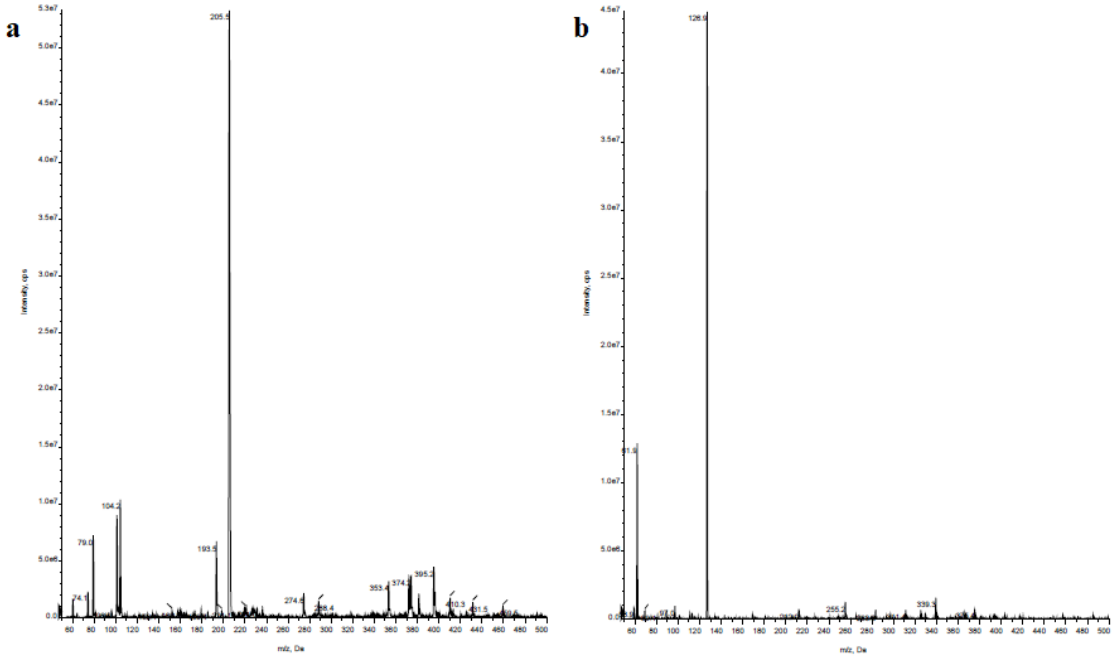

Figure 3.2 a) positive mode and **b)** negative mode ESI-MS spectra in methanol of **AEPyI$_2$**.

We immediately noticed a very intense fluorescence in **AEPyI$_2$** aqueous solution, as it can be seen in **Figure 3.3**, so we performed UV-visible absorption spectrum, both in solution and in the solid state (diffuse reflectance spectrum): the comparison between the two spectra allowed us to observe the possible presence of a charge-transfer complex from iodide anion to organic cation, a feature which has been already mentioned (Chapter 2, section **2.1.1**) for viologens and extended viologens.

Both spectra (absorbance in solution and pseudoabsorbance) for **AEPyI$_2$** are reported in **Figure 3.4**; as shown, the solid-state spectrum presents an additional absorption band, for $\lambda > 560$ nm, relative to that in solution, probably due to the occurrence of a charge-transfer process, which is not present in solution, due to ion solvation.

Figure 3.3 Fluorescence of **AEPyI$_2$** in aqueous solution, under excitation with a 365 nm lamp.

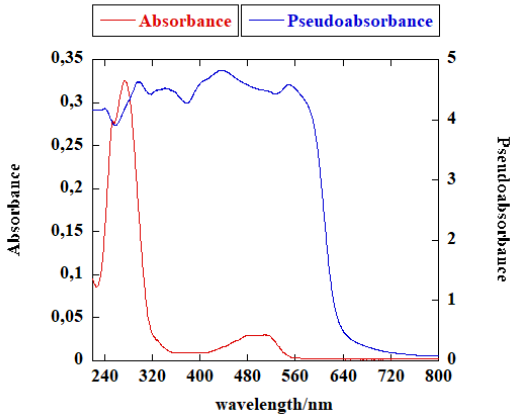

Figure 3.4 Absorbance in H_2O solution, c = $4.2x10^{-5}$ M (red curve) and pseudoabsorbance (blue curve) obtained by application of the K.M. function to reflectance data for **AEPyI$_2$**.

Given the intense emission of the compound in the visible region, shown qualitatively in **Figure 3.3**, its fluorescence spectrum in water was also measured, for two different excitation wavelengths: 274 nm, which is the absorption maximum of the most intense absorption band in solution, and a slightly greater wavelength, that is, 300 nm; the two fluorescence spectra of **AEPyI$_2$** are reported in **Figure 3.5**.

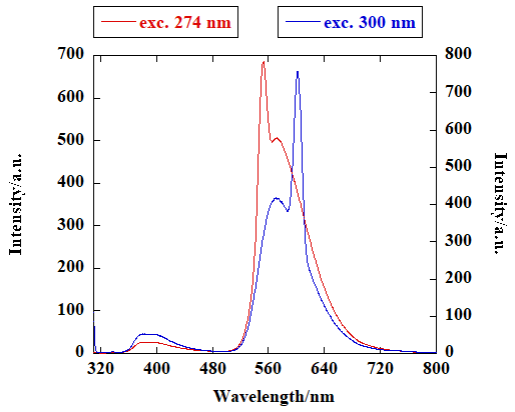

Figure 3.5 Fluorescence spectra of **AEPyI$_2$** in H_2O solution, c = $1.8x10^{-4}$ M.

Both the spectra show a very weak fluorescence between 350 and 450 nm, followed by a broad and extremely intense emission band for λ > 500 nm, clearly comprising multiple transitions, the relative intensities of which are different for different excitation wavelengths.

After evaluating UV-visible absorption and emission for compound **AEPyI$_2$**, another very important information that was needed, in view of the preparation of its

iodometallates and their possible optoelectronic applications, was about its stability to high temperatures; therefore, a TG-DTA experiment, in flowing Ar atmosphere, was carried out and the result is shown in **Figure 3.6**.

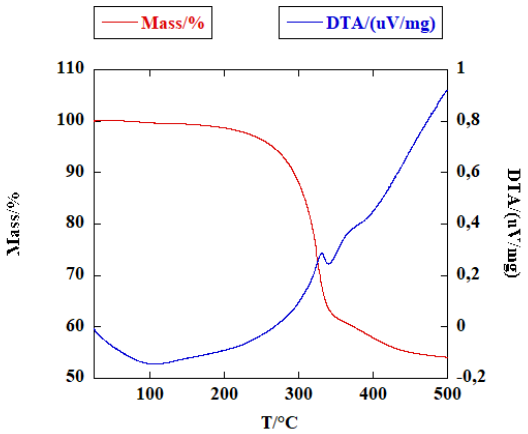

Figure 3.6 TG-DTA curve of **AEPyI$_2$**.

From the TG-DTA curve, no sign of decomposition or other thermal events can be noticed up to a temperature of about 300° C, after which an absorption of energy takes place, as it is apparent from the sharp endothermic peak, which is accompanied by a very steep decrease in mass, rapidly falling to about 60% of its initial value. The compound **AEPyI$_2$** shows, then, an excellent thermal stability, a highly desirable quality for its utilization in hybrid perovskites; the preparation and characterization of a lead iodide perovskite with **AEPyI$_2$** salt will be discussed in the next section.

3.2 Synthesis and characterization of lead perovskite AEPyPb$_2$I$_6$

In order to prepare the perovskite, first of all, a suitable solvent had to be found in which to dissolve the precursor organic salt: as seen while illustrating the characterization of **AEPyI$_2$**, this compound is soluble in H_2O, with a solubility of about 13 mg/mL, so a saturated **AEPyI$_2$** H_2O solution was prepared and slowly added to a solution in acetone (so that solvent volume ratio after mixing of the two solutions was 1:3 H_2O:acetone) containing an equimolar amount of PbI_2, together with an excess of NaI to allow PbI_2 dissolution through complexation.

$$\mathbf{AEPyI_2} + 2PbI_2 + 3NaI \rightarrow \mathbf{AEPyPb_2I_6} \quad (21)$$

Immediate precipitation of a dark solid and its subsequent filtration afforded the perovskite **$AEPyPb_2I_6$** (the stoichiometry of which was assessed by elemental analysis), as a black powder, as shown in **Figure 3.7**.

Figure 3.7 Precipitated **$AEPyPb_2I_6$** powder.

The identity of the perovskite was verified by ESI-MS spectra in methanol, shown in **Figure 3.8**, both in positive and negative mode: the positive ions mass spectrum features peaks at 205 m/z, owing to the organic dication, and 395 m/z, for the monocationic species derived by the loss of a CH_3 fragment, while the negative mode shows the exclusive presence of iodide as halide species (as I^-, I_3^- and $Pb_2I_6^{2-}$ cluster).

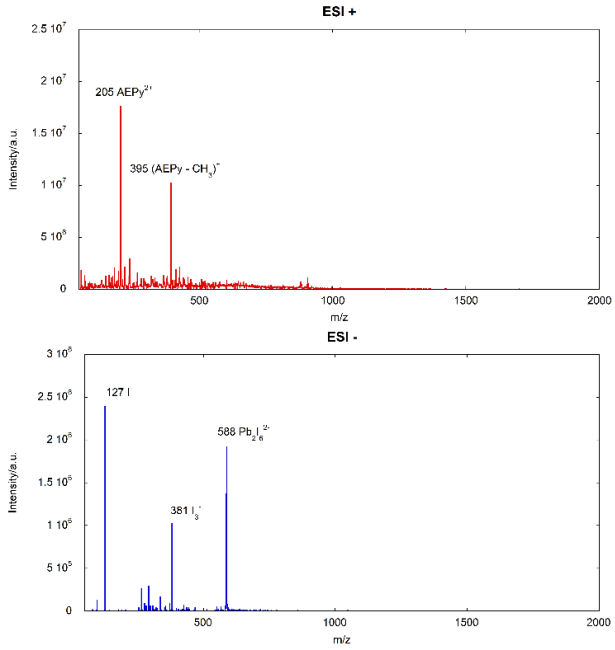

Figure 3.8 ESI-MS spectra of **$AEPyPb_2I_6$**, in positive (top) and negative mode (bottom).

3.2.1 Environmental and thermal stability

AEPyPb$_2$I$_6$ showed an excellent environmental stability, as confirmed by its ^{1}H-NMR spectrum in d_6-DMSO, shown in **Figure 3.9**, performed on the perovskite stored in ambient air at room temperature, for some months after its preparation, superimposed to that of a freshly prepared sample: the signals, belonging to the organic cation, are the same in both spectra, thus proving that **AEPyI$_2$** does not undergo any modification when embedded in the metal halide framework.

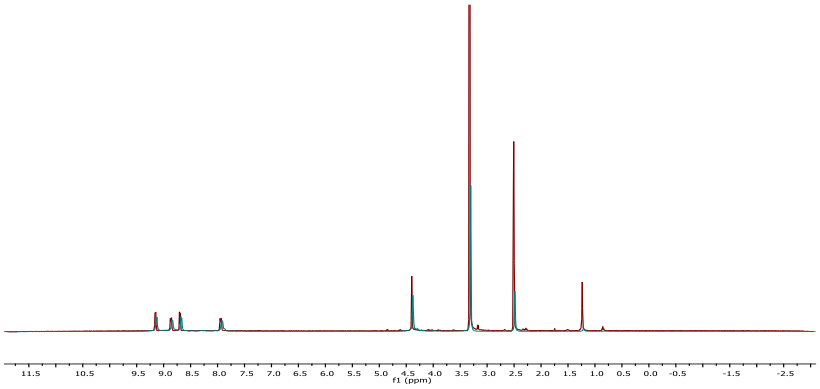

Figure 3.9 ^{1}H-NMR spectra of a freshly prepared sample of **AEPyPb$_2$I$_6$** (blue line) and a sample stored for months at room temperature in ambient air (red line).

On the contrary, the ^{1}H-NMR spectrum of the organic salt alone, stored for some months in the same conditions, shown in **Figure 3.10**, displays the appearance of additional signals, suggesting some degree of degradation.

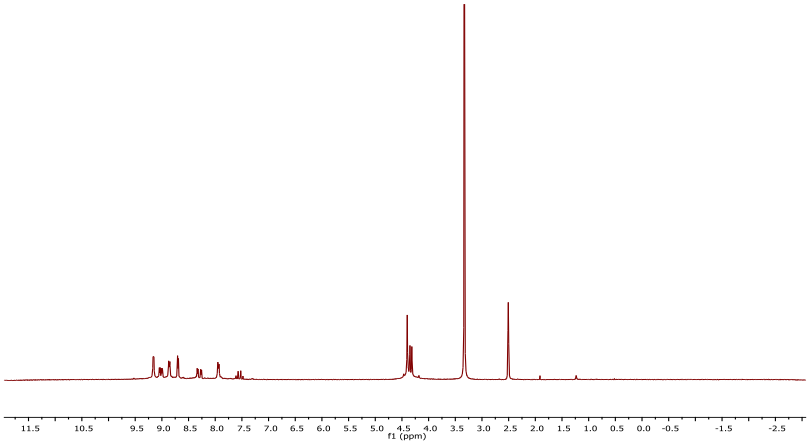

Figure 3.10 ^{1}H-NMR spectrum of a sample of **AEPyI$_2$** stored for months at room temperature in ambient air.

Most notably, **AEPyPb$_2$I$_6$** is exceptionally moisture-tolerant, thanks to the absence of hydrolysable protons, as already highlighted in the previous chapters, and in addition, the water solubility of the precursor organic salt allows its synthesis from an aqueous solution.

Thermal stability of the perovskite was also tested, through thermogravimetry-differential thermal analysis, as **Figure 3.11** shows; the material, as seen previously for the precursor organic salt, resulted to be remarkably stable to high temperatures, in argon atmosphere, since its mass starts to decrease just above 300° C, similarly to **AEPyI$_2$**, so the endothermic event taking place at that temperature is easily attributable to the decomposition of the organic species.

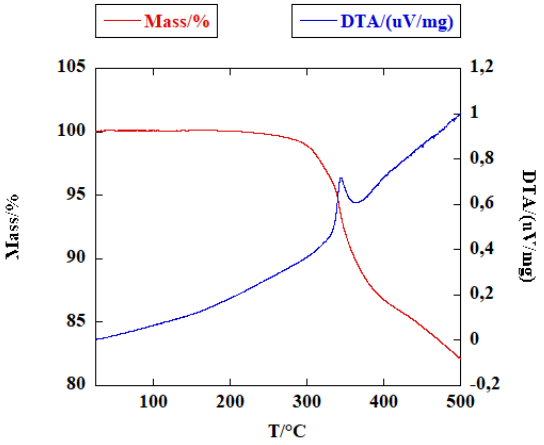

Figure 3.11 TG-DTA curve of **AEPyPb$_2$I$_6$**.

3.2.2 Powder X-ray diffraction and crystallization

On the perovskite powder obtained, as previously described, by precipitation from precursor solutions and subsequent filtration, powder X-ray diffraction was also carried out; **AEPyPb$_2$I$_6$** diffractogram, in **Figure 3.12**, shows the crystalline nature of the powder.

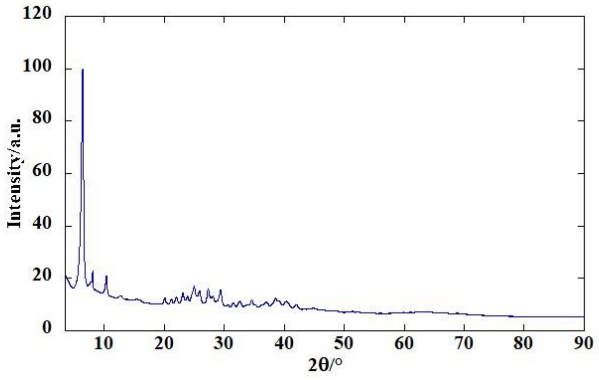

Figure 3.12 X-ray diffraction pattern of precipitated **AEPyPb$_2$I$_6$**.

Moreover, in order to test the suitability of **AEPyPb$_2$I$_6$** for thin film deposition, which is crucial for optoelectronic applications, a test was made using a spray deposition technique of a saturated solution in DMF (100 mg/80 mL), on a microscope glass slide kept at 160 °C. The film obtained resulted to be constituted only of the perovskite, with no decomposition products, as demonstrated by thin-film XRD: the pattern of the film, reported in **Figure 3.13**, was superimposable with the one obtained from powder, shown in **Figure 3.12**, demonstrating so the possibility of obtaining films of **AEPyPb$_2$I$_6$** from solutions.

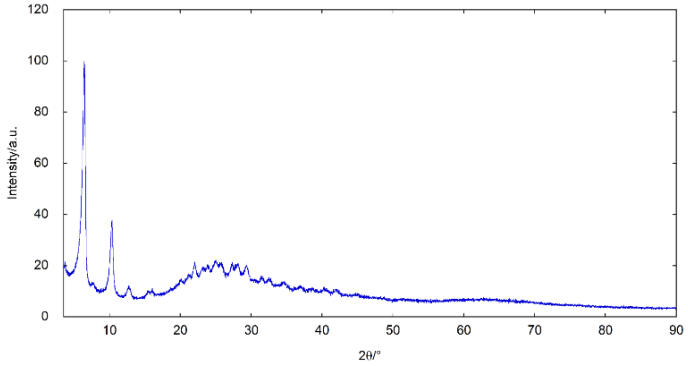

Figure 3.13 X-ray diffraction pattern of a thin film of **AEPyPb$_2$I$_6$** on a glass slide.

Nevertheless, the growth of single crystals possessing suitable dimensions for crystal structure determination by X-ray diffraction proved to be extremely challenging, and we did not manage to accomplish it, although we attempted with a number of different techniques and solvent combinations. At first, crystal growth was tried by using the vapor diffusion method, consisting in the exposition of a saturated solution of the compound to

be crystallized, dissolved in an appropriate solvent, to vapors of an antisolvent, which must have a higher vapor pressure than the solvent, in a closed container. Various mixtures were employed in our attempts: at first, DMF (*N*,*N*-dimethylformamide) was used as a solvent and CH_2Cl_2 as an antisolvent, since this is the most practiced solvent combination for this kind of compounds, indeed giving satisfactory results in the case of other hybrid perovskites we were able to crystallize. Given the unsuccessful outcome, a different dipolar aprotic solvent was chosen, namely DMI (1,3-dimethyl-2-imidazolidinone), a cyclic urea, again in combination with CH_2Cl_2 as an antisolvent. Finally, given that not even this combination had afforded suitable crystals, it was decided to substitute the antisolvent with a less volatile one, with the hope that a slower diffusion into the perovskite solution would have led to a better crystal accretion: therefore, a DMF solution of **AEPyPb$_2$I$_6$** was exposed to vapors of α,α,α-trifluorotoluene, possessing a similar dielectric constant to CH_2Cl_2, that is, 9.18 (while for CH_2Cl_2 it is 9.04) but a very different boiling point of 102° C, compared to about 40° C for dichloromethane.[176]
However, also in this last case, the dimensions of the obtained crystals were not large enough to allow structure determination from X-ray diffraction, so a different crystallization technique was tested and, in particular, crystal growth was tried at the interface between two liquids: in other words, a solution containing the perovskite and an antisolvent with a different density were carefully introduced in a glass vial allowing them to stratify. Two solvent-antisolvent combinations were used with this method, namely DMF and dichloromethane, and sulfolane (10% wt H_2O) as a solvent, with toluene as an antisolvent; however, in both trials, the collected crystals did not possess the desired size. Lastly, hydrothermal conditions were employed in an attempt to obtain **AEPyPb$_2$I$_6$** as crystals of adequate dimensions directly upon its formation: to do so, the organic salt **AEPyI$_2$** was inserted into a hydrothermal bomb, together with $Pb(NO_3)_2$ and LiI, in a 95:5 CH_3OH/H_2O mixture; the compounds were reacted at 145° C for 72 h, then the mixture was filtered and the collected solid was subjected to powder diffraction in order to identify it; unfortunately, the analysis revealed a mostly amorphous material, in which a few peaks could be hardly noticed. Subsequently, similar hydrothermal conditions were tested on the already synthesized perovskite, with the precipitation method previously explained, in an extreme attempt to achieve crystal accretion, nevertheless without any success.

3.2.3 3D electron diffraction for crystal structure determination

The lack of suitable single crystals forced us to resort to an alternative technique, in order to determine **AEPyPb$_2$I$_6$** crystal structure, which was essential for complete characterization of the material; solution of the structure could be achieved either by powder methods or by electron diffraction.

As previously remarked (Chapter 2, section **2.2.1**), the use of PXRD for structure determination is an extremely complicated matter, and it results particularly challenging for substances possessing low-symmetry space groups and very large unit cells, especially if containing bulky organic species in combination with a great number of heavy atoms (featuring higher scattering factors), which could completely obscure the contribution from the organic portion. In light of this, the only chance to solve this structure exclusively by powder methods would have been to perform a neutron powder diffraction experiment, since neutron scattering factors are not directly correlated to the atomic number; this technique, nonetheless, would have required the preparation of a totally deuterated **AEPyI$_2$** sample, which was not economically, and practically, feasible.

Thus, the determination of **AEPyPb$_2$I$_6$** crystal structure was tried, and successfully achieved, by means of 3D electron diffraction, performed on single crystals of submicrometric size, grown by us in silanized glass vials by vapor diffusion crystallization from DMF/CH_2Cl_2 solvent/antisolvent system.

Electron diffraction measurements and structure determination were accomplished by Dr. Mauro Gemmi and his research group, at the Center for Nanotechnology Innovation@NEST, Istituto Italiano di Tecnologia, in Pisa (Italy).

In fact, 3D ED (electron diffraction) proved to be a reliable method for structure determination,[177] for phases crystallizing with the formation of submicrometric grains, which therefore do not allow X-ray diffraction from single crystal, and for this reason it has found wide application in case of hybrid structures.[178] The protocol, which is adopted in these situations, combining data attained by powder XRD with those from 3D ED, consists of the following steps: first, any newly synthesized substance is characterized by X-ray powder diffraction, then, if its diffraction pattern cannot be fully indexed with known structures, 3D ED data are collected from a certain number of single nanocrystals, to identify the new phase present in the sample and to determine the size of the related

unit cell; finally, if an unknown phase is found, its crystal structure is solved by 3D ED and refined by Rietveld refinement against PXRD.

Experimentally, 3D ED data were recorded with a transmission electron microscope in STEM mode, from several crystal fragments with sizes less than 1 μm, like the sample in **Figure 3.14a**, shown in high-angle annular dark-field scanning transmission electron microscopy (HAADF-STEM)[179] imaging mode. This is a very sensitive technique to variations in atomic number in the sample,[180] and it is performed with an annular dark field detector; in this mode, incoherently scattered electrons from the nucleus of the atoms at very high angle are collected and used to produce an image.

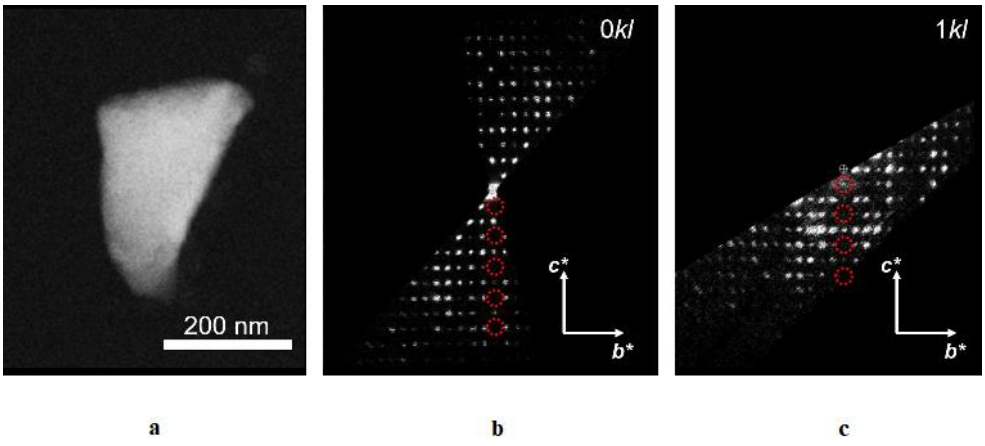

Figure 3.14 a) High angle annular dark field STEM (HAADF-STEM) image of an **$AEPyPb_2I_6$** single crystal used for 3D ED data collection; **b)** and **c)** selected planar cuts, from the two 3D ED datasets chosen for the integration of reflection intensities, of the 3D reciprocal space reconstruction of **$AEPyPb_2I_6$**, revealing extinction conditions *h0l*: *l*=2*n* (red circles).

All the collected datasets showed, in a consistent way, the same primitive monoclinic unit cell; among those, the two displaying the largest angular tilt range and without artefacts induced by polycrystallinity were selected for the structure determination. The rough cell parameters obtained from 3D ED are *a*=4.7 Å, *b*=23.0 Å, *c*=17.8 Å and *β*=105.0°. The cell parameters were further refined and validated with a Le Bail fitting against XRPD, which provided the following values: *a*=4.6628(5) Å, *b*=22.902(4) Å, *c*=17.696(4) Å and *β*=105.3477(3)°. From reciprocal space sections on 3D ED data, the following extinction condition was revealed, for *h0l*: *l*=2*n*, as shown in **Figure 3.14b** and **c**, indicating in a convincing way a monoclinic space group *Pc* (7) or *P*2/*c* (13). Reflection intensities

extracted from both datasets were merged, according to the observed Laue symmetry and by a scale factor, which was derived from the comparison of the strongest reflections in common.

A two-step approach was followed for the solution of crystal structure: Pb-I inorganic clusters were obtained first, by standard direct methods (SDMs) which automatically furnished the position of two Pb and six I atoms in the asymmetric unit, shown in **Figure 3.15**; subsequently, two independent **AEPy**$^{2+}$ cations were added by simulated annealing (SA).

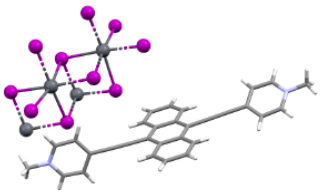

Figure 3.15 Asymmetric unit of **AEPyPb$_2$I$_6$** crystal.

The molecular model was deduced from structure CCDC 2181402, containing the same cation (that is, bismuth perovskite **AEPy$_3$Bi$_4$I$_{18}$**, the synthesis and characterization of which will be discussed in the next chapter) and modelled as a unique fragment. No anti-bump restraint was used; this method was applied with success, in the past, to 3D ED data for structure determination of a covalent organic framework[181] and important pharmaceuticals.[182,183]

Structure solution attempts in space group *P*2/*c* (13) resulted unstable and could not be refined: the best crystallographic model was obtained then in space group *Pc* (7) and further kinematically least-squares refined against 3D ED data, by imposing constraints on the aromatic rings and the assignment of all hydrogen atoms to calculated positions. Additionally, restraints were imposed on Pb-I interatomic distances and the planarity of the flat portions contained in the molecule.

Further details about structure determination and refinement are reported in **Table 3.1**.

The high R-value of the kinematical refinement can be expected, due to the unavoidable presence of dynamical scattering, which is higher when heavy atoms are present, and must be imputed to imperfections in the data collection, related to the small crystal size

and to the beam movement over different positions of the same crystal, in order to reduce the beam damage.

The obtained 3D ED structural model was subsequently improved by Rietveld refinement on PXRD data, shown in **Figure 3.16**: the refinement converged to R_{wp} = 5.32%, R_F(obs) = 17.41%, wR_F(obs) = 18.49% without any significant modification, as it can be seen in the figure.

The final structure model, oriented along the *a* axis, is shown in **Figure 3.17a**: the **AEPyPb$_2$I$_6$** crystal structure is characterized by well separated Pb_2I_6 double chains of edge-sharing octahedra, developing along the *a* direction, while in the *b*-*c* plane they are arranged in an almost centered lattice, leaving room for the **AEPy^{2+}** cations, which are stacked in the same *a* direction through π-π interactions; the arrangement of the organic cations and the lead iodide chains are represented in **Figure 3.17b** and **c**, respectively. Considering the type of structure, which, as seen in Chapter 1, section **1.5.2**, can be regarded as a 1D perovskite structure, the obstacles encountered in growing crystals can be probably motivated with the formation, by the inorganic lattice, of a polymeric motif, which, in combination with the large organic cation, makes crystal packing difficult.

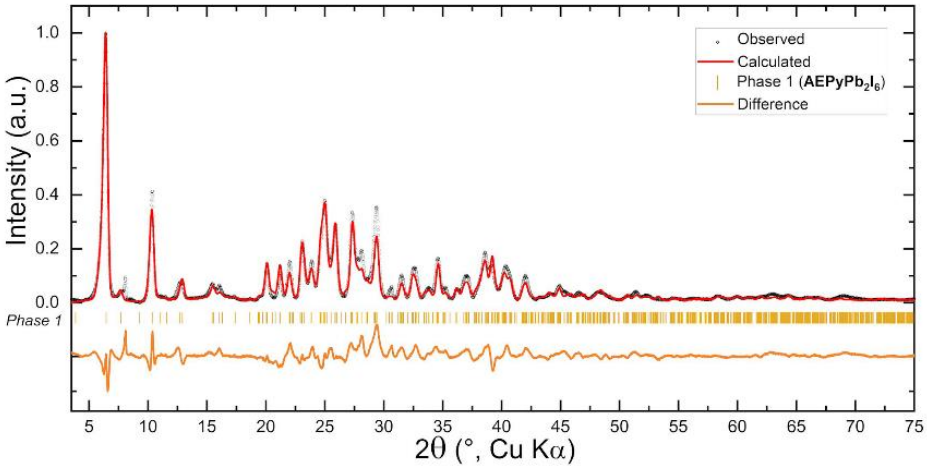

Figure 3.16 Final profile fit obtained by a Rietveld refinement on **AEPyPb$_2$I$_6$**, performed starting from the structural model obtained by 3D ED.

Crystallographic information	
Asymmetric unit content	$C_{30}H_{22}N_2Pb_2I_6$
Z	2
Space group	*Pc* (7)
a (Å)	4.6628(5)
b (Å)	22.902(4)
c (Å)	17.696(4)
β (°)	105.3477(3)
Volume ($Å^3$)	1823.804(6)
Structure solution parameters (*SIR2014*)	
Data resolution (Å)	0.9
No. of sampled reflections	5392
No. of independent reflections	2180
Independent reflections coverage (%)	81
Global thermal factor *U*iso (Å2)	0.03045
*R*int(*F*) (%)	18.95
CF (%)	36.371
Structure refinement parameters (*SHELXL*)	
Data resolution (Å)	0.9
*R*int(*F*2) (%)	30.87
No. of reflections (all)	5219
No. of reflections (>4σ)	871
*R*1 (4σ) (%)	34.50
Goodness-of-fit	1.334
Structure refined parameters – PXRD (JANA 2006)	
Data resolution (Å)	1.09
Rp	3.50
wRp	5.32
No. of reflections (all)	2987
No. of reflections (>3σ)	2819
R(3σ) (%)	17.41
wR (3σ) (%)	18.49

Table 3.1 Selected parameters from structure solution (*SIR2014*) and refinement (*SHELXL*) based on the 3D ED data.

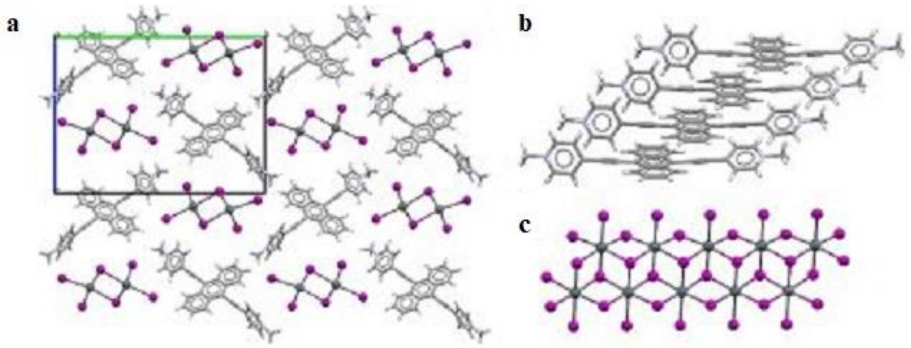

Figure 3.17 a) Crystal structure of **$AEPyPb_2I_6$** seen along the *a*-axis, with the indication of the unit cell; **b)** molecular packing of **$AEPy^{2+}$** units; **c)** representation of Pb_2I_6 double chains (grey: Pb, purple: I).

3.2.4 UV-visible absorption and photoluminescence spectroscopy

The optical and electronic properties of the material were studied by a series of experiments and theoretical characterizations; first of all, the UV-visible absorption was determined, by UV-visible diffuse reflectance spectroscopy measurement, as seen previously: the pseudoabsorbance spectrum thus obtained is shown in **Figure 3.18a**. From the pseudoabsorbance spectrum, it was possible to calculate the Tauc plot, shown in **Figure 3.18b**, through which an optical band gap of 1.6 eV was estimated, by assuming a direct optical transition.

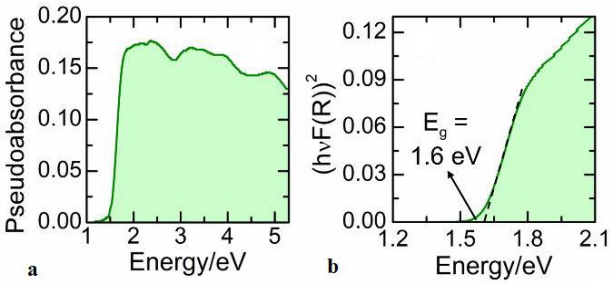

Figure 3.18 a) Pseudoabsorbance spectrum of **$AEPyPb_2I_6$**; **b)** Tauc plot, assuming a direct optical transition, for the determination of the band gap value E_g.

The emission efficiency of the perovskite was extensively investigated by photoluminescence (PL) spectroscopy studies, performed on samples of **$AEPyPb_2I_6$** powder; notably, PL and Raman measurements (described in the next section) were

carried out by Dr. Elena Blundo, and Prof. Antonio Polimeni's research group, at the Department of Physics, Sapienza University of Rome.

Figure 3.19 shows the PL spectrum of the perovskite, represented by the light green curve; the spectrum was acquired with a Si charge coupled device (CCD) and the system response was properly taken into account: since the system response drops at ~1.2 eV, the spectrum is shown only up to that energy value; however, in order to verify that no lower energy states were present, the PL signal was measured also by an InGaAs linear array.

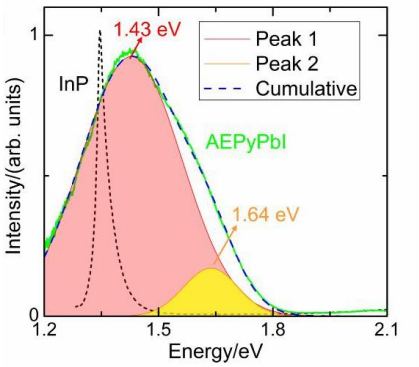

Figure 3.19 $AEPyPb_2I_6$ PL spectrum (light green curve) and corresponding fit (dashed curve) with two gaussian functions (pink and yellow); the PL spectrum of a InP epilayer standard, acquired under analogous conditions (dotted curve), is also shown as a comparison.

The spectrum in **Figure 3.19** can be fitted with two gaussians, centered at 1.43 eV (pink) and 1.64 eV (yellow). The PL emission of the perovskite is remarkably high, as revealed by the comparison with the intensity of the PL signal of a standard, constituted by a high-quality 3-micron-thick (100) InP epilayer, grown by metal-organic chemical vapor deposition at a temperature of 650° C (represented by the black dotted line). **$AEPyPb_2I_6$** and the InP epilayer show similar peak intensities, while the integrated area of the PL signal of the material under investigation is about one order of magnitude larger than that of InP.

Additionally, to get further quantitative information on the PL intensity of **$AEPyPb_2I_6$**, its spectrum was also compared with the PL signal of $CH_3NH_3PbI_3$ perovskite, and the results are shown in **Figure 3.20**.

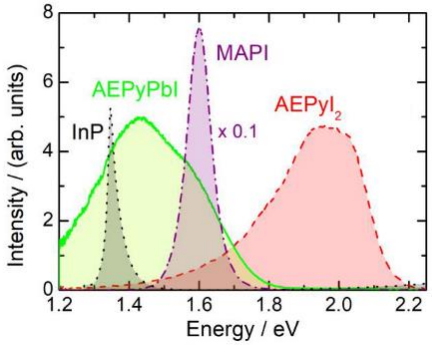

Figure 3.20 Comparison between PL spectra for **$AEPyPb_2I_6$** (green), $CH_3NH_3PbI_3$ (purple), **$AEPyI_2$** (red) and InP (black).

The integrated area of the PL signal of $CH_3NH_3PbI_3$ (MAPI) exceeds that of **$AEPyPb_2I_6$** of about 3.1 times, confirming a high PL efficiency for the new perovskite; the PL external quantum yield of the perovskite synthesized by us was also measured and compared to that of MAPI:[184,185,186] the obtained values are of 17% and 25%, respectively, for **$AEPyPb_2I_6$** and $CH_3NH_3PbI_3$, thus suggesting a good PL efficiency for this new material, though slightly lower than that of methylammonium. Moreover, in **Figure 3.20**, the PL spectrum for **$AEPyI_2$** is also reported: the organic salt shows a bright PL signal, which is centered at higher energy (~1.97 eV) than that of the corresponding perovskite. Finally, the robustness of the perovskite upon photoexcitation was also tested, by performing PL measurements at increasingly higher excitation powers, from 44 nW to 900 μW; the experiments were carried out by focusing the laser through a 20x objective with NA = 0.4. As shown in **Figure 3.21**, no lineshape variations are observed until 200 μW, which demonstrates the robustness of **$AEPyPb_2I_6$** against photoexcitation; at higher powers, however, a broadening is observed, followed by a quenching of the PL intensity, owed to degradation of the material.

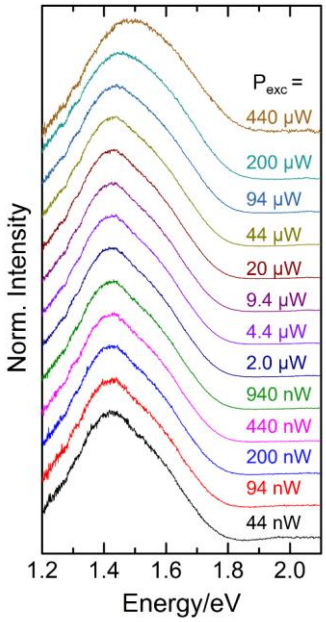

Figure 3.21 PL spectra of **$AEPyPb_2I_6$** as a function of the excitation laser power.

3.2.5 FTIR and Raman spectroscopy

The vibrational properties of **$AEPyPb_2I_6$** were investigated by Raman and Fourier transform infrared (FTIR) spectroscopies; in **Figure 3.22**, the experimental Raman and FTIR spectra are compared with a simulated IR spectrum, obtained by density functional perturbation theory (DFPT) calculations:[187] overall, a good agreement between the experimental data and the computation is observed.

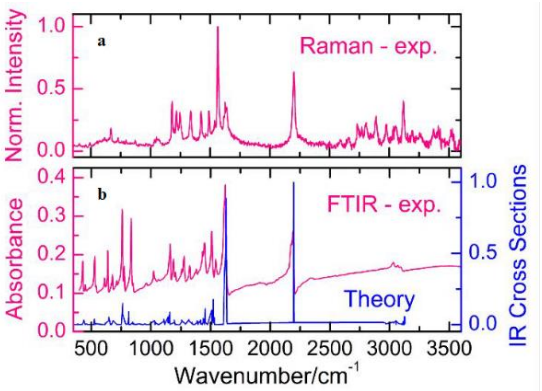

Figure 3.22 a) Raman spectrum and **b)** experimental FTIR spectrum of **$AEPyPb_2I_6$**; in **b)** experimental data (purple) are compared to IR spectrum calculated by DFPT (blue).

AEPyPb$_2$I$_6$ shows vibrational features deriving from the oscillations of the different components of the perovskite. The low energy portion of the spectrum (not shown in **Figure 3.22**), below 100 cm^{-1}, is mostly characterized by the bending and stretching of the inorganic portion; vibrational modes between 100-200 cm^{-1} are associated with the torsion of the organic cations within the 1D channel of the perovskite, while the frequency region between 200-600 cm^{-1} shows primarily the bending of the organic cation; beyond 600 cm^{-1} only the stretching modes of the latter are present. As regards the most intense peaks around 1600^{-1} and 2200 cm^{-1}, they are associated to the stretching of the aromatic rings and triple C-C bond, respectively.

3.2.6 Computational study

In order to correlate the nature of the optical excitations in the **AEPyPb$_2$I$_6$** perovskite to its electronic structure, density functional theory (DFT) calculations were also performed. All the theoretical calculations were carried out by Dr. Daniele Meggiolaro, at the Computational Laboratory for Hybrid/Organic Photovoltaics (CLHYO), Istituto CNR di Scienze e Tecnologie Chimiche "Giulio Natta" (CNR-SCITEC), in Perugia, (Italy).

The electronic band structure and the projected density of states (PDOS) of **AEPyPb$_2$I$_6$** were calculated by using the Perdew-Burke-Ernzerhof (PBE) functional[188] and including spin-orbit coupling (SOC); the results are shown in **Figure 3.23**.

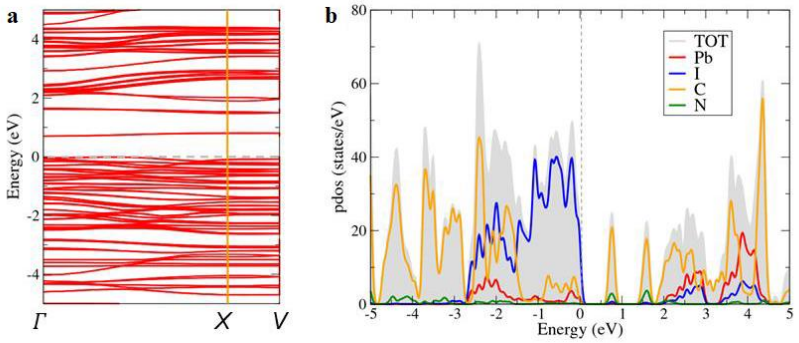

Figure 3.23 a) Electronic band structure of **AEPyPb$_2$I$_6$**; **b)** projected density of states (PDOS) of **AEPyPb$_2$I$_6$** calculated by using the PBE functional and by including spin-orbit coupling (SOC).

At this level of theory, the perovskite shows an indirect band gap, with a value of 0.71 eV. The analysis of the PDOS indicates that the valence band maximum (VBM) is derived

primarily by iodine and cation orbitals, while the conduction band minimum (CBM) is originated exclusively by the cation orbitals, in accordance with the localized nature of the states which can be seen in the band structure. The particular composition of the VBM has its explanation in the highly conjugated π orbitals present in the cations, the shallow levels of which are partially mixed with iodine p-orbitals.

As it could be anticipated, the electronic band gap of 0.71 eV, obtained at the PBE-SOC level of theory is largely underestimated, so, a more accurate estimate was obtained through G_0W_0 calculations, by the use of the electron wavefunctions obtained by PBE-SOC calculations: in fact, this method led to a renormalization of the electronic band gap, to 2.01 eV, a value which is higher than the measured optical band gap of 1.6 eV, highlighting the presence of large exciton effects in **AEPyPb$_2$I$_6$**.

In order to determine the nature of the optical excitations at low energies, that is, close in energy to band-to-band transitions, a simulation of the optical spectrum of **AEPyPb$_2$I$_6$** was carried out, by solving the Bethe Salpeter equation (BSE) on top of the quasi-particle states calculated at the G_0W_0 level; the results of the simulation are displayed in **Figure 3.24**.

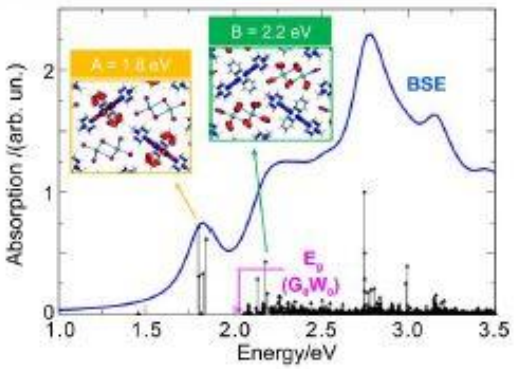

Figure 3.24 Simulated optical spectrum of **AEPyPb$_2$I$_6$** obtained by solving the Bethe Salpeter equation on top of the G_0W_0, with the most intense exciton peaks at lower energies highlighted in yellow and green.

The simulated absorption spectrum features several exciton peaks of various nature; the calculated optical excitations possessing the lowest energy show very small oscillator strengths and are placed at 1.46 eV, that is, at a lower energy than the fundamental gap of the material (2.01 eV), denoting large exciton binding energies of 0.55 eV. These dark excitons are associated to $\pi \rightarrow \pi^*$ transitions, taking place mainly between the HOMO and

LUMO orbitals of the organic cations, and are slightly below the optical gap obtained experimentally, which is of 1.6 eV, though they quantitatively reproduce the optical feature observed in PL emission at ~1.4 eV.

The first intense exciton peak, indicated with A in **Figure 3.24**, is found to be, from calculations, 0.21 eV lower in energy than the fundamental gap, and it is in agreement with the optical feature measured by absorption spectroscopy at about 1.8 eV. Similarly to the lowest energy exciton, also this excitation is mainly originated by HOMO-LUMO singlet transitions in the cation (see inset in **Figure 3.24**). Notably, the dark exciton solution at 1.4 eV is observed only with a full relativistic treatment of the BSE problem, that is, not restricting the spin multiplicity, while, without SOC, the bright exciton at 1.8 eV is the lowest energy excitation. This fact, together with the low oscillator strength, resulting from calculations, highlights that the dark exciton has a mixed singlet-triplet character, and it can be likely activated in emission.

The optical spectrum at higher energies than 2 eV is mainly characterized by the convolution of exciton peaks arising from charge transfer processes between the I p-orbitals and the LUMO of the cation, a typical feature of viologen compounds, as already pointed out; the inset in **Figure 3.24** shows the Kohn-Sham orbitals which give a major contribution to such transition in the intense peak found by calculations at 2.2 eV and indicated as B.

The optical features of **$AEPyPb_2I_6$** can be interpreted on the basis of the computational analysis performed: in the absorption spectrum, $\pi \rightarrow \pi^*$ transitions of the organic cation are mainly responsible for the low energy region of the spectrum, while at higher energies (above 2 eV) an overlapping of these transitions with charge transfer processes between the inorganic and the organic components occurs. The energy value of 1.6 eV of the optical gap, determined by absorption spectroscopy, is intermediate in energy between the first dark exciton, at 1.46 eV, and the first bright exciton, predicted at 1.80 eV, demonstrating in general a good agreement between experiments and theory.

It is important to note, however, that a direct comparison between calculations and experiments is difficult, for the presence of temperature effects, modulating the optical gap of the material, through the activation of the cation vibrational modes inside the 1D channels of **$AEPyPb_2I_6$**. Anyway, the bright emission measured experimentally at about 1.4 eV is consistent with the activation of the dark exciton calculated at 1.46 eV and can

be ascribed to the fluorescence of the cation after the relaxation of the photo-generated electron-hole pair into the LUMO and HOMO orbitals.

3.3 Conclusions

An extended viologen featuring an anthracene core, namely **AEPyI$_2$**, has been synthesized and utilized for the preparation of a novel lead halide hybrid perovskite, of formula **AEPyPb$_2$I$_6$**: this material has been thoroughly characterized by a vast range of techniques, including powder X-ray and electron diffraction, TG-DTA, UV-visible diffuse reflectance, photoluminescence, FTIR and Raman spectroscopy, to probe its chemical and structural properties; moreover, theoretical calculations have been performed, in order to correlate its emission properties with its electronic band structure. **AEPyPb$_2$I$_6$** is remarkably stable to environmental conditions, due to the absence of acidic protons in the organic cation, possesses a good thermal stability, up to 300° C, and shows an optical band gap value of 1.6 eV, besides an intense photoluminescence, centered at 1.43 eV. The crystal structure of this perovskite was determined by 3D ED, on nanometric single crystals, and presents an arrangement of metal halide double chains surrounding the organic cations (a 1D perovskite structure).
The interesting emissive properties, arising from the interaction of the large and conjugated organic cation with the inorganic framework, combined with an easy synthesis and the absence of reactivity towards air and moisture, make **AEPyPb$_2$I$_6$** an extremely promising material for optoelectronic applications.

3.4 Experimental section

All the reagents were purchased from Merck and used as received unless otherwise stated. Dry solvents were distilled according to standard procedures: tetrahydrofuran was distilled over Na/benzophenone, triethylamine and diisopropylamine were distilled over KOH and dichloromethane was distilled over P_2O_5.

Reactions and chromatographic separations were monitored by thin layer chromatography (TLC) on 0.25 mm silica gel plates (Merck Kieselgel 60 F_{254}) and revealed under a UV lamp (λ = 254 nm). Column chromatography was carried out on silica gel Merck-Kieselgel 60 (0.063-0.20 mm, 70-230 mesh) as a stationary phase.

^{1}H and ^{13}C NMR spectra were recorded on a Bruker Avance 400 spectrometer (400 MHz) using 5 mm tubes and chloroform-*d* ($CDCl_3$), methanol-d_4 (CD_3OD) and dimethyl sulfoxide-d_6 (DMSO-d_6) as internal standards.

ESI-MS analysis was performed on a Thermo Scientific-TSQ QUANTUM ACCESS triple quadrupole spectrometer.

Fluorescence spectra were measured on a Cary Eclipse (Varian) spectrofluorimeter, using SUPRASIL quartz cells (10x10 mm).

The C, H, N, and S elemental analysis was performed with an EA 1110 CHNS-O elemental analyzer.

3.4.1 Synthetic procedures

Synthesis of 4-((trimethylsilyl)ethynyl)pyridine (1a): In a flame-dried Schlenk tube, under argon atmosphere, 60 mL of a degassed and anhydrous 3:1 THF/*i*-Pr_2NH mixture and 7.3 g (37.5 mmol) of 4-bromopyridine hydrochloride (previously washed with a 2 N aqueous NaOH solution and extracted three times with CH_2Cl_2) are introduced. Then, 400 mg (0.57 mmol) of $Pd(PPh_3)_2Cl_2$, 195 mg (1.0 mmol) of CuI and 7.0 mL (50.5 mmol) of trimethylsilylacetylene are added and the mixture is heated to 80° C and stirred for 3 days. After that, the reaction is cooled to room temperature, the resulting mixture is filtered to remove the solids and washed with CH_2Cl_2, then extracted with H_2O (100 mL), dried over anhydrous Na_2SO_4 and concentrated under vacuum. The crude product is purified with column chromatography (9:1 petroleum ether/ethyl acetate) to yield 3.9 g of pure **1a** as a yellow-brownish oil (60%). ^{1}H-NMR ($CDCl_3$, 400 MHz) δ 8.55 (m, 2H), 7.30 (m, 2H) 0.25 (s, 9H); ^{13}C-NMR ($CDCl_3$, 100 MHz) δ 149.65, 131.26, 125.84, 101.94, 100.00, -0.32.

Synthesis of 4-ethynylpyridine (1b): In a round-bottom flask, 3.9 g (22.3 mmol) of **1a** are dissolved in 55 mL of methanol, under argon atmosphere, and 3.48 g (25.2 mmol) of K_2CO_3 are added. The resulting suspension is stirred overnight at room temperature,

protected from light, then 50 mL of H_2O are added, and the solution is extracted with CH_2Cl_2 (3x50 mL). The combined organic phases are dried over anhydrous Na_2SO_4 and concentrated under vacuum at room temperature, to yield 2.9 g of crude **1b** as a light-sensitive and volatile white solid, which is used without further purification. ^{1}H-NMR ($CDCl_3$, 400 MHz) δ 8.59 (m, 2H), 7.34 (m, 2H) 3.29 (s, 1H); ^{13}C-NMR ($CDCl_3$, 100 MHz) δ 149.81, 130.33, 126.09, 81.87, 80.94.

Synthesis of 9,10-bis(pyridin-4-ylethynyl)anthracene (1c): In a flame-dried Schlenk tube, under argon atmosphere, 25 mL of a degassed 1:1 toluene/Et_3N mixture are introduced, together with 400 mg (1.2 mmol) of 9,10-dibromoanthracene, 27 mg (0.14 mmol) of CuI, 27 mg (0.12 mmol) of $Pd(OAc)_2$ and 54 mg (0.21 mmol) of PPh_3, and the mixture is stirred at room temperature; after that, 375 mg (3.6 mmol) of 4-ethynylpyridine **1b** are added and the temperature is increased to 80° C. The reaction mixture is stirred for 3 days, then it is cooled to room temperature and filtered to remove the solids. The solvent is then evaporated under reduced pressure and the crude is separated by column chromatography (7:3 petroleum ether/ethyl acetate → ethyl acetate) to yield 158 mg of compound **1c** (35%) along with 54 mg of byproduct **1d** (15%). ^{1}H-NMR ($CDCl_3$, 400 MHz) δ 8.73 (m, 4H), 8.65 (m, 4H), 7.70 (m, 4H), 7.63 (m, 4H); ^{13}C-NMR ($CDCl_3$, 100 MHz) δ 149.92, 132.58, 131.67, 127.47, 127.02, 125.53, 118.51, 99.68, 90.74.

Synthesis of 4,4'-(anthracene-9,10-diylbis(ethyne-2,1-diyl))bis(1-methyl-1-pyridinium) iodide ($AEPyI_2$): In a flame-dried Schlenk tube, 146 mg (0.38 mmol) of **1c** are dissolved in anhydrous CH_2Cl_2 and 1.3 mL (20.9 mmol) of CH_3I are added under argon atmosphere. The mixture is stirred at 40° C overnight, then it is cooled to room temperature and filtered under vacuum; the collected solid is washed with portions of CH_2Cl_2 and dried for 1 hour under suction, to yield 184 mg (0.28 mmol) of **$AEPyI_2$** as a dark red solid (72%). ^{1}H-NMR (DMSO-d_6, 400 MHz) δ 9.13 (m, 4H), 8.84 (m, 4H), 8.67 (m, 4H), 7.92 (m, 4H), 4.38 (s, 6H); ^{13}C-NMR (DMSO-d_6, 100 MHz) δ 146.14, 138.12, 132.59, 129.76, 129.61, 127.46, 118.19, 99.39, 97.61, 48.36. MS (+ESI): *m/z* 205.5 [M^{2+}]. MS (-ESI): *m/z* 126.9 [I^-]. UV-Vis (H_2O, l=10mm, c=4.2x 10^{-5}): λ=274 nm, ε=110000 $M^{-1}cm^{-1}$; λ=511 nm, ε=10000 $M^{-1}cm^{-1}$.

Synthesis of $AEPyPb_2I_6$: In a glass vial, 38 mg (0.0572 mmol) of **$AEPyI_2$** are dissolved in 3 mL of H_2O; in another vial, 53 mg (0.115 mmol) of PbI_2 and 26 mg (0.173 mmol) of NaI are dissolved in 9 mL of acetone. The first solution, containing the organic salt, is then slowly added, dropwise, to the second: instantaneously, a dark red-brown solid starts to form. After addition is complete, the mixture is vigorously shaken, then it is left stand alone for 24 hours, during which the precipitate changes color to dark violet-black. After that, the dark solid is filtered under vacuum and washed with several portions of a 3:1 acetone/water mixture, then it is dried for 2 hours under suction, to yield 91 mg of crude product. The solid is subsequently dissolved in 75 mL of DMF, the dark red solution is filtered over a 0.45 μm PTFE syringe filter and exposed to CH_2Cl_2 vapors for 72 hours in a closed container. After vacuum filtration, the product is washed with multiple portions of CH_2Cl_2 and allowed to dry for 1 hour under suction, to yield 60 mg of pure **$AEPyPb_2I_6$** as black crystals (66%). Samples for structure determination by electron diffraction were grown by exposing saturated solutions of **$AEPyPb_2I_6$** in DMF in silanized glass vials, covered by aluminum foil with a single small hole in it, to CH_2Cl_2 vapors, in a closed vessel, for 1 week at 22° C. Elemental analysis, calculated: C 22.70%, H 1.40%, N 1.77%; found C 23.99% H 1.45%, N 1.87%.

3.4.2 Characterization techniques

Thermogravimetry-Differential Thermal Analysis (TG-DTA): TG-DTA analysis was performed with a Netzsch STA 409 PC Luxx simultaneous thermal analyzer. The analysis was performed under flowing Ar atmosphere (85 cm^3/min at STP, purity ≥ 99.9995%) in an alumina crucible and a thermal scan rate of 10 K/min in the 30−500° C temperature range was used.

UV-Visible spectroscopy: The UV-Vis spectrum in diffuse reflectance mode was acquired with a Shimadzu (Japan) UV2600 UV-vis spectrophotometer, equipped with an ISR-2600 Plus integrating sphere, by using $BaSO_4$ as a reference. The same instrument was also used for the measure of UV-visible spectra in solution.

FT-IR spectroscopy: A Bruker Alpha FT-IR spectrophotometer was used in ATR mode using the ATR Platinum Diamond 1 accessory for the acquisition of the IR spectrum in the 400-4000 cm^{-1} wavenumber range, with resolution: 4 cm^{-1}.

Raman spectroscopy: For Raman measurements, the excitation laser was provided by a single frequency Nd:YVO_4 lasers (DPSS series by Lasos) emitting at 532 nm. The Raman signal was spectrally dispersed by an ACTON SP750 monochromator with focal length of 750 mm and equipped with a 300 grooves/mm grating. The signal was detected by a back-illuminated N_2-cooled Si CCD camera (100BRX by Princeton Instruments). The laser light was filtered out by a very sharp longpass Razor edge filter (Semrock). The spectral resolution was 2.8 cm^{-1}. A 100x objective with NA = 0.9 was employed to excite and collect the light, in a backscattering configuration.

PL spectroscopy: PL measurements were taken in the same experimental configuration used for Raman measurements. In this case, the sample was excited through a 20x objective with NA = 0.4 and the signal was spectrally dispersed by a Princeton Isoplane160 monochromator with focal length of 200 mm and equipped with a 150 grooves/mm grating. The signal was detected by a back-illuminated N_2-cooled Si CCD camera (100BRX by Princeton Instruments) or by an InGaAs linear array (PyLoN-IR by Princeton Instruments). To have reliable information of the PL lineshape and intensity, the system response was duly taken into account. The system response was measured by using a blackbody source and by comparing the measured spectrum with the blackbody nominal one.

Structure Determination: High-angle annular dark-field scanning transmission electron microscopy (HAADF-STEM) imaging and three-dimensional electron diffraction (3D ED) were carried out with a transmission electron microscope (TEM) Zeiss Libra 120 equipped with a LaB_6 cathode (120 kV). 3D ED was performed by keeping the TEM in STEM mode after defocusing the beam in order to have a parallel illumination on the sample, as described by Lanza et al..[189] ED patterns were collected in Köhler parallel illumination with a beam size of about 150 nm in diameter, obtained using a 5 μm C2 condenser aperture. Data were recorded by a single-electron ASI MEDIPIX detector.[190]

The powdered sample was gently crushed and loaded directly on a carbon-coated Cu TEM grid without any solvent or sonication. 3D ED acquisitions were performed when rotating the sample around the TEM goniometer axis in steps of 1°, with a total tilt range up to 110°. After each tilt, a diffraction pattern was acquired, and the crystal position was tracked by STEM imaging. The exposure time per frame was 1 s. The camera length was 180 mm, allowing resolution in real space up to 0.7 Å. The extremely low-dose illumination allowed data to be acquired at room temperature without evidence of any sample amorphization. In order to proper integrate every reflection over the excitation error, during the experiment, the beam was precessed around the optical axis by an angle of 1°.[191] Precession was obtained using a Nanomegas Digistar P1000 device.

3D ED data were analysed using the *PETS2.0* software package.[192] Structure determination of inorganic clusters was achieved by standard direct methods (SDM), while organic ligand molecule was added by simulated annealing (SA), as implemented in the *SIR2014* software package.[193] The resolution limit was set at 0.9 Å. Data were treated with a fully kinematical approximation, assuming that I_{hkl} was proportional to $|F_{hkl}|^2$. The model determined by SA was refined with the least-squares procedures embedded in the *SHELXL* software package.[194] Geometrical restraints and constraints were added stepwise to check the consistency of the model. All hydrogen atoms were generated in geometrically idealized positions.

Powder X-ray diffraction: High quality PXRD patterns were collected on a Malvern Panalytical X'Pert Pro MPD, operating in Bragg-Brentano geometry and equipped with an ultrafast RTMS X'Celerator detector. The diffraction data were acquired in the 2θ ranges of 3.5-8.5° and 8.5-90° using Cu Ka radiation Ni-filtered ($\lambda_{k\alpha 1}$ = 1.54056 Å, $\lambda_{k\alpha 2}$ = 1.54439 Å). A beam knife was used in the range of 3.5-8.5°, in order to suppress the main beam diffuse scattering.

Thin film X-ray diffraction measurement was performed using the thin film module equipped with a graphite monochromator of the same Malvern Panalytical X'Pert Pro MPD diffractometer. The scan was performed in parallel beam mode using a fixed incidence angle set at 1.5° in order to minimize substrate contribution.

The unit cell and structure parameters were refined with *Jana2006*.[195] The background was described by manually picked fixed points. The analyzed data collections were

merged by scaling the baseline of the 8.5-90° range with respect to the 3.5-8.5° baseline. Profile parameters were first obtained by Le Bail fitting and kept fixed in the Rietveld. Unfortunately, the PXRD patterns suffer from limited diffraction resolution and severe peak overlap preventing a free Rietveld refinement.

The refinement on **$AEPyPb_2I_6$** was performed starting from the atomic coordinates obtained by the single-crystal 3D ED model. The organic fraction of the structural model (**$AEPy^{2+}$**) was refined as semi-rigid bodies, able to rotate around their single bonds while the aromatic rings were considered as rigid bodies.

Computational details: DFT calculations were carried out in the primitive cell of **$AEPyPb_2I_6$** by using the Quantum Espresso (QE) software package[196] and by fixing cell parameters to the experimental values. The equilibrium positions of ions in the cell were found by performing a geometry relaxation using the PBE functional and including DFT-D3 dispersion corrections.[197] Calculations were performed by using scalar relativistic norm-conserving pseudopotentials (I 5s, 5p; N and C 2s, 2p; H 1s; and Pb 6s, 6p, 5d shells explicitly included) with a cutoff on the wavefunctions of 60 Ry and a 8x1x1 k-point grid in the Brillouin zone (BZ). Phonon calculations were carried out at the experimental cell parameters. The ground state geometry and charge density were calculated by using the same computational setup described above but without including dispersion corrections. Phonon frequencies at the Γ point of the BZ and the relative IR spectrum were calculated at the PBE level by using DFPT41, as implemented in the QE package.

The electronic structure of the perovskite was calculated at the PBE-D3 relaxed geometry by using the PBE functional and by including spin orbit coupling (SOC) with the use of the full relativistic version of the pseudopotentials. The optical spectrum was calculated by solving the BS equation on top of G_0W_0 calculation, for an accurate estimate of the electronic features and exciton properties of the perovskite, by using the Yambo code.[198] G_0W_0 calculations were carried out in the plasmon-pole approximation by using the wavefunctions provided by PBE-SOC calculations. A cutoff of 40 Ry (4 Ry) for the exchange (correlation) part of the self-energy were used, by including a total of 1000 bands (VB contains 444 electrons) in the calculation of the dielectric matrix and correlation energy. BSE calculations were performed on top of QP corrected eigenvalues

by using a cutoff of 40 Ry (4 Ry) on the exchange (screening) parts and by including 30 occupied and 30 unoccupied bands. A 10x1x1 grid of k-points in the BZ was used.

Chapter 4: Synthesis and characterization of $AEPy_3Bi_4I_{18}$

4.1 Synthesis of a bismuth-analogue of $AEPyPb_2I_6$

In the previous chapter, the synthesis and characterization of the hybrid lead iodide perovskite **$AEPyPb_2I_6$** has been discussed, both on the structural and on the physico-chemical point of view; the material has been found to possess very interesting optoelectronic properties, originating from the unique combination of its highly conjugated large organic cation with the metal halide double chains framework.

We turned to lead as the metal of choice to prepare our perovskite since this is the most exploited element for such materials (as already explained in detail in Chapter 1), so this allowed us to make a parallel with attributes found in similar hybrid haloplumbates possessing organic cations with viologen-related structure. As regards the intense PL emission verified for **$AEPyPb_2I_6$**, it is possible to compare it, for example, with the behavior of another 1D lead halide perovskite featuring a large organic cation, that is, phenyl viologen lead iodide (see Chapter 2, section **2.1.2**): PL studies carried out on this material revealed it is not active in the as-prepared form, but it starts to emit after a short laser treatment and a thermal annealing turns it into a highly photoluminescent material, as a consequence of a rearrangement in the structure induced by high temperature;[199] by contrast, **$AEPyPb_2I_6$** does not need any treatment, since it shows high emission efficiency in its native form, as seen in Chapter 3, section **3.2.4**.

So, the extremely promising results obtained with the use of **$AEPy^{2+}$** as an organic component in hybrid lead perovskite, encouraged us in the synthesis of an analogue characterized by the presence of a different metal, in order to compare the structural and optoelectronic properties; the choice of the element fell on bismuth, for the reasons already discussed in Chapter 1, section **1.4**.

The synthesis of the bismuth perovskite was accomplished in a similar way to the lead one: the organic salt **$AEPyI_2$** (the synthesis of which has been shown in Chapter 3, section **3.1.1**) was dissolved in H_2O to obtain a saturated solution, while BiI_3 was dissolved in acetone (volume was chosen so that total solvent volume after mixing of the two solutions had a ratio H_2O:acetone equal to 1:3); since BiI_3, differently from PbI_2, has a good solubility in acetone, NaI was not needed.

$$3\mathbf{AEPyI_2} + 4BiI_3 \rightarrow \mathbf{AEPy_3Bi_4I_{18}} \quad (22)$$

An instantaneous precipitate formation, upon addition of the aqueous solution to the one containing the bismuth salt, took place; subsequent filtration and drying of the solid yielded the desired perovskite as a black powder, which was subsequently crystallized by the vapor diffusion method, using DMF as a solvent and CH_2Cl_2 as an antisolvent, affording **$AEPy_3Bi_4I_{18}$** as black crystals, as shown in **Figure 4.1**

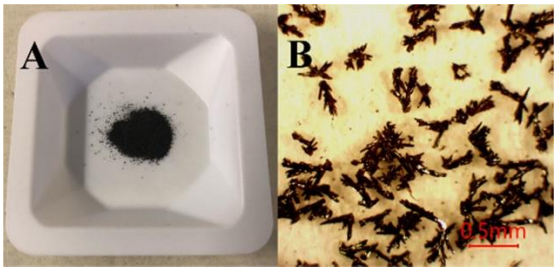

Figure 4.1 $AEPy_3Bi_4I_{18}$ powder (left) and some crystals observed under an optical microscope, with 4x magnification, in reflected light (right).

The purity of the material was ascertained by ^{1}H-NMR spectroscopy, in *d*$_6$-DMSO, and ESI-MS, in methanol, (in positive ion mode) in an analogous way to the lead perovskite; the mass spectrum of **$AEPy_3Bi_4I_{18}$** is reported in **Figure 4.2**. Moreover, elemental analysis was employed to determine its stoichiometry.

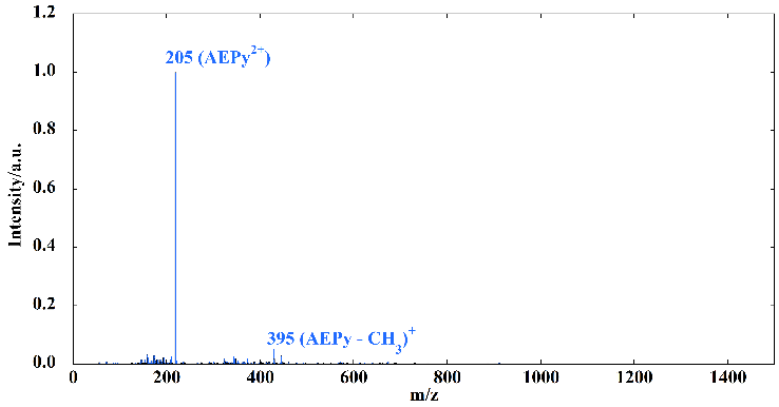

Figure 4.2 ESI mass spectrum (positive ions) of **$AEPy_3Bi_4I_{18}$**.

4.2 $AEPy_3Bi_4I_{18}$ characterization

As seen for **$AEPyPb_2I_6$**, also the bismuth perovskite **$AEPy_3Bi_4I_{18}$** was extensively characterized, with several different techniques, in order to elucidate its chemical, structural and photophysical properties and evaluate the possibility of benefiting of this lead-free hybrid material for optoelectronic applications.

4.2.1 Environmental and thermal stability

First of all, it was of fundamental importance to assess the stability of **$AEPy_3Bi_4I_{18}$** in environmental conditions; as in the case of **$AEPyPb_2I_6$**, an ^{1}H-NMR spectrum, shown in **Figure 4.3**, performed on a sample, stored in ambient air at room temperature for several months after its preparation, and compared to that of the perovskite directly after its synthesis, confirmed the identity of the organic cation, and the absence of its degradation products, thus showing it is inert to atmospheric oxygen when embedded in the inorganic framework.

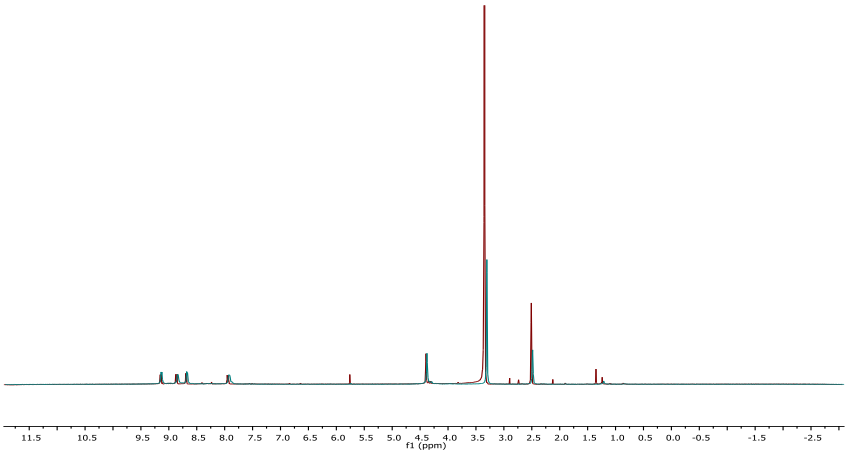

Figure 4.3 ^{1}H-NMR spectrum of a freshly prepared **$AEPy_3Bi_4I_{18}$** sample (blue line), compared to a sample stored for some months in ambient air at room temperature (red line).

In addition, perovskite reactivity towards water at room temperature was tested by immersing some perovskite crystals in distilled water for one hour and then acquiring a powder X-ray diffraction pattern after their recovery by filtration and drying. As it is demonstrated in **Figure 4.4**, peaks in the pattern do not show significant changes between the as-prepared sample and the perovskite after treatment, proving **$AEPy_3Bi_4I_{18}$** is stable

in water; a slight difference in peak intensities can be attributed to preferred orientation effects, due to the configuration of the diffractometer (Bragg-Brentano geometry).

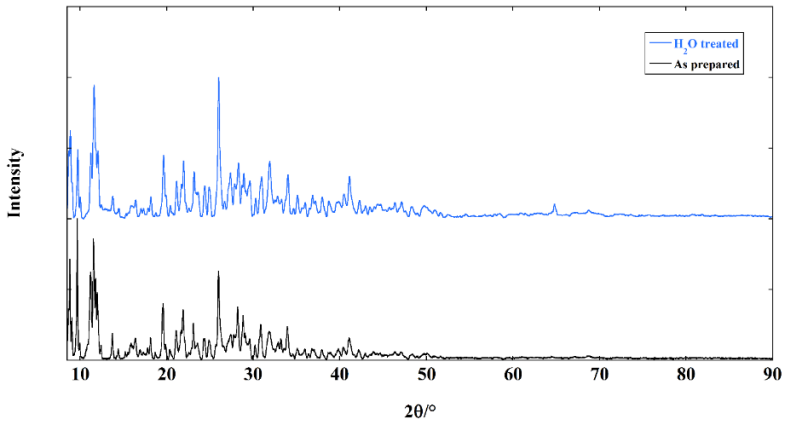

Figure 4.4 XRD powder patterns of the as-prepared (black line) and water treated (blue line) **$AEPy_3Bi_4I_{18}$** samples, showing perovskite water tolerance.

The lack of reactivity towards water, on the other hand, could be easily inferred from the quaternary nature of the organic cation, as already seen for **$AEPyPb_2I_6$**, and from the preparation of the material by precipitation from an aqueous solution.

In addition, **$AEPy_3Bi_4I_{18}$** thermal stability was investigated by means of TG-DTA measurement, in argon atmosphere, and the result of the analysis is reported in **Figure 4.5**; as it can be seen from the thermogravimetric curve, the material does not undergo any modification up to a temperature around 300° C, after which a gradual weight loss can be observed, corresponding to an endothermic event in the DTA curve, followed by another one at higher temperature, about 400° C, accompanied by a change in the TG slope.

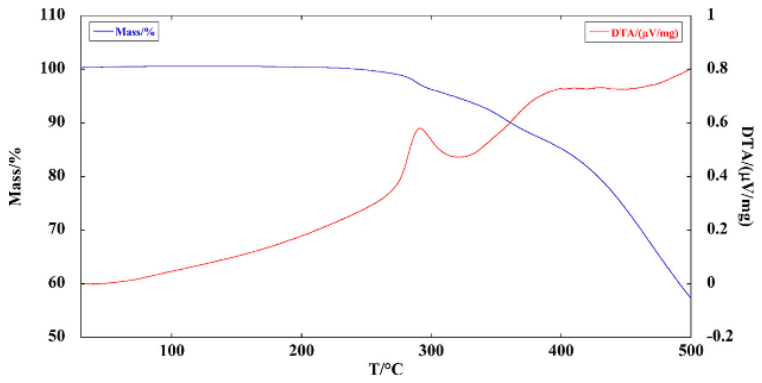

Figure 4.5 TG-DTA curve of **$AEPy_3Bi_4I_{18}$**.

Given that the organic salt starts to decompose at a temperature a little above 300° C, and the structural determination (which will be discussed in detail in the next section) highlighted the presence of crystallization solvent (DMF) molecules in the crystal lattice, the first decrease in sample mass can be attributed to the loss of solvent and degradation of the organic component, while the second thermal event, characterized by a faster mass loss, can be identified as the evaporation of BiI_3, which has a vapor pressure of 1 atm at 316° C.[200]

4.2.2 Crystal structure determination

In contrast to the impossibility of obtaining single crystals suitable for structure determination of **AEPyPb$_2$I$_6$** by X-ray diffraction (see section **3.2.2**), the growth of **AEPy$_3$Bi$_4$I$_{18}$** crystals was surprisingly straightforward. An examination of the crystalline powder obtained by vapor diffusion, as explained previously, through an optical microscope, with polarized transmitted light and crossed polarizers, revealed that it was composed by dark elongated platelet-shaped single crystals; their dimensions were in the hundreds of μm range, as shown in **Figure 4.6**, making them large enough for single crystal X-ray diffraction.

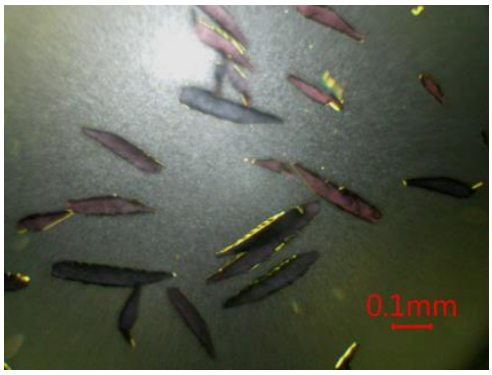

Figure 4.6 Optical microscopic image of **AEPy$_3$Bi$_4$I$_{18}$** single crystals taken with 10x magnification with polarized light and crossed polarizers; the crystals appear of homogeneous color or homogeneously dark.

In order to succeed in structure determination, especially as regards the large organic cation, a synchrotron radiation source was preferred, given the presence of a high number of heavy atoms in the structure; single-crystal X-ray diffraction measurements were then performed at the XRD1 beamline of the Elettra synchrotron radiation facility in Trieste

(Italy)[201,202] and structure analysis was performed by Dr. Alberto Cassetta and his research group.

$AEPy_3Bi_4I_{18}$ crystallizes in the monoclinic system, in the P21/n space group, and features a structure which can be defined as a 0D perovskite (see Chapter 1, section **1.5.2**) and is typical of halobismuthates such as methylammonium bismuth iodide $(CH_3NH_3)_3Bi_2I_9$ and cesium bismuth iodide $Cs_3Bi_2I_9$, containing isolated Bi_2I_9 clusters formed by two BiI_6^{3-} octahedra sharing one face;[203,204] a projection of the unit cell along the *a* axis is reported in **Figure 4.7.**

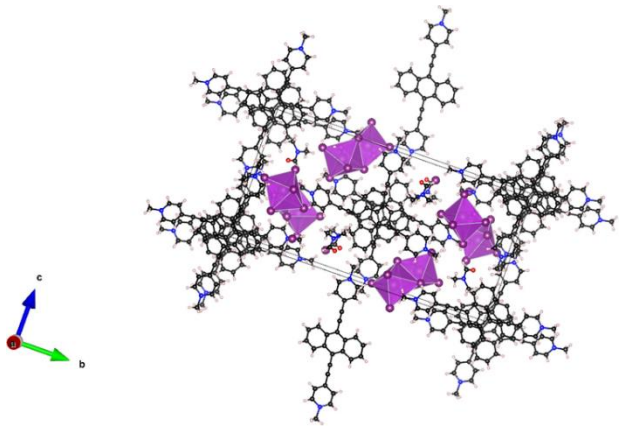

Figure 4.7 Unit cell of **$AEPy_3Bi_4I_{18}$** seen along the *a* crystallographic axis; black: C, blue: N, white: H, purple: I; Bi atoms are the spherical shadows inside the face-sharing octahedra.

The formation of metal halide isolated clusters, rather than extended motifs, such as the double chains of Pb_2I_6 octahedra seen in **$AEPyPb_2I_6$**, offers an explanation to the different tendency to the formation of large crystals between the two materials, as already pointed out when previously discussing lead perovskite structure: it is likely that the absence of polymeric chains formed by the inorganic components makes **$AEPy_3Bi_4I_{18}$** crystal growth easier.

The asymmetric unit of the bismuth iodide perovskite crystallographic structure, shown in **Figure 4.8a**, is constituted by a $Bi_2I_9^{3-}$ anion, a disordered DMF molecule and one full plus half of **$AEPy^{2+}$** cations, while the second half of the incomplete **$AEPy^{2+}$** is generated by a center of symmetry situated on the geometric center of the anthracene moiety. The presence of solvent molecules in the crystal lattice can explain the slight discrepancy between the experimental and calculated elemental analysis, especially as regards

nitrogen content. The two cations in the asymmetric units are rotated by 90° with respect to each other, as represented in **Figure 4.8b**.

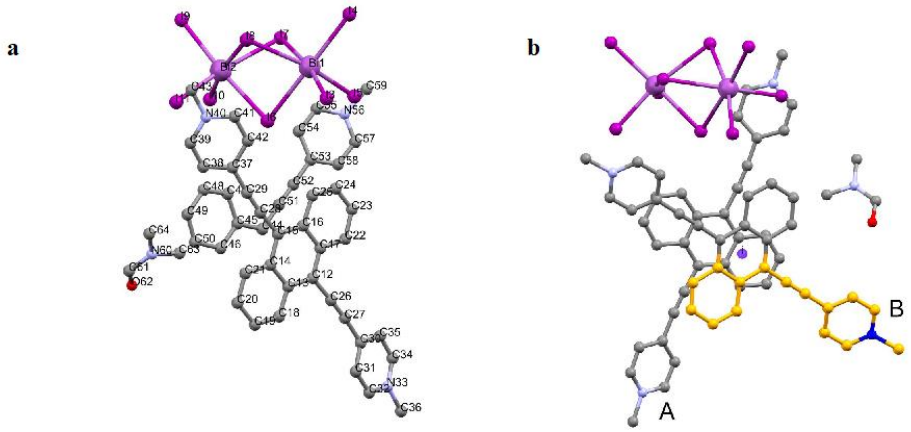

Figure 4.8 Stick-and-ball representations of the asymmetric unit of **$AEPy_3Bi_4I_{18}$** crystallographic structure, with indicated in **a)** the labelling scheme of the atoms and in **b)** the symmetry-generated second half of the **$AEPy^{2+}$** cation (in yellow) and the inversion center (the light-purple sphere), lying on the anthracene moiety, generating it; grey: C, blue: N, dark purple: I, lighter purple: Bi.

$AEPy^{2+}$ cations generate a much more complex interaction network in the crystal, compared to what had been encountered in **$AEPyPb_2I_6$** structure, where the organic cations were simply piled up along the *a* axis, with the anthracene moieties forming parallel planes. In **$AEPy_3Bi_4I_{18}$**, the organic cations are indeed stacked together along the *a* direction, following an ABA repeating motif, where A indicates the **$AEPy^{2+}$** cation entirely contained in the asymmetric unit, while B refers to the **$AEPy^{2+}$** half cation observed in the asymmetric unit (see **Figure 4.8b**). The ABA units develop along the *a* direction, according to the (ABA)(ABA) repeating scheme shown in **Figure 4.9a**: A and B molecules are stacked in an almost parallel way, owing to the presence of π-π interaction between the aromatic systems; indeed, the mean planes passing through the anthracene subunits of cations A and B form an angle of 3.3° with a distance of 3.50 Å between the planes.

Moreover, a further and different network of **$AEPy^{2+}$** cations is put in place between an AB unit interacting through C−H···π bonds with a neighboring organic cation, and precisely between the methyl group bound to nitrogen atom and the pyridinium aromatic

system of another **AEPy**$^{2+}$ cation; this additional interaction network is demonstrated in **Figure 4.9b**.

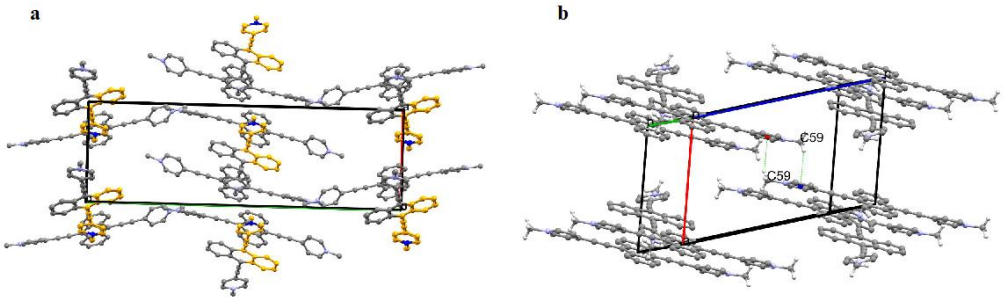

Figure 4.9 Stick-and ball representation of **a)** the (ABA)(ABA) network seen along the ***c*** axis, with **AEPy**$^{2+}$ of type B half colored in yellow ($Bi_2I_9^{3-}$ and disordered DMF molecules are not shown) and **b)** the (AB)··· **AEPy**$^{2+}$ interaction network, with centroids of the pyridinium ions represented as spheres colored in blue and red on neighboring cations ($Bi_2I_9^{3-}$ and disordered DMF molecules, as well as **AEPy**$^{2+}$ belonging to the (ABA)(ABA) network are not shown).

As regards the inorganic components of the crystal, the face-sharing BiI_6^{3-} octahedra in the $Bi_2I_9^{3-}$ clusters, shown in **Figure 4.10**, are highly distorted, similarly to the case of $(CH_3NH_3)_3Bi_2I_9$: in fact, they feature different interatomic distances and bond angles, thus suggesting a stereochemically active 6s lone pair, similarly to Pb-based hybrid metal halide perovskites.[205]

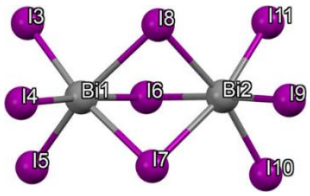

Figure 4.10 A $Bi_2I_9^{3-}$ cluster.

This distortion is in agreement with those observed in other 0D bismuth iodide perovskites:[206,207] the Bi−I distances in Bi1−I3, Bi1−I4, Bi1−I5, Bi2−I9, Bi2−I10, and Bi2−I11 are sensibly shorter than the distances Bi1−I6, Bi1−I7, Bi1−I8, Bi2−I6, Bi2−I7, and Bi2−I8.

The bond angles also display the same behavior observed in other perovskites, with the I−Bi−I angles formed with I atoms shared by the two octahedra showing values below

90°, while values over 90° are observed for I−Bi−I angles formed with no shared I atoms. All the Bi−I interatomic distances and I−Bi−I angles are reported in **Table 4.1**, while in **Table 4.2** crystal structure details are summarized.

The following hydrogen bonds are established between the $Bi_2I_9^{3-}$ anions and the organic cations: I3-H36C (3.07 Å), I7-H36A (2.99 Å), I3-H57 (3.08 Å), I10-H31 (3.10 Å), and I5-H23 (3.15 Å); these interactions suggest a donor-acceptor semiconductor behavior for **AEPy$_3$Bi$_4$I$_{18}$**, with charge transfer processes from $Bi_2I_9^{3-}$ anions to the cations, as it is typical of viologens.

Finally, the bond lengths in the cation are consistent with those expected on the basis of its chemical nature: in particular, the C−C distances in the acetylenic linkers (1.19 Å) between the pyridinic rings and the anthracene unit are in agreement with the expected value for a triple bond (1.189 Å).

Bond distances (Å)		Bond angles (°)	
Bi2—I6	3.1545 (9)	I6—Bi2—I8	84.40 (2)
Bi2—I8	3.2230 (10)	I6—Bi2—I7	81.46 (2)
Bi2—I10	2.9907 (9)	I8—Bi2—I7	79.50 (3)
Bi2—I11	2.9277 (12)	I11—Bi2—I10	98.73 (3)
Bi2—I7	3.2954 (12)	I11—Bi2—I9	94.85 (4)
Bi2—I9	2.9705 (10)	I9—Bi2—I10	91.89 (3)
Bi1—I6	3.1606 (9)	I6—Bi1—I8	82.27 (2)
Bi1—I8	3.3485 (9)	I7—Bi1—I6	83.58 (3)
Bi1—I7	3.1572 (10)	I7—Bi1—I8	79.64 (3)
Bi1—I4	3.0068 (10)	I4—Bi1—I3	94.56 (4)
Bi1—I3	3.0141 (11)	I5—Bi1—I4	91.87 (3)
Bi1—I5	2.8631 (9)	I5—Bi1—I3	92.73 (3)

Table 4.1 Bi−I interatomic distances and I−Bi−I angles

Crystal structure	
Chemical formula	Bi_2 I_9, C_{30} H_{21} N_2, C_{15} H_{11} N, C_3 H_7 N O
M_r	2247.89
Crystal system, space group	Monoclinic, P21/n
Temperature (K)	298
a, *b*, *c* (Å)	10.958 (2), 33.008 (7), 17.070 (3)
α, *β*, *γ* (°)	90, 106.42 (3), 90
V (Å^3)	5922 (2)
Z	4
Radiation type	Synchrotron
μ (mm^{-1})	10.26
Crystal size (mm)	0.07 × 0.05 × 0.05
Data collection	
Diffractometer	Synchrotron
Absorption correction	Empirical (using intensity measurements)
SADABS	
N° of measured, independent and observed [$I > 2.0\sigma(I)$] reflections	69652, 10842, 10412
R_{int}	0.043
θ_{min} = 1.2°	θ_{max} = 24.9°
Refinement	
$R[F^2 > 2\sigma(F^2)]$, $wR(F^2)$, S	0.042, 0.112, 1.12
N° of reflections	10842
N° of parameters	551
H-atom treatment	H-site location: inferred from neighboring sites
$\Delta\rho_{max}$, $\Delta\rho_{min}$ (e Å^{-3})	1.98, −1.41

Table 4.2 Crystal structure data of **$AEPy_3Bi_4I_{18}$**

In **Figure 4.11**, the calculated diffraction pattern from the solved crystal structure for **$AEPy_3Bi_4I_{18}$** is shown, together with the experimental one; in addition, the five most intense reflections have been indexed. As it can be seen, the agreement between the observed powder diffraction pattern and the structure obtained by the single-crystal data is excellent and it has been also confirmed by the Le Bail fit (R_p = 0.338, R_{wp} = 0.696, R_{Bragg} = 3.383), shown in **Figure 4.12**.

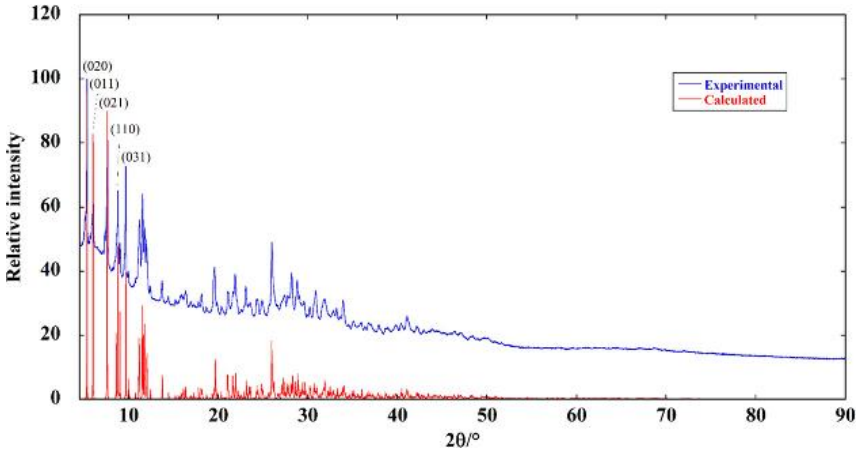

Figure 4.11 Experimental (blue line) and calculated (red line) powder diffraction patterns of **$AEPy_3Bi_4I_{18}$**.

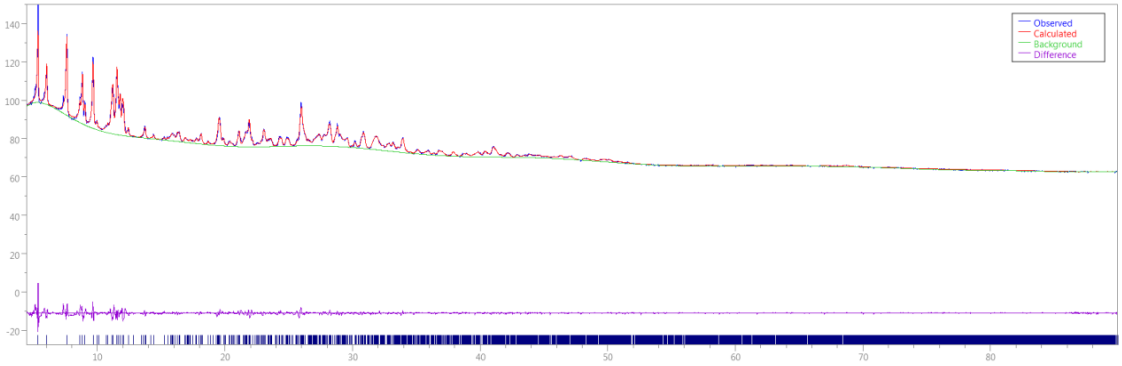

Figure 4.12 Le Bail fit of the experimental powder diffraction pattern of **$AEPy_3Bi_4I_{18}$** with the structure obtained by single crystal data.

4.2.3 FTIR and Raman spectroscopy

Similarly to **$AEPyPb_2I_6$**, also for the bismuth perovskite FTIR and Raman spectroscopy experiments were carried out, in order to elucidate its vibrational properties: the results obtained are consistent between the two techniques, showing an overall good agreement between the different spectral features observed, as it can be seen in **Figure 4.13**.

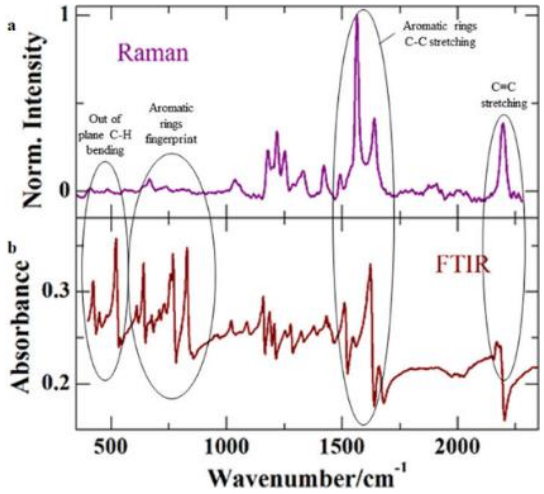

Figure 4.13 a) Raman and **b)** FTIR spectrum of **$AEPy_3Bi_4I_{18}$** in the 400-2350 cm^{-1} range.

As already underlined for **$AEPyPb_2I_6$**, the vibrational bands are due only to the organic cation, since Bi and I are heavy atoms and consequently the vibrations associated to the inorganic sublattice cannot be seen in the FTIR instrument's spectral range (400-4000 cm^{-1}). The peak at 2165 cm^{-1} can be assigned to the C-C stretching of the two triple bonds present in the molecule, while the intense FTIR features in the range 900-650 cm^{-1} are typical of aromatic structures, as in our case (the same features are observed also in the Raman spectrum, yet less pronounced). The intense peaks around 1600 cm^{-1} can be assigned to the C−C stretching in aromatic rings. The 400-650 cm^{-1} region shows peaks that can be attributed to the out-of-plane C−H bending vibrations. Both Raman and FTIR measurements were taken also in the range from 2350 to 4000 cm^{-1}, but no peaks were observed.

Notably, as for **$AEPyPb_2I_6$**, Raman spectrum measurement, as well as photoluminescence studies, which will be described in the next section, were performed by Dr. Elena Blundo, and Prof. Antonio Polimeni's research group, at the Department of Physics, Sapienza University of Rome.

4.2.4 UV-visible absorption and photoluminescence spectroscopy

As seen for its lead counterpart, also the optical properties of **$AEPy_3Bi_4I_{18}$** were investigated both by diffuse reflectance UV-visible spectroscopy and by photoluminescence (PL) spectroscopy. In **Figure 4.14a**, the pseudoabsorbance spectrum, determined by UV-visible measurements, is shown, while the corresponding Tauc plot,

evaluated by assuming a direct optical transition, in analogy with **$AEPyPb_2I_6$**, can be seen in **Figure 4.14b**. The optical band gap energy E_g, estimated from the Tauc plot, corresponds to 1.64 eV, a very similar value to that found for the lead perovskite **$AEPyPb_2I_6$**, for which a band gap energy of 1.6 eV had been determined, as seen in Chapter 3, section **3.2.4**.

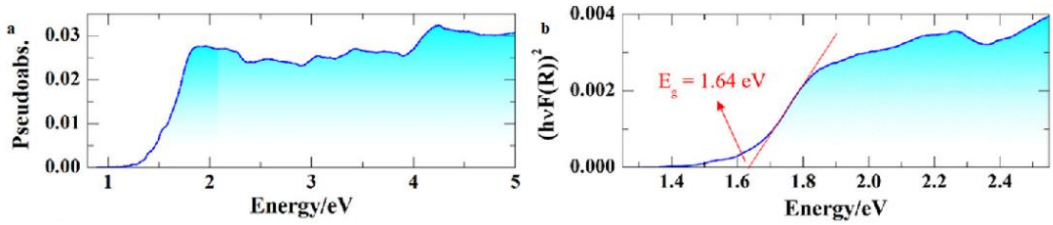

Figure 4.14 a) UV-visible pseudoabsorbance spectrum of **$AEPy_3Bi_4I_{18}$** and **b)** Tauc plot, calculated assuming a direct optical transition.

In order to test the optical efficiency of **$AEPy_3Bi_4I_{18}$** and its potential use for optoelectronic applications, PL measurements at room temperature were performed: the sample was excited by a 532 nm laser via a 100x objective, and the signal was collected through the same objective, spectrally dispersed through a 150 grooves/nm monochromator and detected with a Si-CCD. The photoluminescence spectrum of the perovskite, for an excitation power of 2 μW, is represented by the green curve in **Figure 4.15**.

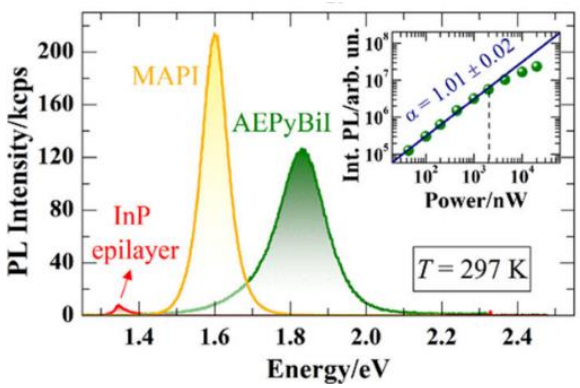

Figure 4.15 PL spectrum of **$AEPy_3Bi_4I_{18}$** (green curve), compared to those of an InP epilayer (red curve) and of MAPI (yellow curve); the insect shows the integrated intensity of the PL signal of **$AEPy_3Bi_4I_{18}$** as a function of the excitation power and the data, fitted up to the dashed line, corresponding to 2 μW, demonstrate a linear behavior.

The PL band is centered at about 1.83 eV, and thus about 0.2 eV above the band gap estimated by the Tauc plot. The efficiency of the emission of **$AEPy_3Bi_4I_{18}$**, was evaluated by comparing its PL spectrum with that of a high-quality 3-micron-thick (100) InP epilayer, grown by metal-organic chemical vapor deposition at a temperature of 650 °C (as already seen when discussing PL measurements on **$AEPyPb_2I_6$**), since this is a highly emissive material and its emission properties are well established; measurements on the InP epilayer standard were performed exactly under the same experimental conditions of the perovskite. **$AEPy_3Bi_4I_{18}$** possesses indeed a much more intense emission, with the integrated intensity exceeding that of the InP signal by a factor of about 35.

The PL signal of **$AEPy_3Bi_4I_{18}$** was also compared to that of methylammonium lead iodide (MAPI), as done for **$AEPyPb_2I_6$**; the PL spectrum of MAPI is also shown in **Figure 4.15**, represented by the yellow curve, and a comparison between the two spectra demonstrates that the two perovskites are characterized by a comparable PL efficiency: in fact, the integrated intensity of MAPI is larger than that of **$AEPy_3Bi_4I_{18}$** of a factor of 1.1. Noteworthy, this is an even better result than that evidenced for **$AEPyPb_2I_6$** (see Chapter 3, section **3.2.4**), since, in that case, the integrated intensity of MAPI emission exceeded that of the material under study by a factor of about 3.1.

Moreover, **$AEPy_3Bi_4I_{18}$** PL signal is characterized by a very good homogeneity, as it is demonstrated by the spectra in **Figure 4.16**, showing PL intensity for seven different points of **$AEPy_3Bi_4I_{18}$** powder, obtained by using an excitation power of 1 μW, with peak maxima varying in the range 1.826-1.837 eV and only moderate differences in intensity.

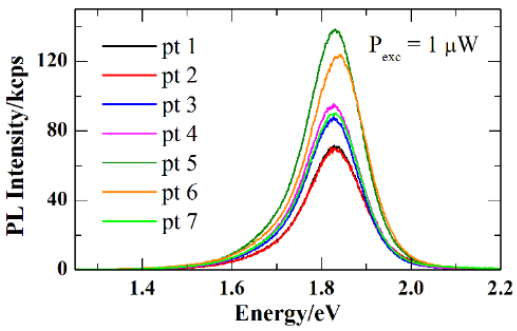

Figure 4.16 PL spectra of **$AEPy_3Bi_4I_{18}$** acquired on seven different points of the powder; the spectrum showed in the previous figure corresponds to that taken on point 1.

Perovskite robustness upon photoexcitation was also tested, as already seen for **AEPyPb$_2$I$_6$**: indeed, further PL measurements were performed, by varying the excitation power from 40 nW to 20 μW. In this range, the lineshape of the PL signal does not show significant variation, as **Figure 4.17** shows.

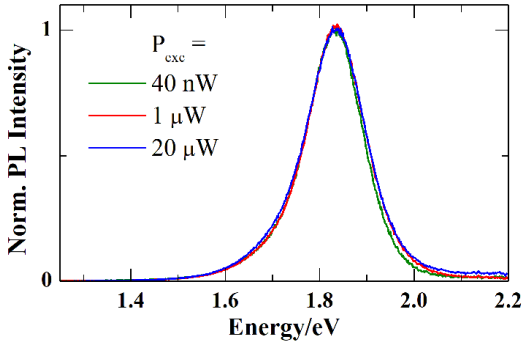

Figure 4.17 Normalized PL spectra of **AEPy$_3$Bi$_4$I$_{18}$** acquired by exciting the sample with three different excitation powers, varying over about three orders of magnitudes.

Considering the integrated area of the PL signal, it increases in a linear way up to about 2 μW, as it can be seen in the inset of **Figure 4.15**. The data were fitted through the equation $I = A \cdot P\alpha$, where I indicates the integrated intensity, P is the excitation power, A is a scaling constant, and α is the exponent, which was found to be equal to 1.01 ± 0.02 by the fit, suggesting a modest density of nonradiative recombination channels. For P > 5 μW, a deviation of the intensity from the linear behavior occurs, suggesting that the sample is starting to degrade.

4.3 Conclusions

A new, lead-free perovskite, namely **AEPy$_3$Bi$_4$I$_{18}$**, has been successfully synthesized, starting from the extended viologen **AEPyI$_2$**, prepared by us, and an extensive characterization of this hybrid material has been carried out. Its crystal structure has been determined by single-crystal X-ray diffraction, using synchrotron source, and **AEPy$_3$Bi$_4$I$_{18}$** turned out to possess a 0D perovskite structure (as frequently verified for bismuth-based perovskites), featuring $Bi_2I_9^{3-}$ inorganic clusters and a quite complex

structural motif, formed by organic cations **$AEPy^{2+}$** with the inclusion of crystallization solvent molecules.

The synthesized material is unreactive in ambient conditions and water-insensitive, besides being thermally stable up to about 300° C, as already observed for its lead counterpart **$AEPyPb_2I_6$**, thanks to the presence of the quaternary bipyridinium cation **$AEPy^{2+}$**.

In addition, **$AEPy_3Bi_4I_{18}$** was characterized by different spectroscopic techniques, including FTIR and Raman spectroscopy, for vibrational features, and diffuse reflectance and photoluminescence spectroscopy, to investigate its optical properties. From UV-visible absorption, by using the Tauc plot, an optical band gap value of 1.64 eV has been determined, a very similar value to the one observed for **$AEPyPb_2I_6$**; moreover, PL studies showed an even more intense emission than that already found for **$AEPyPb_2I_6$** (see Chapter 3), centered at 1.83 eV, and characterized by an integrated intensity ∼35 times that of InP standard in the same experimental conditions, making this lead-free perovskite a very appealing material for optoelectronic applications.

4.4 Experimental section

All the details about the reagents, techniques and instruments used for the synthesis and characterization of the intermediates, as well as the synthetic procedure for the synthesis of **$AEPyI_2$** have been already described in Chapter 3, section **3.4**.

4.4.1 Synthesis of $AEPy_3Bi_4I_{18}$

In a glass vial, 50 mg (0.0753 mmol) of **$AEPyI_2$** is dissolved in 4 mL of distilled H_2O; in another vial, 59 mg (0.100 mmol) of BiI_3 is dissolved in 12 mL of acetone. The first solution, containing the organic salt, is then slowly added, dropwise, to the second; instantaneously, a dark-brown solid starts to precipitate. After the addition is complete, the mixture is vigorously shaken and left undisturbed for 24 h. After that, the dark solid is filtered under suction and washed with several portions of a 3:1 acetone/water mixture. It is then dried for 2 h under suction to yield 89 mg of crude product. The precipitate is

subsequently dissolved in 45 mL of *N*,*N*-dimethylformamide (DMF). The dark red solution is filtered over a 0.45 μm PTFE syringe filter and exposed to CH_2Cl_2 vapors for 72 h in a closed container at room temperature. After vacuum filtration, the product is washed with multiple portions of CH_2Cl_2 and allowed to dry for 1 h under suction to yield 51 mg of pure **AEPy$_3$Bi$_4$I$_{18}$** as black crystals (47%). Single crystals suitable for structure determination by X-ray diffraction were grown by exposing saturated solutions of **AEPy$_3$Bi$_4$I$_{18}$** in DMF in silanized glass vials to CH_2Cl_2 vapors, in a closed vessel, for 72 h at 22 °C. Elemental analysis, calculated: C 24.84%, H 1.53%, N 1.93%; found C 24.94% H 1.65%, N 2.40%.

4.4.2 Characterization techniques

TG-DTA, UV-visible, FTIR, Raman and PL spectroscopy, as well as powder X-ray diffraction were performed under the same experimental condition already described in Chapter 3, section **3.4**. The Le Bail fit of the powder diffraction pattern was performed using the EXPO 2014 software.[208]

Single-Crystal Structure Analysis: X-ray diffraction measurements were performed at the XRD1 beamline of the Elettra synchrotron radiation facility (see section **4.2.2**) at room temperature (293 K). X-ray wavelength was set to 0.7 Å, while a Pilatus 2M (Dectris) detector was used for the diffraction experiments. Unit cell assignment, integration, and data reduction were performed with the XDS program;[209] empirical absorption correction was applied using SADABS software.[210] The structure was solved using SHELXT,[211] while Fourier analysis and refinement were performed by the full matrix least-squares methods based on F^2 implemented in SHELXL[212] through the OLEX2 software.[213] Anisotropic thermal motion refinement have been used for all atoms with full occupancy with hydrogen atoms included at calculated positions with isotropic U factors = 1.2·Ueq (Ueq being the equivalent isotropic thermal factor of the bonded nonhydrogen atom). According to a difference Fourier map, a disordered DMF molecule was located and modeled. The disordered DMF molecule was then refined with full occupancy but keeping both geometry and isotropic thermal parameters restrained.

Chapter 5: Different viologen-derived cations for hybrid perovskites

5.1 Synthesis of different viologen-related structures

In Chapters 3 and 4, the synthesis and characterization of two novel hybrid perovskites containing the extended viologen **AEPy^{2+}** has been described. The two materials, namely **AEPyPb$_2$I$_6$** and **AEPy$_3$Bi$_4$I$_{18}$** have been proved to possess an excellent stability under ambient conditions as well as a remarkable thermal stability; moreover, they feature very interesting optoelectronic properties, in particular a narrow band gap and a very intense photoluminescence, making them ideal candidates for light emission applications.
All these advantageous characteristics stimulated us to extend the scope of our work, through the preparation of several other viologen-like organic cations to be used for the synthesis of lead and bismuth halide hybrid perovskites; their structures, already shown in **Figure 2.3** are reported again here (**Figure 5.1**).

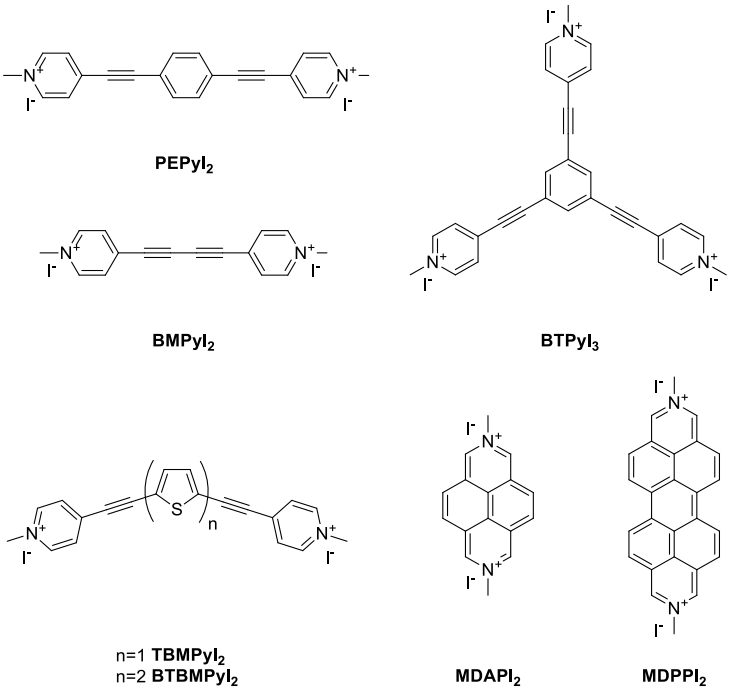

Figure 5.1 Structure of the cations examined in this chapter.

Indeed, some of these structures were already described in the literature, nevertheless their use as organic cations in hybrid perovskites, to the best of our knowledge, has never been reported.

For all of the displayed cations (except in the case of **$BMPyI_2$**, for which only the iodoplumbate has been prepared), the corresponding lead and bismuth perovskites have been synthesized; however, only a preliminary study has been conducted by now on these materials, in order to select the most interesting and suitable among them for optoelectronic applications. In the next sections, then, the synthetic routes followed for their preparation will be illustrated first and, after that, the currently available information on the properties of their iodoplumbate and iodobismuthate derivatives will be examined, highlighting which of these hybrid perovskites deserve most a deeper investigation, in order to find out some useful characteristic.

5.1.1 Synthesis of $BMPyI_2$

First of all, we decided to prepare a bipyridinium dication featuring only two acetylenic spacers between the quaternarized rings, without any central aromatic moiety: its synthesis was extremely easy, since it could be afforded by simple dimerization of 4-ethynylpyridine (the synthesis of which has been already described in Chapter 3, section **3.1.1**), through a Hay coupling,[214] as shown in **Scheme 5.1**, followed by reaction with CH_3I.

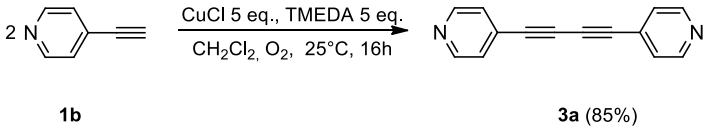

1b **3a** (85%)

Scheme 5.1

The reaction, with CuCl and *N*,*N*,*N*′,*N*′-tetramethylethylenediamine (TMEDA) in ambient air at room temperature, furnished the bipyridine **3a** as a pale brown solid, with a 85%yield, after chromatographic purification; the obtained product was then subjected to substitution reaction on CH_3I, shown in **Scheme 5.2**, with the same procedure already seen for **$AEPyI_2$**, leading to the formation of the corresponding quaternary pyridinium salt **$BMPyI_2$** as a brown solid, isolated by precipitation and filtration, in a moderate yield (53%).

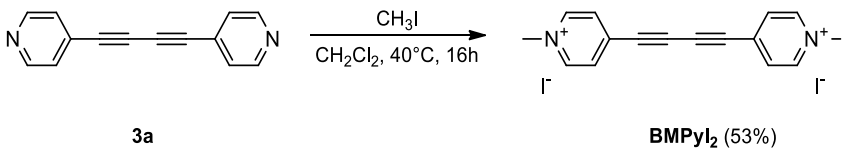

Scheme 5.2

5.1.2 Synthesis of $PEPyI_2$

The next organic salt we planned to synthesize featured a benzene ring as a central aromatic linker between the two triple bonds; its precursor, namely the bipyridine **2a**, could be achieved by two equally simple reactions, both consisting in a palladium-catalyzed Sonogashira cross-coupling, starting from simple building blocks. The first alternative was represented by the reaction between 4-bromopyridine (prepared, here and later in the text, by treating with a 2N NaOH solution the commercial hydrochloride, as seen in Chapter 3, section **3.1.1**) and 1,4-diethynylbenzene,[215] while the second involved the coupling between 1,4-diiodobenzene and 4-ethynylpyridine.[216] We performed the synthesis by using both routes, as reported in **Scheme 5.3**, and obtained the desired compound **2a** with comparable yields (50% and 56%, respectively) after purification by column chromatography, as a white crystalline solid.

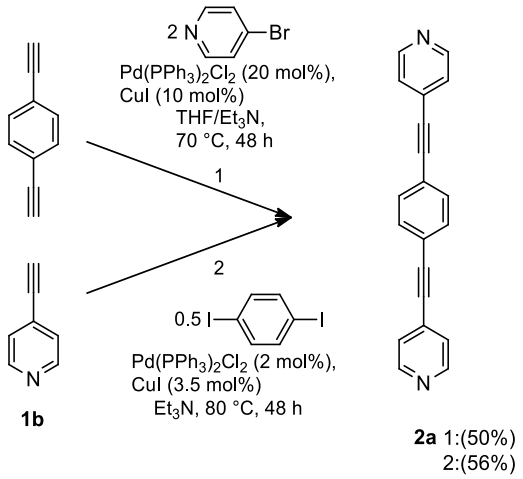

Scheme 5.3

Finally, by the reaction of **2a** with CH_3I, in refluxing CH_2Cl_2, the target quaternary pyridinium salt **$PEPyI_2$** was prepared; the reaction, shown in **Scheme 5.4**, afforded the

pure desired product, precipitated and filtrated from the reaction mixture as a yellow solid, with a yield of 86%.

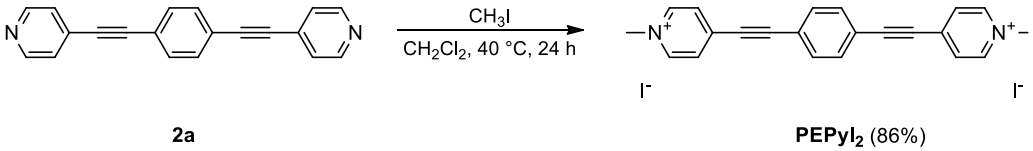

2a **PEPyI$_2$** (86%)

Scheme 5.4

5.1.3 Synthesis of BTPyI$_3$

As seen in Chapter 2, section **2.1.1**, the interest in quaternary pyridinium salts and their properties, in the fields of organic chemistry and material chemistry, is not just limited to compounds presenting two pyridyl moieties connected in *para* position, since it has been demonstrated that an extension of the viologen motif to a different number of pyridinium rings and/or with a different connectivity retains the typical viologen features, such as redox activity.[217,218]

In light of this, we envisioned the preparation of an organic pyridinium salt possessing three charged groups, connected through acetylenic linkers to a central benzene ring; as for the previously illustrated syntheses, also this compound could be prepared by a short and straightforward synthetic route making use of palladium-catalyzed couplings to assemble simple and readily accessible building blocks.

The construction of the target trication started therefore with the Sonogashira reaction between commercially available 1,3,5-tribromobenzene and trimethylsilylacetylene (TMSA), following a reported procedure;[219,220] the coupling reaction, shown in **Scheme 5.5**, afforded the expected product **4a** as a pale yellow solid, with a satisfactory yield of 72% after chromatographic purification.

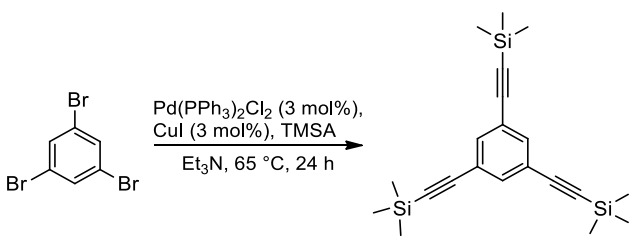

4a (72%)

Scheme 5.5

Following the same procedure, the trimethylsilyl protected triacetylene derivative was subsequently treated, as reported in **Scheme 5.6**, with a basic THF/CH_3OH solution, to furnish 1,3,5-triethynylbenzene **4b** in a very high yield (99%) as a white volatile solid.

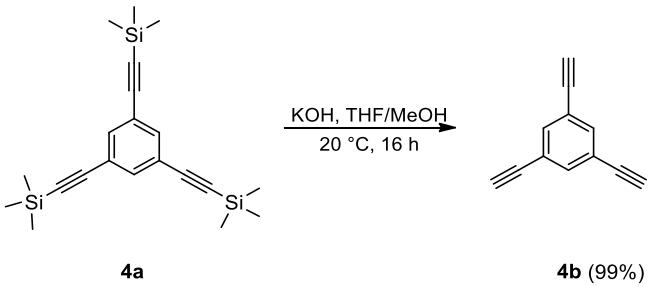

Scheme 5.6

Then, another palladium-catalyzed reaction[221] was carried out, between compound **4b** and 3 equivalents of 4-bromopyridine, as shown in **Scheme 5.7**, leading to the exclusive formation of the tripyridyl product **4c**, obtained as a pale yellow solid, after purification through column chromatography, with a good yield of 68%.

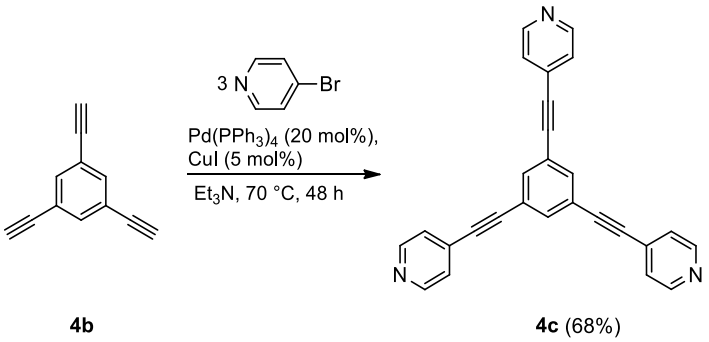

Scheme 5.7

The final reaction of the tripyridyl derivative **4c** with the methylating agent CH_3I, in the usual reaction conditions, as shown in **Scheme 5.8**, afforded the desired quaternary pyridinium salt **BTPyI$_3$** as a pure yellow solid, collected by precipitation from the reaction mixture with a yield of 72%. It should be noted however that, while in the previous cases the reaction reached completion in 24 hours or less, for the preparation of the tricationic compound, a reaction time of 48 hours was needed, since the analysis of the obtained solid by ^{1}H-NMR spectroscopy, for shorter reaction times, highlighted the

presence of byproducts, constituted by mono- and disubstituted species, along with the target **BTPy**$^{3+}$ cation.

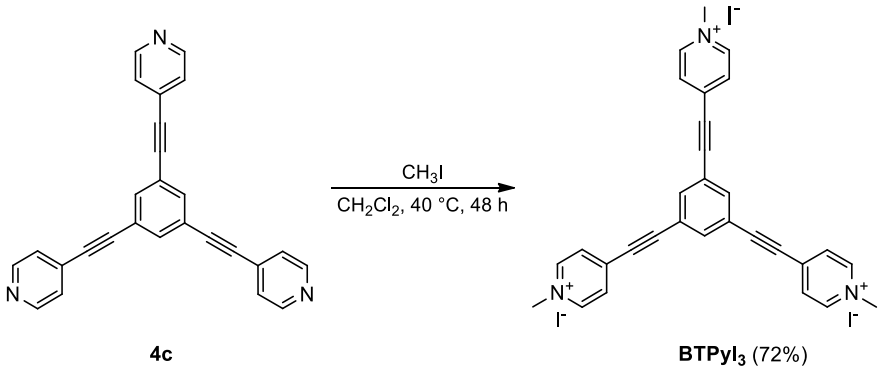

4c **BTPyI$_3$** (72%)

Scheme 5.8

5.1.4 Synthesis of TBMPyI$_2$ and BTBMPyI$_2$

Among the different conjugated structural elements selected for the modification of the viologens that we wanted to introduce in hybrid perovskites, the thiophene motif was an almost obvious choice. Indeed, the insertion of a thiophene derivative in a hybrid haloplumbate is not an unprecedented idea: as it has been highlighted in Chapter 1, section **1.6.1**, the synthesis of the perovskite AEQTPbBr$_4$, where AEQT^{2+} is the doubly protonated 5,5‴-bis(aminoethyl)-2,2′:5′,2″:5″,2‴-quaterthiophene, is among the earliest examples of modulation of the properties of these hybrid materials through an optically active organic component.

The reasons behind the choice of an oligothiophene are quite clear: as it is well known, this class of heterocyclic compounds is one of the most exploited and versatile for organic electronics,[222,223] thanks to their effective electron transport properties, with poly(thiophenes) constituting a prominent example of conducting polymers,[224] and oligomers possessing finely tunable optoelectronic properties and offering practically limitless possibilities for functionalization.[225]

Anyway, we did not need a particularly extended core for the preparation of these thiophene-containing quaternary pyridinium cations, in order to make a comparison with the other synthesized structures featuring different central conjugated units, so we chose to start with the insertion of a single thiophene ring, and then to prepare, in an analogous way, a further extended viologen featuring two of them.

The construction of these two conjugated cations was accomplished, in both cases, starting from the corresponding 2,5-diiododerivatives, since they were both commercially available. As seen for the previously described structures, also in this case the introduction of triple bonds on the central aromatic unit was readily accessible through Sonogashira cross-coupling reactions with trimethylsilylacetylene, and the trimethylsilyl-protected compounds **5a** and **6a** were synthesized according to literature procedures,[226,227] as shown in **Scheme 5.9** and **Scheme 5.10**, respectively.

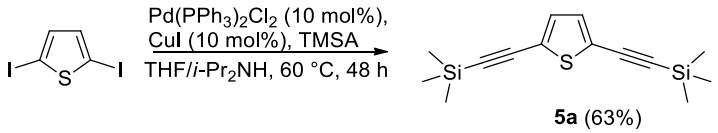

Scheme 5.9

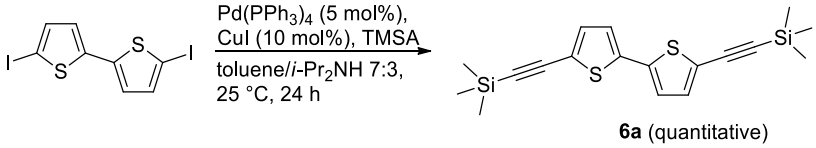

Scheme 5.10

The products **5a** and **6a**, obtained as yellow solids, with a yield of 63% and a quantitative yield, respectively, after chromatographic purification, underwent deprotection in basic conditions, as shown in **Scheme 5.11** and **Scheme 5.12**, again following reported procedures, affording the terminal acetylenes **5b** and **6b**, as a yellow oil and a pale brown solid, in 99% and 89% yields, respectively, after column chromatography.

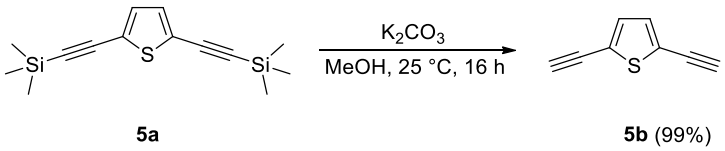

Scheme 5.11

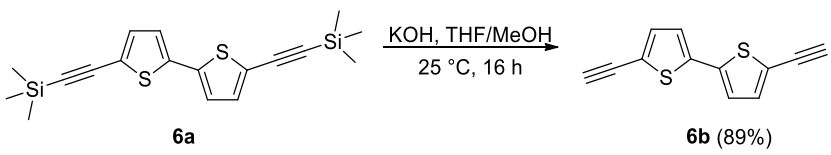

Scheme 5.12

Compounds **5b** and **6b** were then coupled to pyridyl moieties, in an analogous way, according to a modified literature procedure, by a palladium-catalyzed reaction with 4-iodopyridine, leading to the formation of the products **5c** and **6c**, isolated by column chromatography and obtained as yellow solids, with yields of 84% and 68%, respectively; the reaction conditions are shown in **Scheme 5.13.**

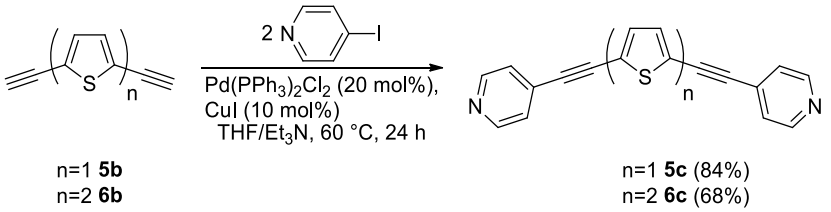

Scheme 5.13

Finally, also the bipyridyl derivatives **5c** and **6c** were subjected to the reaction with CH_3I in refluxing CH_2Cl_2, as shown in **Scheme 5.14**, to afford the corresponding quaternary salts **TBMPyI$_2$** and **BTBMPyI$_2$**, isolated, as usual, by precipitation from the reaction mixture and subsequent filtration, as orange solids, with similar yields of 81% for the first and 83% for the second.

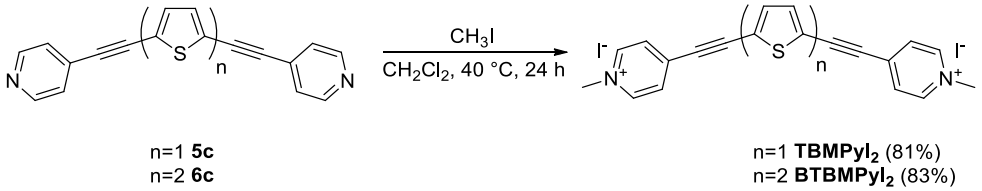

Scheme 5.14

5.1.5 Synthesis of MDAPI$_2$ and MDPPI$_2$

All of the compounds described up to now, with the exception of **BMPyI$_2$**, feature a common structural pattern, that is, an aromatic subunit in the middle, to which methylated pyridinium rings are linked by means of a triple bond; the entire conjugated structure possesses therefore a high flexibility, with many degrees of freedom, given that single and triple bonds allow rotation of the aromatic rings. Indeed, the determination of crystal structures of perovskites **AEPyPb$_2$I$_6$** and **AEPy$_3$Bi$_4$I$_{18}$** has offered an interesting example of this, since the same cation adopts a nearly planar geometry in **AEPy$_3$Bi$_4$I$_{18}$** (see

Chapter 4, section **4.2.2**), while there is an evident deviation from planarity between the two pyridinium rings in **AEPyPb$_2$I$_6$** (see Chapter 3, section **3.2.3**).

We decided then to turn our attention to completely rigid structures, to eliminate this possibility; in particular, two compounds were selected, both of them based on fused-ring aromatic systems, namely a diazapyrene and a diazadibenzoperylene (**MDAPI$_2$** and **MDPPI$_2$**), in which the extended π system, besides ensuring structural rigidity also offered the advantage of making them semiconductor materials by themselves.

A synthetic route in three steps for the preparation of such compounds was found in literature,[228,229,230] so we followed the established pathway to obtain the desired compounds; the reported procedure started from a cyclic dianhydride, commercially available for the two compounds, namely 1,4,5,8-naphthalenetetracarboxylic dianhydride for **MDAPI$_2$** and 3,4,9,10- perylenetetracarboxylic dianhydride for **MDPPI$_2$**.

The dianhydrides were then treated with an aqueous methylamine solution in refluxing conditions, as shown in **Scheme 5.15** and **Scheme 5.16**, followed by isolation of the precipitate, either by filtration (for compound **7a**) or by centrifugation (for compound **8a**), to afford the corresponding cyclic diimides as pure solids, with excellent yield: a pink powder in the case of **7a** (yield 98%) and a red powder in the case of **8a** (quantitative yield).

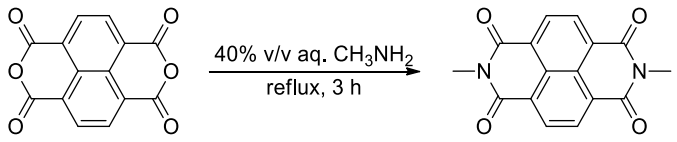

7a (98%)

Scheme 5.15

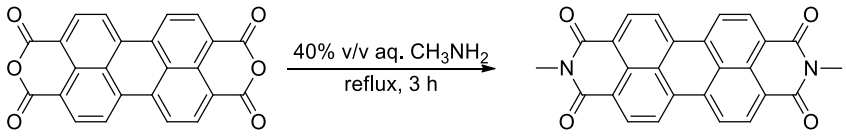

8a (quantitative)

Scheme 5.16

The following synthetic step required the reduction of the two diimides to the corresponding diamines; to prepare them, $LiAlH_4$, in combination with $AlCl_3$ was utilized as a reducing agent, as shown in **Scheme 5.17** and **Scheme 5.18**, leading to the formation of the desired products, which were purified through Soxhlet extraction with $CHCl_3$ and subsequent crystallization from $CHCl_3$/hexane mixture, affording pure **7b** and **8b** with yield, respectively, of 53% and 63%.

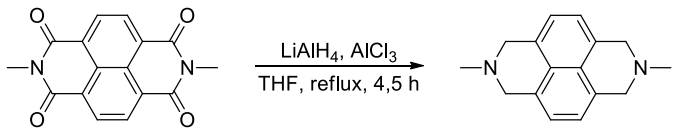

7a **7b** (53%)

Scheme 5.17

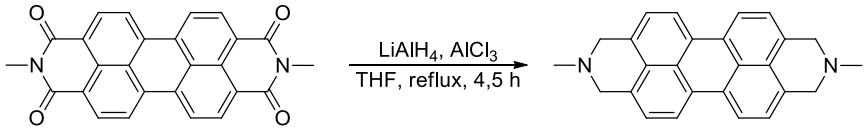

8a **8b** (63%)

Scheme 5.18

As a last step, the reaction, shown in **Scheme 5.19** and **Scheme 5.20**, of the two tertiary amines with DDQ (2,3-dichloro-5,6-dicyano-1,4-benzoquinone) as an oxidizing agent was necessary for the aromatization of the heterocyclic rings. Thus, the reaction, carried out in refluxing acetonitrile for 72 hours, to ensure the complete oxidation of the methylene carbons (since an analysis by ^{1}H-NMR spectroscopy of a portion of the reaction mixture after 24 hours, quenched with acid, indicated the presence of the tertiary ammonium salt arising from the unreacted amine, along with the desired quaternary salt) furnished the target aromatic cations. Addition of HI to the reaction mixture and filtration of the precipitate provided pure compounds **MDAPI$_2$** and **MDPPI$_2$** as an orange and a brown solid, respectively (with yield of 49% and 94%).

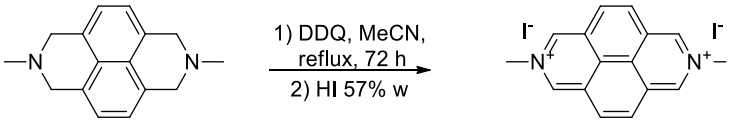

7b **MDAPI$_2$** (49%)

Scheme 5.19

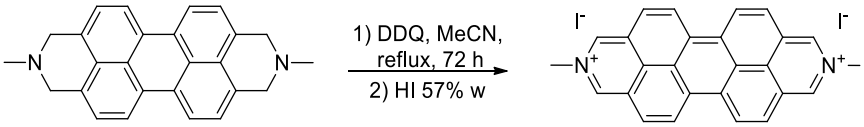

8b **MDPPI$_2$** (94%)

Scheme 5.20

5.2 Characterization of the organic salts and preparation of hybrid perovskites

All the compounds described in the previous section were characterized by ^{1}H-NMR and ^{13}C-NMR, to assess the identity and purity of the organic cationic species; with the exception of **BMPyI$_2$**, which resulted to be quite unstable, starting soon to degrade if not embedded in the hybrid material, all the other salts possess a good stability, at least for moderate periods of times, since their long-term stability has not been tested yet.
Moreover, they are all fairly soluble in H_2O, and water solutions of **PEPyI$_2$**, **TBMPyI$_2$**, **BTBMPyI$_2$**, **MDAPI$_2$** and **MDPPI$_2$** show a quite intense fluorescence, upon irradiation with a UV lamp (**Figure 5.2**).

Figure 5.2 Aqueous solutions containing some of the organic salts, under irradiation with a 365 nm lamp; from left to right, **PEPyI$_2$**, **TBMPyI$_2$**, **BTBMPyI$_2$**, **MDAPI$_2$** and **MDPPI$_2$**.

For these species, UV-visible absorption and fluorescence spectra in water solution have been measured and they are reported in **Figure 5.3** and **Figure 5.4**.

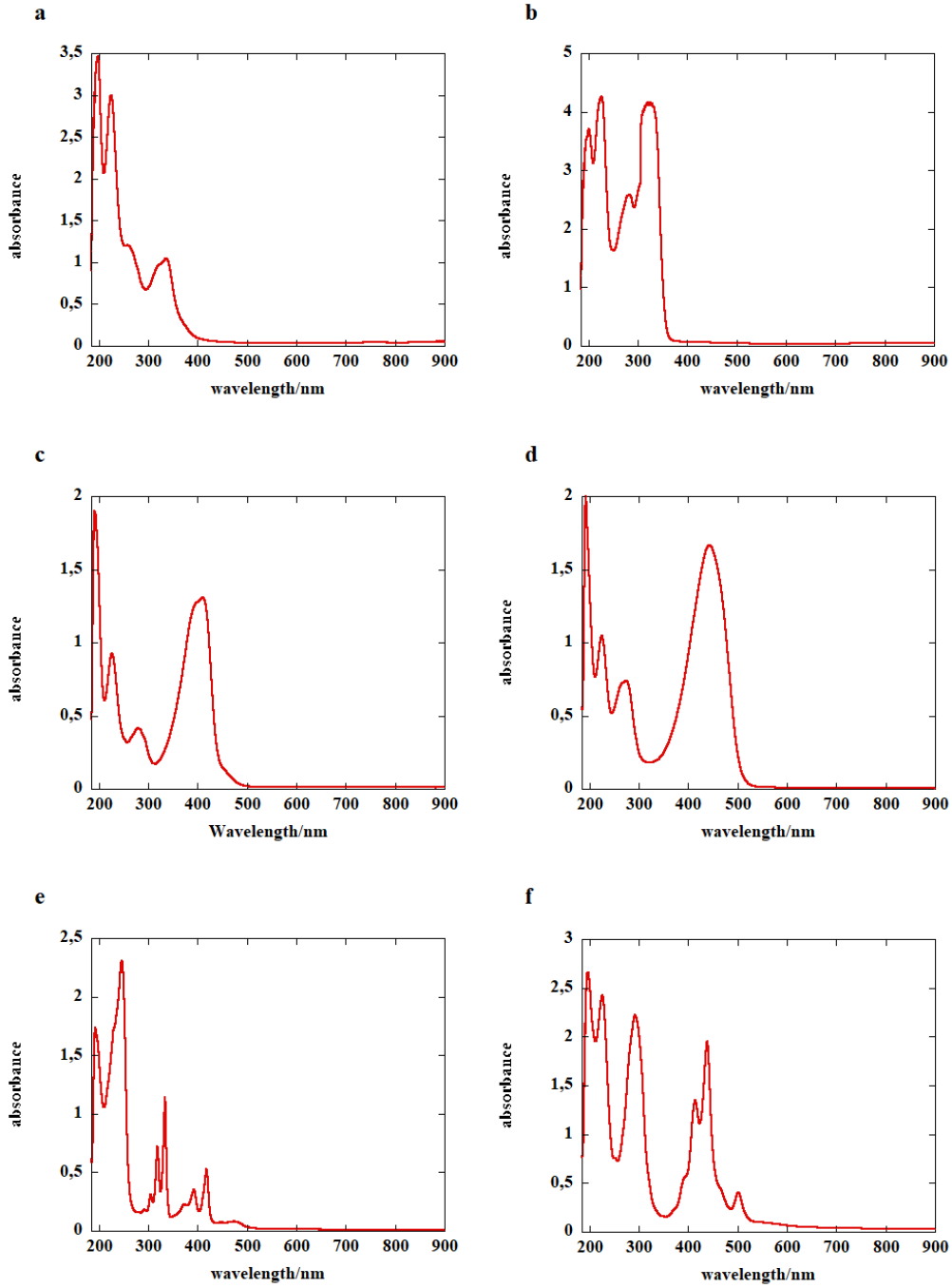

Figure 5.3 UV-visible absorption spectra in H_2O solution of **a) PEPyI$_2$**, c = 7.1x10^{-4} M; **b) BTPyI$_3$**, c = 5.0x10^{-4} M; **c) TBMPyI$_2$**, c = 2.5x10^{-4} M; **d) BTBMPyI$_2$**, c = 2.5x10^{-4}M; **e) MDAPI$_2$**, c = 2.5x10^{-4} M; **f) MDPPI$_2$**, c = 4.6x10^{-4} M.

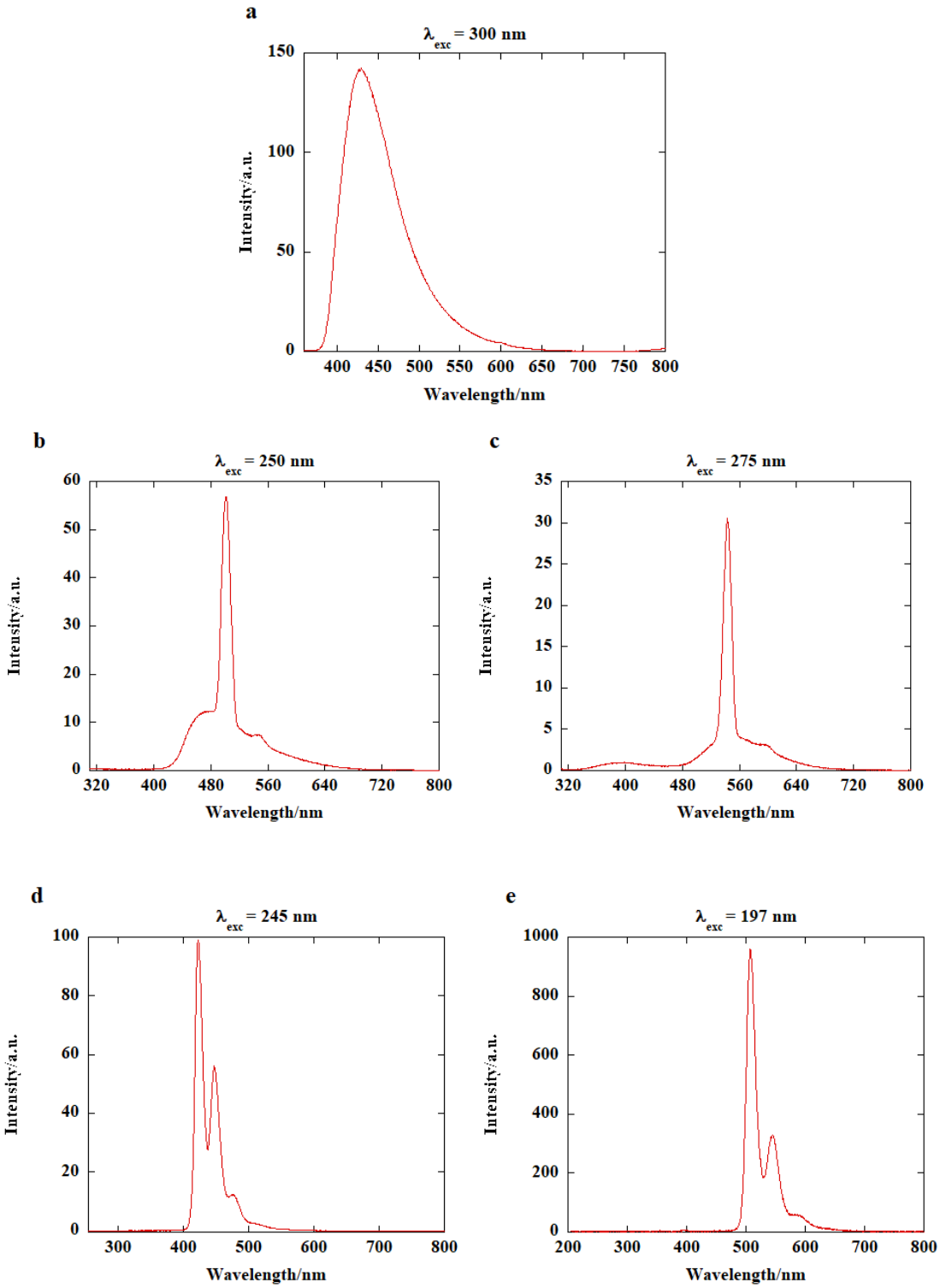

Figure 5.4 Fluorescence spectra in H_2O solution of **a) PEPyI$_2$**, c = 7.1x10^{-4} M; **b) TBMPyI$_2$**, c = 2.5x10^{-4} M; **c) BTBMPyI$_2$**, c = 2.5x10^{-4}M; **d) MDAPI$_2$**, c = 2.5x10^{-4} M; **e) MDPPI$_2$**, c = 4.6x10^{-4} M.

As regards hybrid perovskites, they were all prepared by mixing saturated solutions in DMF of the organic salts with solutions, also in DMF, of PbI_2 or BiI_3; the synthesis from a H_2O/acetone 1:3 mixture, following the same procedure as **$AEPyPb_2I_6$** and **$AEPy_3Bi_4I_{18}$** (see Chapter 3, section **3.2** and Chapter 4, section **4.1**) has been attempted indeed, but the precipitation of the product was incomplete and solid particles were very small, making it difficult to isolate the perovskite by filtration of the solution.
The reactions for the synthesis of lead and bismuth perovskites from an organic salt $CatI_2$ can be summarized by the general equations:

$$CatI_2 + 2PbI_2 \rightarrow CatPb_2I_6 \quad (23)$$

$$3CatI_2 + 4BiI_3 \rightarrow Cat_3Bi_4I_{18} \quad (24)$$

For compound **$BTPyI_3$**, owing to the different stoichiometry, the reactions are

$$\mathbf{BTPyI_3} + 3PbI_2 \rightarrow \mathbf{BTPyPb_3I_9} \quad (25)$$

$$\mathbf{BTPyI_3} + BiI_3 \rightarrow \mathbf{BTPyBiI_6} \quad (26)$$

For all of the prepared perovskites, after mixing of the precursors, the obtained solution in DMF was exposed to CH_2Cl_2 vapors in a closed container, to allow product precipitation, for a variable time, between 72 hours and 2 weeks, followed by filtration of the obtained solid; the details about the synthesis of the single perovskites are reported in the experimental section.
Notably, for most of the compounds, some precipitate started to form immediately, upon mixing of the two solutions (and this was more evident for lead perovskites), so the collected solids turned out to be mostly amorphous. In a few cases however, the solid, isolated by filtration, appeared to be sufficiently crystalline and, for perovskites prepared from the salt **$MDAPI_2$**, it was also possible to perform powder X-ray diffraction on the two synthesized materials; the obtained diffraction pattern are shown in **Figure 5.5** and **Figure 5.6.**

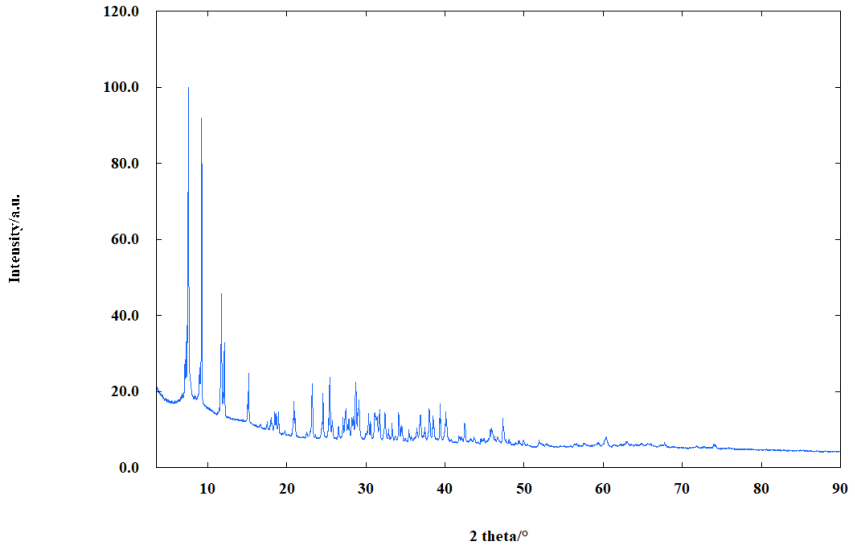

Figure 5.5 Powder X-ray diffraction pattern of lead perovskite from **MDAPI$_2$**.

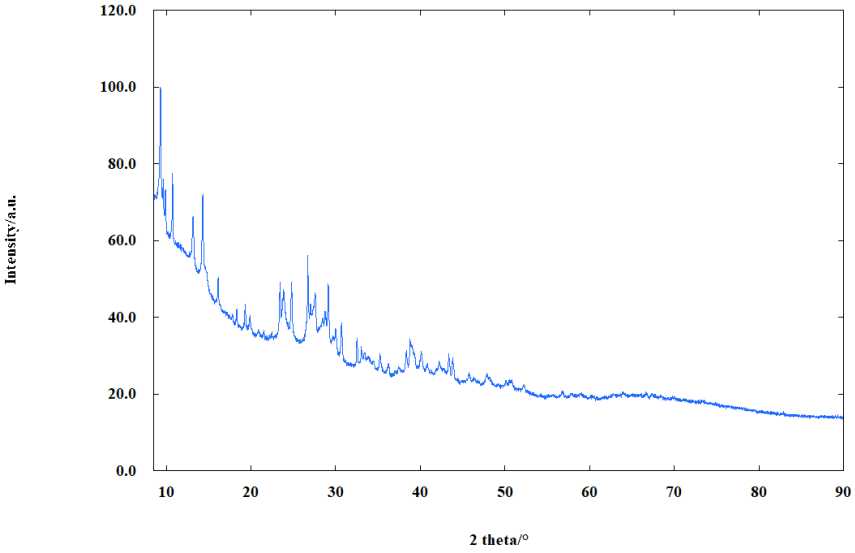

Figure 5.6 Powder X-ray diffraction pattern of bismuth perovskite from **MDAPI$_2$**.

All the perovskites were stored at room temperature in ambient air after their preparation, without appreciable changes in their appearance; however, in order to evaluate their long-term environmental stability, as it has been possible to verify for **AEPyPb$_2$I$_6$** and **AEPy$_3$Bi$_4$I$_{18}$**, more extended periods of time are required.

5.3 Characterization of the perovskites

For some of the hybrid materials, thermal stability has been probed through TG-DTA experiments, carried out in Ar atmosphere; in particular, this has been made for lead perovskite synthesized from **$BMPyI_2$**, for lead and bismuth perovskites obtained from **$PEPyI_2$** and for lead and bismuth perovskites obtained from **$MDAPI_2$**. The results of all thermal analyses are reported in **Figure 5.7**.

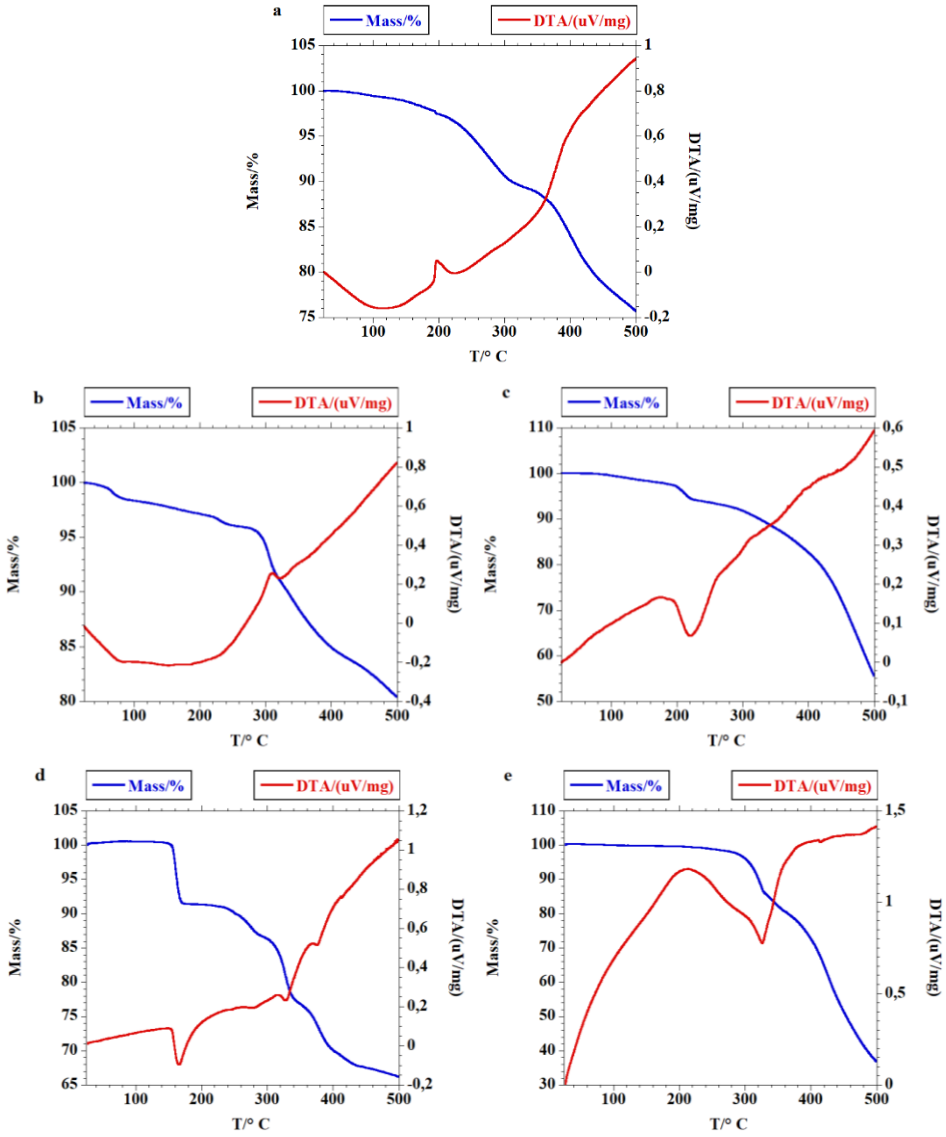

Figure 5.7 Thermogravimetric curves for **a) $BMPyPb_2I_6$; b) $PEPyPb_2I_6$; c) $PEPy_3Bi_4I_{18}$; d) $MDAPPb_2I_6$; e) $MDAP_3Bi_4I_{18}$.**

The analyzed perovskites exhibit all a moderate thermal stability, though not so good as in the case of **$AEPyPb_2I_6$** and **$AEPy_3Bi_4I_{18}$**, since no thermal events are recorded up to about 150° C (a mass loss of about 1.5%, at a temperature below 100° C, for **$PEPyPb_2I_6$** could be due to evaporation of the residual solvent, considering that the analysis was performed on a sample prepared from a H_2O/acetone mixture). An abrupt decrease in mass can be observed for **$MDAPPb_2I_6$** at a temperature of about 160° C, while, for the other materials, relevant changes take place around 200° C or at higher temperatures; notably, in **$MDAP_3Bi_4I_{18}$** some thermal event, which does not involve a decrease in mass, can be observed just above 200° C.

The poorer stability of these materials, compared to the ones with **$AEPy^{2+}$** cation, could be partly explained on the basis of the structure of the organic component, especially for perovskites containing **$BMPy^{2+}$** and **$PEPy^{2+}$** species, possessing a considerably less extended aromatic portion than **$AEPy^{2+}$**. However, the different behavior between materials containing the same organic cation, particularly evident for the two perovskites prepared from **$MDAPI_2$** (in which the cation features a rigid extended aromatic skeleton) clearly indicates that the thermal stability of the iodometallates must be evaluated on the basis of the overall crystal structure resulting from the organic and inorganic components.

All the synthesized materials are intensely colored solids, with tones ranging from orange-red to black, demonstrating a broad absorption in the visible range; the appearance and color of the powders is shown in **Figure 5.8**.

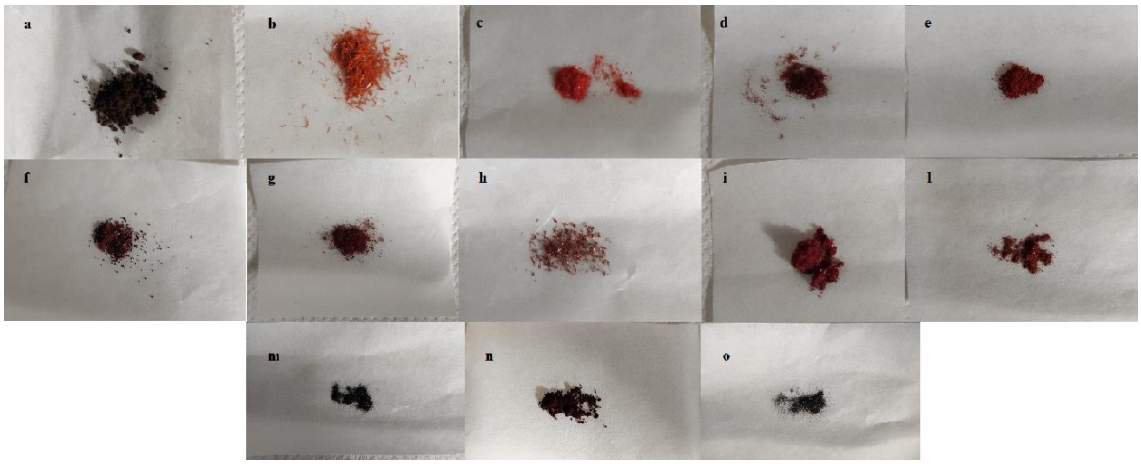

Figure 5.8 Perovskite powders: **a) $BMPyPb_2I_6$**; **b) $PEPyPb_2I_6$**; **c) $PEPy_3Bi_4I_{18}$**; **d) $BTPyPb_3I_9$**; **e) $BTPyBiI_6$**; **f) $TBMPyPb_2I_6$**; **g) $TBMPy_3Bi_4I_{18}$**; **h) $BTBMPyPb_2I_6$**; **i) $BTBMPy_3Bi_4I_{18}$**; **l) $MDAPPb_2I_6$**; **m) $MDAP_3Bi_4I_{18}$**; **n) $MDPPPb_2I_6$**; **o) $MDPP_3Bi_4I_{18}$**.

A preliminary evaluation of the optoelectronic properties, for all the newly synthesized materials, has been performed through diffuse reflectance UV-visible spectroscopy. In the following figures (**Figure 5.9** to **Figure 5.21**), the pseudoabsorbance spectra of the perovskites are reported (on the left), together with their Tauc plots (on the right), for the type of transition which fits best with the experimental value of the absorption edge; in all cases, a direct band gap, either allowed or forbidden, has been assumed.

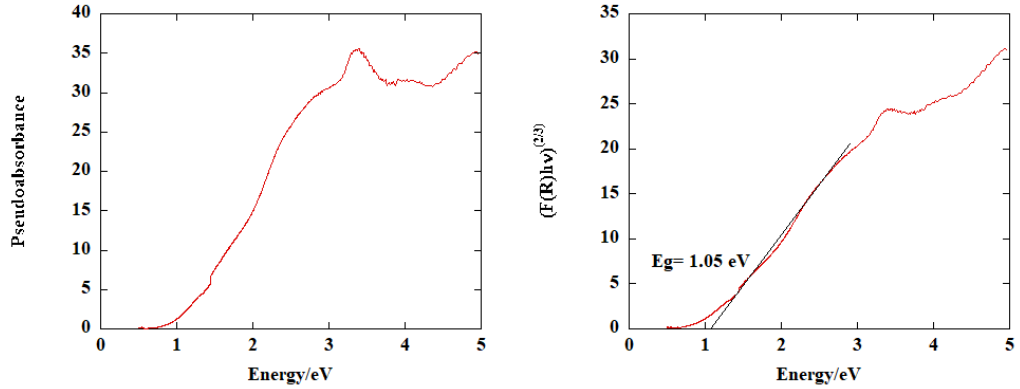

Figure 5.9 $BMPyPb_2I_6$ pseudoabsorbance spectrum and Tauc plot.

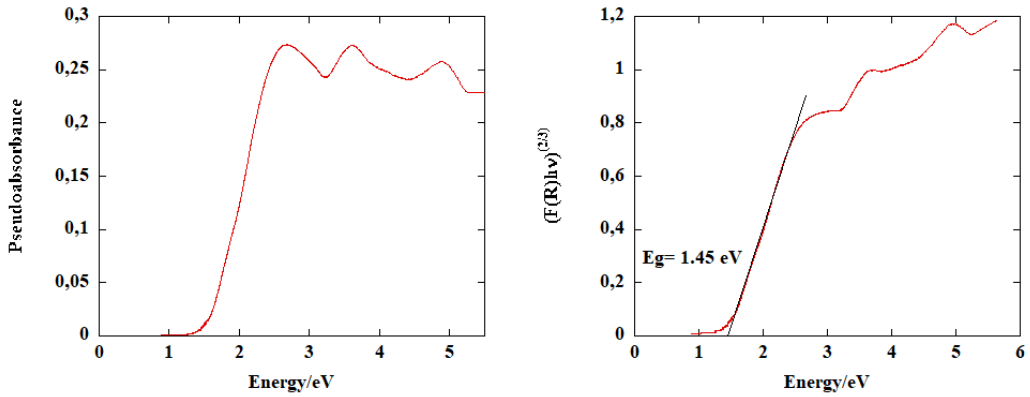

Figure 5.10 $PEPyPb_2I_6$ pseudoabsorbance spectrum and Tauc plot.

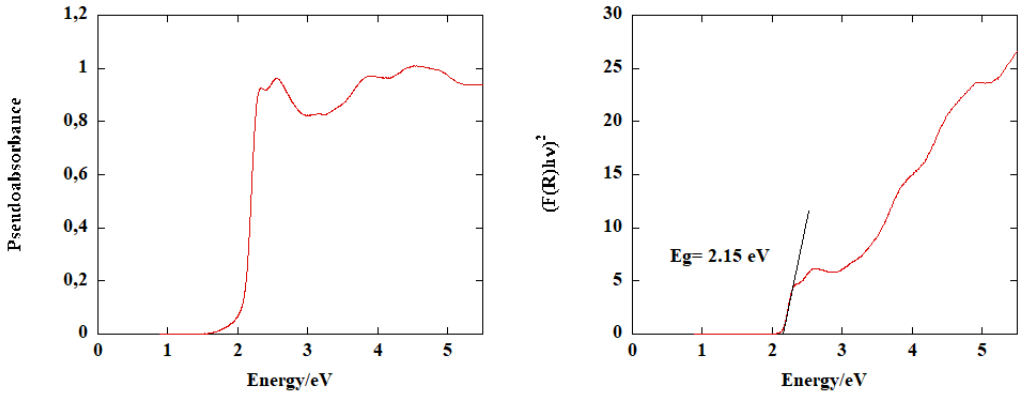

Figure 5.11 $PEPy_3Bi_4I_{18}$ pseudoabsorbance spectrum and Tauc plot.

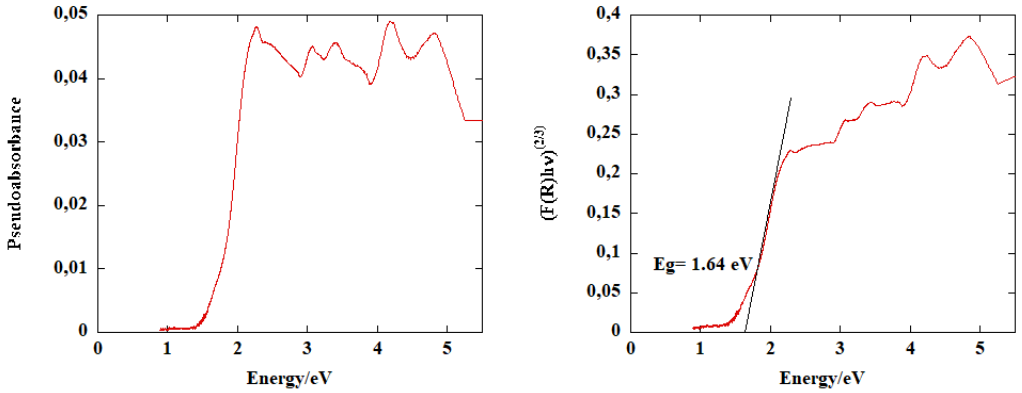

Figure 5.12 $BTPyPb_3I_9$ pseudoabsorbance spectrum and Tauc plot.

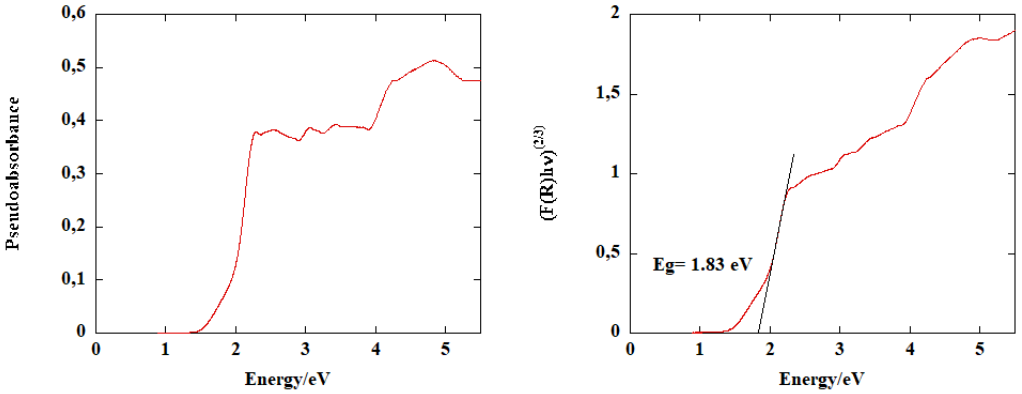

Figure 5.13 $BTPyBiI_6$ pseudoabsorbance spectrum and Tauc plot.

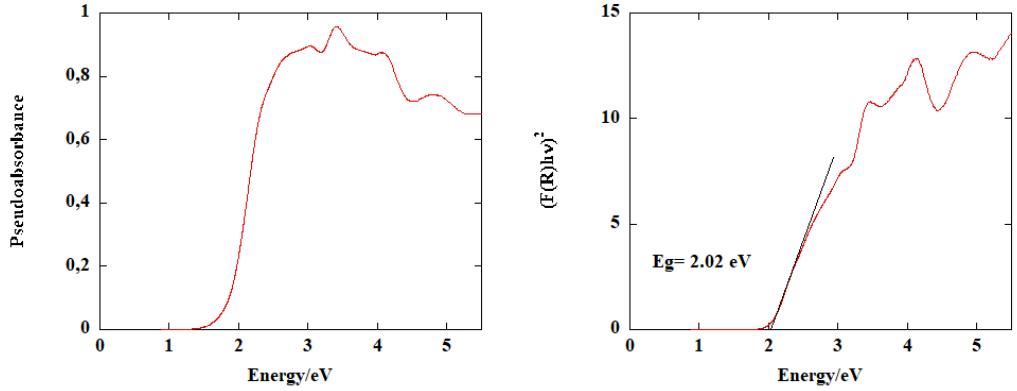

Figure 5.14 $TBMPyPb_2I_6$ pseudoabsorbance spectrum and Tauc plot.

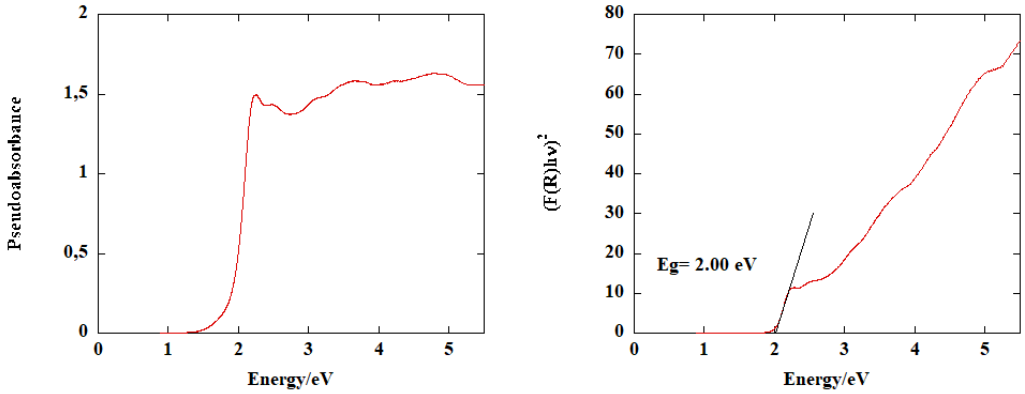

Figure 5.15 $TBMPy_3Bi_4I_{18}$ pseudoabsorbance spectrum and Tauc plot.

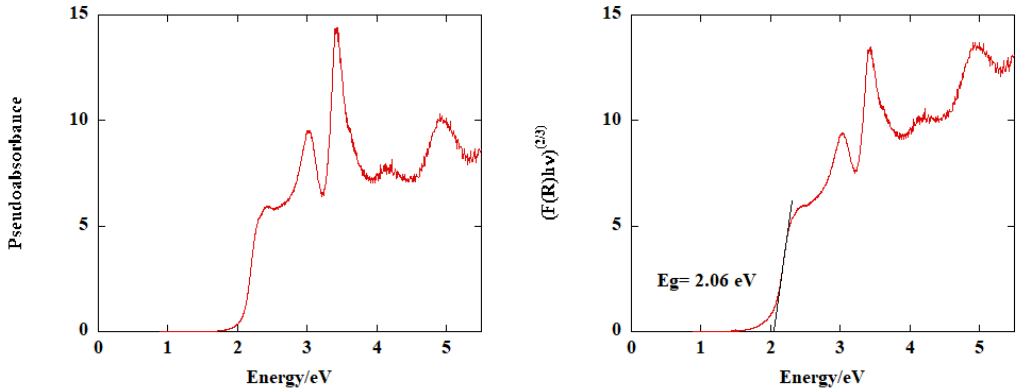

Figure 5.16 $BTBMPyPb_2I_6$ pseudoabsorbance spectrum and Tauc plot.

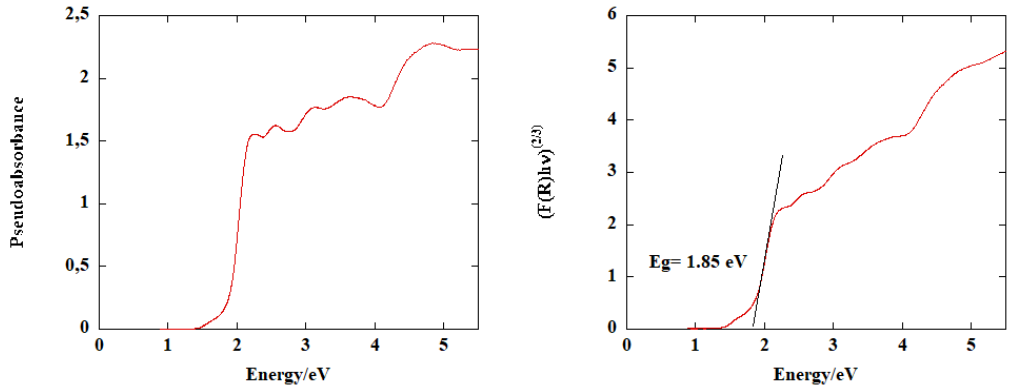

Figure 5.17 $BTBMPy_3Bi_4I_{18}$ pseudoabsorbance spectrum and Tauc plot.

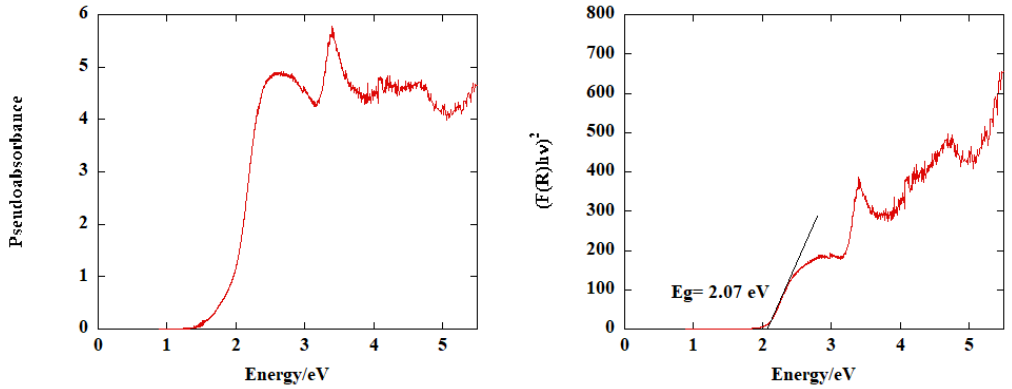

Figure 5.18 $MDAPPb_2I_6$ pseudoabsorbance spectrum and Tauc plot.

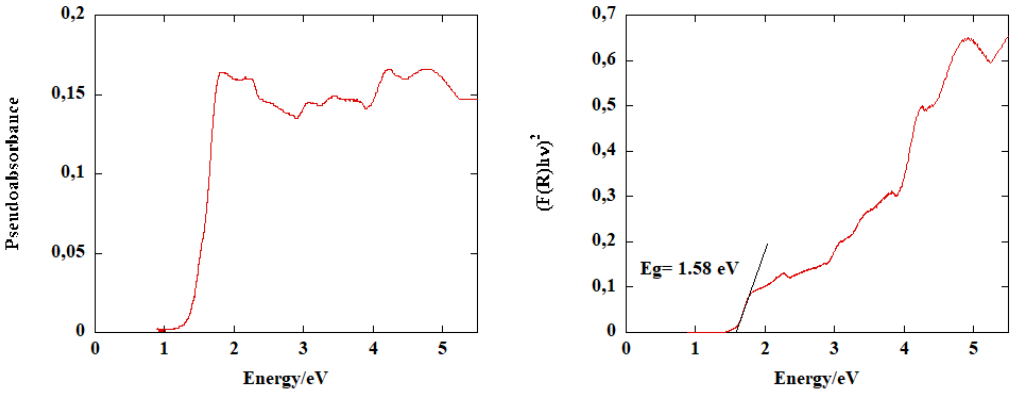

Figure 5.19 $MDAP_3Bi_4I_{18}$ pseudoabsorbance spectrum and Tauc plot.

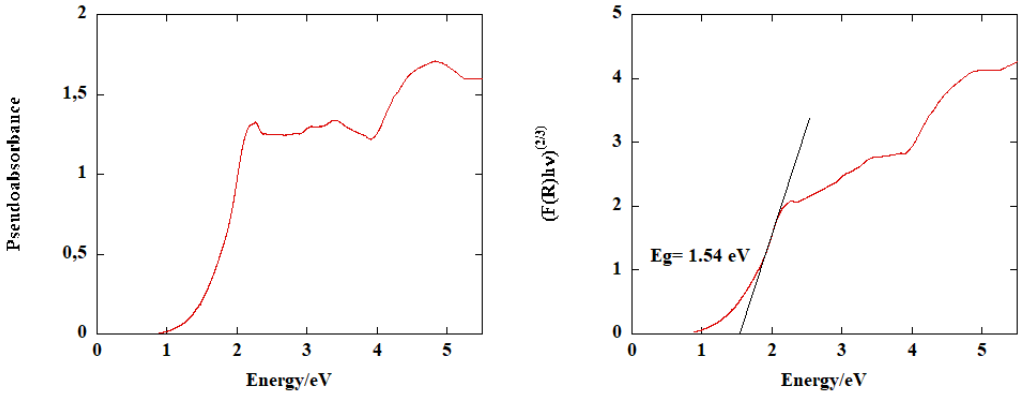

Figure 5.20 $MDPPPb_2I_6$ pseudoabsorbance spectrum and Tauc plot.

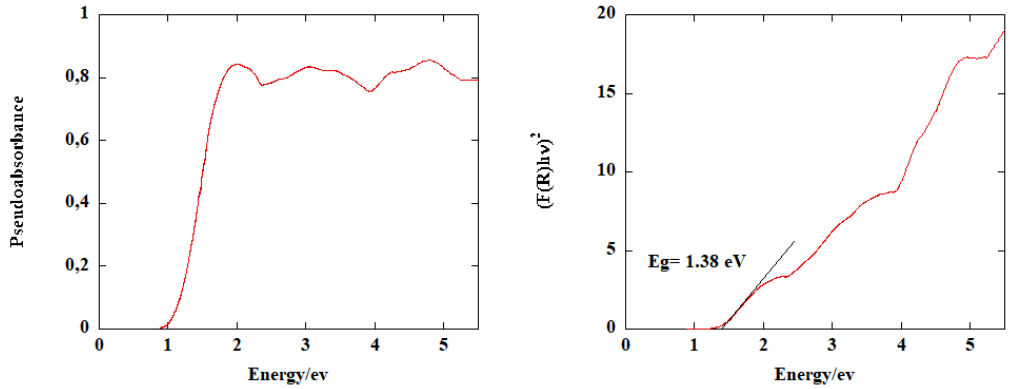

Figure 5.21 $MDPP_3Bi_4I_{18}$ pseudoabsorbance spectrum and Tauc plot.

As it can be seen, the band gap values for the synthesized materials are in the range 1.05-2.15 eV, with several of them possessing E_g around 2 eV, so they do not appear to be particularly suitable for photovoltaic applications. Conversely, **$MDPP_3Bi_4I_{18}$**, with a band gap value of 1.38 eV, and also **$PEPyPb_2I_6$**, with a value of 1.45 eV, could be of some interest in this field, though additional investigation is needed, in order to assess the actual type of transition, and the emissive properties must be investigated too.

Additionally, **$BMPyPb_2I_6$** shows a narrow band gap, of about 1.05 eV; indeed, also this value results to be out of the range of interest for photovoltaics, since a large fraction of the solar radiation would be dissipated as heat, nevertheless it is interesting to note the discrepancy with the behavior of similar compounds.

5.4 Conclusions

As the final part of this work, a series of quaternary pyridinium salts, characterized by the presence of different extendedly conjugated structures, has been synthesized and characterized; subsequently, they have been employed for the preparation of lead and bismuth hybrid perovskites, by mixing of two DMF solutions containing the organic and the metal iodide, followed by precipitation.

The obtained materials resulted to be unreactive in environmental conditions and, in addition, the thermal stability of some of them has been probed through TG-DTA analysis: they have been found to tolerate moderately high temperatures, at least up to 150° C; however, the examined materials appear to be less stable than the two already studied perovskites **AEPyPb$_2$I$_6$** and **AEPy$_3$Bi$_4$I$_{18}$**.

All the hybrid materials prepared by us feature an intense coloration, and the organic precursors show, in most cases, visible fluorescence in solution; the absorption of the perovskites in the UV-visible region has been measured by diffuse reflectance UV-visible spectroscopy and, by their Tauc plots, they have been found to possess band gap values ranging from 1.05 eV to 2.15 eV; notably, the iodoplumbate **BMPyPb$_2$I$_6$** also shows some absorption in the NIR region.

However, an in-depth analysis of the optoelectronic characteristics of these new hybrid perovskites, by means of different techniques, such as PL spectroscopy, in order to understand their emission properties, has not been performed yet; moreover, the determination of their crystal structure, which is necessary in order to make theoretical calculations and relate them with experimental data, is still needed and so the investigation of these new materials is just at an initial stage.

5.5 Experimental section

All the details about the reagents, techniques and instruments used for the synthesis and characterization of the organic compounds have been already described in Chapter 3, section **3.4**.

5.5.1 Synthetic procedures

Synthesis of 1,4-di(pyridin-4-yl)buta-1,3-diyne (3a): In a flame-dried round-bottom flask, 104 mg (1.01 mmol) of 4-ethynylpyridine (**1b**) are dissolved in 33 mL of CH_2Cl_2, then 990 mg (10 mmol) of CuCl and 1.50 mL (10 mmol) of *N*,*N*,*N*′,*N*′-tetramethylethylenediamine (TMEDA) are added and the mixture is stirred overnight under ambient atmosphere. After that time, the mixture is diluted with CH_2Cl_2 (15 mL) and washed with H_2O (3x20 mL) until the aqueous phase is colorless, then it is dried over anhydrous Na_2SO_4 and concentrated under vacuum. The crude product is purified with column chromatography (6:4 petroleum ether/ethyl acetate), to afford 86 mg (0.43 mmol) of pure **3a** (85 %) as a pale brown solid. ^{1}H-NMR ($CDCl_3$, 400 MHz) δ 8.65 (m, 4H), 7.42 (m, 4H); ^{13}C-NMR ($CDCl_3$, 100 MHz) δ 149.67, 129.77, 126.33, 82.68, 80.42.

Synthesis of 4,4'-(buta-1,3-diyne-1,4-diyl)bis(1-methyl-1-pyridinium) diiodide (BMPyI$_2$): In a flame-dried Schlenk tube, 86 mg (0.43 mmol) of **3a** are dissolved in 8 mL of anhydrous CH_2Cl_2 and 1.3 mL (20.2 mmol) of CH_3I are added under argon atmosphere. The mixture is stirred at 40° C overnight, then cooled to room temperature and filtered under vacuum; the collected solid is washed with portions of CH_2Cl_2 and dried for 1 hour under suction, to yield 111 mg (0.23 mmol) of **BMPyI$_2$** as a dark brown solid (53 %). ^{1}H-NMR (DMSO-d_6, 400 MHz) δ 9.10 (m, 4H), 8.42 (m, 4H), 4.37 (s, 6H); ^{13}C-NMR (DMSO-d_6, 100 MHz) δ 146.62, 135.93, 131.06, 81.12, 81.69, 48.76.

Synthesis of 1,4-bis(pyridin-4-ylethynyl)benzene (2a) – Method 1: In a flame-dried Schlenk tube, under argon atmosphere, 8 mL of a degassed and anhydrous 1:1 THF/Et_3N mixture and 448 mg (2.3 mmol) of 4-bromopyridine-HCl (treated as in the synthesis of **1a**) are inserted, followed by 108 mg (0.15 mmol) of $Pd(PPh_3)_2Cl_2$, 15 mg (0.079 mmol) of CuI and 100 mg (0.76 mmol) of 1,4-diethynylbenzene. The mixture is stirred at 70° C for 48 hours, then it is cooled, concentrated under vacuum and the residue is dissolved in ethyl acetate The organic phase is washed with a saturated NH_4Cl solution and then with H_2O, dried over anhydrous Na_2SO_4 and concentrated under vacuum. The crude product is purified by column chromatography (1:1 hexane/ethyl acetate → ethyl acetate), to afford 106 mg (0.379 mmol) of pure **2a** as a white crystalline solid (50 %). ^{1}H-NMR

($CDCl_3$, 400 MHz) δ 8.64 (m, 4H), 7.52 (m, 4H), 7.37 (m, 4H); ^{13}C-NMR ($CDCl_3$, 100 MHz) δ 149.30, 131.47, 130.52, 125.17, 122.44, 92.73, 88.39.

Synthesis of 2a – Method 2: In a flame-dried Schlenk tube, under argon atmosphere, 158 mg (0.48 mmol) of 1,4-diiodobenzene are dissolved in 4 mL of anhydrous and degassed Et_3N**,** then 6 mg (0.0085 mmol) of $Pd(PPh_3)_2Cl_2$, 3 mg (0.016 mmol) of CuI and 100 mg (0.97 mmol) of 4-ethynylpyridine (**1b**) are added and the mixture is stirred for 48 hours at 80° C. After that time, the reaction mixture is cooled, the solvent is evaporated under vacuum and the residue is dissolved in CH_2Cl_2; the organic phase is washed with saturated NaCl solution, dried over anhydrous Na_2SO_4 and concentrated under vacuum. The crude product is purified as in **Method 1** to afford 75 mg (0.267 mmol) of pure **2a** as a white crystalline solid (56 %).

Synthesis of 4,4'-(1,4-phenylenebis(ethyne-2,1-diyl))bis(1-methyl-1-pyridinium) diiodide (PEPyI$_2$): In a flame-dried Schlenk tube, 51 mg (0.181 mmol) of **2a** are dissolved in 5.3 mL of anhydrous CH_2Cl_2 and 0.53 mL (8.5 mmol) of CH_3I are added under argon atmosphere. The mixture is stirred at 40° C for 24 hours, then cooled to room temperature and filtered under vacuum; the solid is washed with portions of CH_2Cl_2 and dried for 1 hour under suction, to yield 88 mg (0.156 mmol) of pure **PEPyI$_2$**, as a yellow solid (86 %).^{1}H-NMR (CD_3OD, 400 MHz) δ 8.93 (m, 4H), 8.20 (m, 4H), 7.82 (s, 4H), 4.40 (s, 6H); ^{13}C-NMR (DMSO-d_6, 100 MHz) δ 146.20, 138.19, 133.44, 129.67, 122.58, 100.73, 88.17, 48.49.

Synthesis of 1,3,5-tris((trimethylsilyl)ethynyl)benzene (4a): In a flame-dried Schlenk tube, under argon atmosphere, 300 mg (0.953 mmol) of 1,3,5-tribromobenzene are dissolved in 20 mL of anhydrous and degassed Et_3N, then 20 mg (0.028 mmol) of $Pd(PPh_3)_2Cl_2$ and 6 mg (0.032 mmol) of CuI are added; the suspension is stirred for 20 minutes at room temperature, then 1 mL (7.2 mmol) of trimethylsilylacetylene are added and the mixture is heated to 65° C and stirred for 24 hours. After that, the reaction mixture is cooled, filtered to remove the solids and concentrated under vacuum. The crude product is purified by column chromatography in hexane to yield 252 mg (0.687 mmol) of pure

4a (72 %) as a pale yellow solid. ^{1}H-NMR ($CDCl_3$, 400 MHz) δ 7.49 (s, 3H), 0.24 (s, 27H); ^{13}C-NMR ($CDCl_3$, 100 MHz) δ 135.17, 122.94, 82.66, 81.67, -0.32.

Synthesis of 1,3,5-triethynylbenzene (4b): In a flame-dried round-bottom flask, under argon atmosphere, 252 mg (0.687 mmol) of **4a** are dissolved in 2.5 mL of anhydrous THF and a solution of 344 mg (6.14 mmol) of anhydrous KOH in 2.5 mL of CH_3OH is added; the reaction mixture is stirred at room temperature overnight, then it is concentrated under vacuum and 8.3 mL of 1 N HCl are added. The solution is extracted with CH_2Cl_2 (3x10 mL), the collected organic phases are dried over anhydrous Na_2SO_4 and concentrated under vacuum, then the crude product is purified by column chromatography in hexane to afford 103 mg (0.687 mmol) of pure **4b** (quantitative yield) as a white volatile solid. ^{1}H-NMR ($CDCl_3$, 400 MHz) δ 7.57 (s, 3H), 3.11 (s, 3H); ^{13}C-NMR ($CDCl_3$, 100 MHz) δ 135.64, 122.95, 81.61, 78.67.

Synthesis of 1,3,5-tris(pyridin-4-ylethynyl)benzene (4c): In a flame-dried Schlenk tube, under argon atmosphere, 60 mg (0.40 mmol) of **4b** are dissolved in 20 mL of anhydrous and degassed Et_3N, together with 389 mg of 4-bromopyridine-HCl (treated as in the synthesis of **1a**), 92 mg (0.08 mmol) of $Pd(PPh_3)_4$ and 4 mg (0.02 mmol) of CuI and the reaction mixture is refluxed for 48 hours. After that, the solvent is evaporated under vacuum, the solid residue is dissolved in ethyl acetate, washed with a saturated NH_4Cl solution and then with H_2O, dried over anhydrous Na_2SO_4 and concentrated under vacuum. The crude product is purified by column chromatography (3:7 → 1.5:8.5 hexane/ethyl acetate), to afford 103 mg (0.27 mmol) of pure **4c** as a pale yellow solid. ^{1}H-NMR ($CDCl_3$, 400 MHz) δ 8.55 (m, 6H), 7.64 (s, 3H), 7.28 (m, 6H); ^{13}C-NMR ($CDCl_3$, 100 MHz) δ 150.16, 135.41, 130.81, 125.71, 123.58, 91.64, 88.42.

Synthesis of 4,4',4''-(benzene-1,3,5-triyltris(ethyne-2,1-diyl))tris(1-methyl-1-pyridinium) triiodide (BTPyI$_3$): In a flame-dried Schlenk tube, 87 mg (0.23 mmol) of **4c** are dissolved in 10 mL of anhydrous CH_2Cl_2 and 12 mL (32.1 mmol) of CH_3I are added under argon atmosphere. The mixture is stirred at 40° C for 48 hours, then it is cooled to room temperature and filtered under vacuum; the solid is washed with several portions of CH_2Cl_2 and dried for 1 hour under suction, to yield 133 mg (0.165 mmol) of

pure **BTPyI$_3$**, as a yellow solid (72 %). ^{1}H-NMR (CD_3OD, 400 MHz) δ 8.95 (m, 6H), 8.25 (m, 6H), 8.24 (s, 3H), 4.42 (s, 9H); ^{13}C-NMR (DMSO-d_6, 100 MHz) δ 146.30, 137.94, 136.19, 129.85, 122.49, 98.77, 87.41, 48.73.

Synthesis of 2,5-bis((trimethylsilyl)ethynyl)thiophene (5a): In a flame-dried Schlenk tube, under argon atmosphere, 10 mL of degassed and anhydrous THF, followed by 0.325 mL (2.38 mmol) of *i*-Pr_2NH and 500 mg (1.49 mmol) of 2,5-diiodothiophene are introduced. Then, 104 mg (0.148 mmol) of $Pd(PPh_3)_2Cl_2$, 30 mg (0.158 mmol) of CuI and 0.625 mL (4.51 mmol) of trimethylsilylacetylene are added and the mixture is heated to 60° C and stirred for 48 hours. After that time, the reaction mixture is cooled, diluted with 10 mL of H_2O and extracted with CH_2Cl_2 (4x15 mL), then the combined organic phases are dried over anhydrous Na_2SO_4 and concentrated under vacuum. The crude product is purified by column chromatography in hexane, to afford 258 mg (0.933 mmol) of pure **5a** (63 %) as a pale yellow solid. ^{1}H-NMR ($CDCl_3$, 400 MHz) δ 7.06 (s, 2H), 0.27 (s, 18H); ^{13}C-NMR ($CDCl_3$, 100 MHz) δ 132.57, 124.50, 100.13, 96.81, -0.21.

Synthesis of 2,5-diethynylthiophene (5b): In a round-bottom flask, 258 mg (0.933 mmol) of **5a** are dissolved in 12.5 mL of methanol, under argon atmosphere, and 517 mg (3.74 mmol) of K_2CO_3 are added. The resulting suspension is stirred overnight at room temperature, then 10 mL of H_2O are added, and the solution is extracted with CH_2Cl_2 (4x15 mL). The combined organic phases are dried over anhydrous Na_2SO_4 and concentrated under vacuum, then the crude product is purified by column chromatography in hexane, to yield 122 mg (0.924 mmol) of pure **5b** (99 %) as a pale-yellow oil. ^{1}H-NMR ($CDCl_3$, 400 MHz) δ 7.14 (s, 2H), 3.38 (s, 2H); ^{13}C-NMR ($CDCl_3$, 100 MHz) δ 132.69, 123.65, 82.15, 76.24.

Synthesis of 2,5-bis(pyridin-4-ylethynyl)thiophene (5c): In a flame-dried Schlenk tube, under argon atmosphere, 122 mg (0.924 mmol) of 2,5-diethynylthiophene (**5b**) are dissolved in 10 mL of a degassed and anhydrous 1:1 THF/Et_3N mixture, then 130 mg (0.185 mmol) of $Pd(PPh_3)_2Cl_2$, 18 mg (0.095 mmol) of CuI and 578 mg (2.82 mmol) of 4-iodopyridine are added. The mixture is stirred for 24 hours at 60° C, then it is cooled, washed with a saturated NH_4Cl solution, and the aqueous phase in washed with ethyl

acetate (3x15 mL). The combined organic phases are dried over anhydrous Na_2SO_4 and concentrated under vacuum, then the crude product is purified by column chromatography (1:1 → 4:6 hexane/ethyl acetate), to afford 222 mg (0.775 mmol) of pure **5c** as a yellow solid (84 %). ^{1}H-NMR ($CDCl_3$, 400 MHz) δ 8.66 (m, 4H), 7.40 (m, 4H), 7.27 (s, 2H); ^{13}C-NMR ($CDCl_3$, 100 MHz) δ 149.76, 133.23, 130.60, 125.28, 124.55, 91.89, 86.44.

Synthesis of 4,4'-(thiophene-2,5-diylbis(ethyne-2,1-diyl))bis(1-methyl-1-pyridinium) diiodide (TBMPyI$_2$): In a flame-dried Schlenk tube, 222 mg (0.775 mmol) of **5c** are dissolved in 15 mL of anhydrous CH_2Cl_2 and 3.5 mL (56.0 mmol) of CH_3I are added under argon atmosphere. The mixture is stirred at 40° C for 24 hours, then it is cooled to room temperature and filtered under vacuum; the solid is washed with portions of CH_2Cl_2 and dried for 1 hour under suction, to yield 358 mg (0.628 mmol) of pure **TBMPyI$_2$**, as an orange solid (81 %). ^{1}H-NMR (DMSO-d_6, 400 MHz) δ 9.03 (m, 4H), 8.30 (m, 4H), 7.82 (s, 2H), 4.34 (s, 6H); ^{13}C-NMR (DMSO-d_6, 100 MHz) δ 146.14, 137.61, 137.43, 129.23, 124.75, 93.93, 91.73, 48.41.

Synthesis of 5,5'-bis((trimethylsilyl)ethynyl)-2,2'-bithiophene (6a): In a flame-dried Schlenk tube, under argon atmosphere, 4 mL of a degassed and anhydrous 7:3 toluene/ *i*-Pr_2NH mixture, followed by 400 mg (0.957 mmol) of 5,5′-diiodo-2,2′-bithiophene are introduced. Then, 55 mg (0.0478 mmol) of $Pd(PPh_3)_4$, 18 mg (0.0957 mmol) of CuI and 0.32 mL (2.31 mmol) of trimethylsilylacetylene are added and the mixture is stirred for 24 hours at room temperature. After that, the solvents are evaporated under vacuum and the residue is purified by column chromatography in hexane, to afford 350 mg (0.956 mmol) of pure **6a** (quantitative yield) as a yellow solid. ^{1}H-NMR ($CDCl_3$, 400 MHz) δ 7.13 (d, 2H, J = 3.8 Hz), 7.02 (d, 2H, J = 3.8 Hz), 0.28 (s, 18H); ^{13}C-NMR ($CDCl_3$, 100 MHz) δ 137.97, 133.48, 123.76, 122.53, 100.52, 97.15, -0.17.

Synthesis of 5,5'-diethynyl-2,2'-bithiophene (6b): In a flame-dried round-bottom flask, under argon atmosphere, 350 mg (0.956 mmol) of **6a** are dissolved in 5 mL of anhydrous THF and a solution of 325 mg (5.8 mmol) of anhydrous KOH in 2.5 mL of CH_3OH is added; the reaction mixture is stirred at room temperature overnight, then $CHCl_3$ is added

and the solution is extracted with water (2x10 mL) and brine (2x10 mL). The organic phase is dried over anhydrous Na_2SO_4 and concentrated under vacuum, then the crude product is purified by column chromatography in hexane, affording 183 mg (0.854 mmol) of pure **6b** as a pale brown solid. ^{1}H-NMR ($CDCl_3$, 400 MHz) δ 7.19 (d, 2H, J = 3.8 Hz), 7.05 (d, 2H, J = 3.8 Hz), 3.44 (s, 2H); ^{13}C-NMR ($CDCl_3$, 100 MHz) δ 138.10, 133.97, 123.92, 121.46, 82.65, 76.65.

Synthesis of 5,5'-bis(pyridin-4-ylethynyl)-2,2'-bithiophene (6c): In a flame-dried Schlenk tube, under argon atmosphere, 183 mg (0.854 mmol) of **6b** are dissolved in 10 mL of a degassed and anhydrous 1:1 THF/Et_3N mixture, then 120 mg (0.171 mmol) of $Pd(PPh_3)_2Cl_2$, 16 mg (0.086 mmol) of CuI and 528 mg (2.59 mmol) of 4-iodopyridine are added. The mixture is stirred for 24 hours at 60° C, then it is cooled, washed with a saturated NH_4Cl solution, and the aqueous phase in washed with ethyl acetate (5x15 mL). The combined organic phases are dried over anhydrous Na_2SO_4 and concentrated under vacuum, then the crude product is purified by column chromatography (1:1 → 2:8 hexane/ethyl acetate), to afford 214 mg (0.581 mmol) of pure **6c** as a yellow solid (68 %). ^{1}H-NMR ($CDCl_3$, 400 MHz) δ 8.65 (m, 4H), 7.38 (m, 4H), 7.28 (d, 2H, J = 4.4 Hz), 7.15 (d, 2H, J = 4.4 Hz); ^{13}C-NMR ($CDCl_3$, 100 MHz) δ 149.79, 139.11, 134.27, 130.82, 125.15, 124.52, 121.62, 92.08, 87.01.

Synthesis of 4,4'-([2,2'-bithiophene]-5,5'-diylbis(ethyne-2,1-diyl))bis(1-methyl-1-pyridinium) diiodide (BTBMPyI$_2$): In a flame-dried Schlenk tube, 214 mg (0.581 mmol) of **6c** are dissolved in 15 mL of anhydrous CH_2Cl_2 and 2.5 mL (40.0 mmol) of CH_3I are added, under argon atmosphere. The mixture is stirred at 40° C for 24 hours, then it is cooled to room temperature and filtered under vacuum; the solid is washed with portions of CH_2Cl_2 and dried for 1 hour under suction, to yield 316 mg (0.484 mmol) of pure **BTBMPyI$_2$**, as a dark orange solid (83 %). ^{1}H-NMR (DMSO-d_6, 400 MHz) δ 8.99 (m, 4H), 8.25 (m, 4H), 7.76 (d, 2H, J = 3.9 Hz), 7.67 (d, 2H, J = 3.9 Hz), 4.33 (s, 6H); ^{13}C-NMR (DMSO-d_6, 100 MHz) δ 146.00, 140.90, 138.61, 137.97, 128.81, 127.55, 119.90, 95.41, 91.92, 48.43.

Synthesis of *N,N′*-dimethyl-1,4,5,8-naphthalenetetracarboxylic diimide (7a): In a round-bottom flask, equipped with a reflux condenser, 16 mL of 40% aqueous methylamine are introduced, followed by 500 mg (1.86 mmol) of 1,4,5,8-naphthalenetetracarboxylic dianhydride. The suspension is refluxed for 3 h, then cooled to 25 °C, filtrated under vacuum, washed with CH_3OH and dried for 1 hour under suction, to afford 537 mg (1.82 mmol) of pure **7a** (98 %) as a pink solid. ^{1}H-NMR ($CDCl_3$, 400 MHz) δ 8.80 (s, 4H), 3.63 (s, 6H); ^{13}C-NMR ($CDCl_3$, 100 MHz) δ 163.31, 131.22, 126.88, 124.53, 27.61.

Synthesis of 1,3,6,8-tetrahydro-2,7-dimethyl-2,7-diazapyrene (7b): A flame-dried round-bottom flask, equipped with a reflux condenser and kept under argon atmosphere, is charged with 12 mL of anhydrous THF, then it is cooled to 0° C and 579 mg (4.34 mmol) of anhydrous $AlCl_3$ are added; when the resulting suspension is dissolved, 489 mg (12.89 mmol) of $LiAlH_4$ are carefully introduced, followed by slow addition of 500 mg (1.70 mmol) of **7a**. The reaction mixture, which becomes immediately red and changes gradually to green, is stirred at room temperature for 1 hour and then refluxed for 3.5 hours under nitrogen. After that time, the mixture is cooled (and it turns yellow) and carefully poured over ice (about 7.5 g), then the precipitate is filtered, dried for 1 hour under vacuum and for 2 hours at 60° C, and subsequently subjected to Soxhlet extraction with 150 mL of $CHCl_3$. The resulting extracted solution is concentrated under vacuum to about 2 mL, then hexane is added until complete precipitation of a green solid, followed by filtration under vacuum and subsequent drying of the precipitate. The reaction affords 216 mg (0.908 mmol) of pure **7b** as a green crystalline solid (53 %). ^{1}H-NMR ($CDCl_3$/CF_3COOD 3:2, 400 MHz) δ 7.53 (s, 4H), 5.01 (dd, 4H, J_1 = 21.7 Hz, J_2 = 14.4 Hz), 4.75 (dd, 4H, J_1 = 21.7 Hz, J_2 = 14.4 Hz), 3.31 (d, 6H, J = 14.4 Hz); ^{13}C-NMR ($CDCl_3$/CF_3COOD 3:2, 100 MHz) δ 125.69, 125.54, 125.12, 56.97, 42.94.

Synthesis of *N,N′*-dimethyl-2,7-diazapyrenium diiodide (MDAPI$_2$): In a flame-dried round-bottom flask, equipped with a reflux condenser and kept under argon atmosphere, 20 mL of anhydrous acetonitrile are added, followed by 100 mg (0.4195 mmol) of **7b**. In the resulting suspension, 571 mg (2.517 mmol) of 2,3-dichloro-5,6-dicyano-1,4-benzoquinone (DDQ) are introduced, and the mixture is stirred for 3 days at 80° C; after

that time, the reaction is cooled and 6.9 mL of 57 % HI are added. The resulting precipitate is filtered under vacuum, washed with acetonitrile and then with diethyl ether and dried under suction for 1 hour, to afford 100 mg (0.206 mmol) of pure **MDAPI$_2$** (49 %) as an orange solid. ^{1}H-NMR (DMSO-d_6, 400 MHz) δ 10.33 (s, 4H), 8.93 (s, 4H), 4.90 (s, 6H); ^{13}C-NMR (DMSO-d_6, 100 MHz) δ 143.19, 130.26, 128.94, 126.28, 50.38.

Synthesis of *N*,*N*'-dimethyl-3,4,9,10-perylenetetracarboxylic diimide (8a): In a round-bottom flask, equipped with a reflux condenser, 25 mL of 40% aqueous methylamine are introduced, followed by 1.100 g (2.80 mmol) of 3,4,9,10-perylenetetracarboxylic dianhydride. The suspension is refluxed for 3 h, then cooled to 25 °C and the obtained solid is separated by centrifugation (5000 rpm for 30 minutes) and washed several times with CH_3OH, to afford 1.170 g (2.80 mmol) of **8a** (quantitative yield) as a red solid. The product is insoluble in all the available deuterated solvent, so it is characterized through ATR-IR spectroscopy: 1698, 1661, 1595, 1398, 1357, 1282, 1053 cm^{-1}.

Synthesis of 1,3,8,10-tetrahydro-2,9-dimethyl-2,9-diazadibenzo[*cd*,*lm*]perylene (8b): A flame-dried round-bottom flask, equipped with a reflux condenser and kept under argon atmosphere, is charged with 25 mL of anhydrous THF, then it is cooled to 0° C and 886 mg (6.64 mmol) of anhydrous $AlCl_3$ are added; when the resulting suspension is dissolved, 771 mg (20.3 mmol) of $LiAlH_4$ are carefully introduced, followed by slow addition of 1170 mg (2.80 mmol) of **8a**. The reaction mixture turns immediately to dark blue, it is subsequently heated and kept to reflux for 4 hours, during which the color changes to dark green; after that, the temperature is lowered to 25° C and the brown suspension is carefully poured over ice (about 27 g). The resulting precipitate is filtered, dried for 1 hour under vacuum and for 4 hours at 60° C, and subsequently subjected to Soxhlet extraction with 250 mL of $CHCl_3$. The extracted solution is concentrated under vacuum to about 5 mL and, after that, hexane is added until complete formation of a brown precipitate; the solid is filtered under vacuum and dried for 1 hour, to afford 624 mg (1.72 mmol) of pure **8b** (63 %) as a brown solid. ^{1}H-NMR (CD_2Cl_2/CF_3COOD 3:2, 400 MHz) δ 8.45 (d, J = 7.8 Hz, 4H), 7.59 (d, J = 7.8 Hz, 4H), 5.10 (dd, J_1 = 15.2 Hz, J_2 =3.6 Hz, 4H), 4.76 (dd, J_1 = 15.2 Hz, J_2 =3.6 Hz, 4H), 3.33 (s, 6H); ^{13}C-NMR

(CD_2Cl_2/CF_3COOD 3:2, 100 MHz) δ 132.25, 128.41, 126.82, 126.29, 123.28, 121.78, 57.53, 42.48.

Synthesis of *N,N'*-dimethyl-2,9-diazaperopyrenium diiodide ($MDPPI_2$): In a flame-dried round-bottom flask, equipped with a reflux condenser and kept under argon atmosphere, 123 mL of anhydrous acetonitrile are added, followed by 624 mg 1.72 mmol) of **8b**. In the resulting suspension, 2.340 g (10.3 mmol) of 2,3-dichloro-5,6-dicyano-1,4-benzoquinone (DDQ) are introduced, and the mixture is stirred for 3 days at 80° C; after that time, the reaction is cooled, and 29.5 mL of 57 % HI are added. The resulting precipitate is filtered under vacuum, washed with acetonitrile, then with diethyl ether and dried under suction for 1 hour, to afford 986 mg (1.61 mmol) of pure **$MDPPI_2$** (94 %) as dark brown solid. ^{1}H-NMR (DMSO-d_6, 400 MHz) δ 10.25 (s, 4H), 9.96 (d, J = 9.6 Hz, 4H), 8.96 (d, J = 9.6 Hz, 4H), 4.95 (s, 6H); ^{13}C-NMR (DMSO-d_6, 100 MHz) δ 140.64, 128.92, 128.83, 128.66, 127.80, 127.14, 121.48, 50.38.

General procedure for the synthesis of perovskites: The organic salt is dissolved in the minimum amount of DMF; if necessary, the mixture is filtered over a 0.45 μm PTFE syringe filter, to remove visible solid particles. To the resulting solution, another solution, containing metal iodide (PbI_2 or BiI_3), following the stoichiometry of equations (23)-(26) is added dropwise, then the mixture is shaken vigorously and exposed to CH_2Cl_2 vapors for varying times, from 72 hours to 2 weeks in a closed container at room temperature (25° C). After that time, the obtained precipitate is filtered under vacuum, washed with several portions of CH_2Cl_2 and allowed to dry for 1 hour under suction to yield the relative hybrid perovskite. Amounts of reagents, times and yields are summarized in **Table 5.1**.

Organic salt	DMF volume	Inorganic salt	DMF volume	Time	Yield
BMPyI$_2$ 214 mg	5 mL	PbI$_2$ 405 mg	4 mL	3 days	350 mg (57%)
PEPyI$_2$ 50 mg	8 mL	PbI$_2$ 65 mg	1 mL	2 weeks	100 mg (87%)
PEPyI$_2$ 50 mg	8 mL	BiI$_3$ 70 mg	1 mL	2 weeks	105 mg (87%)
BTPyI$_3$ 20 mg	1 mL	PbI$_2$ 36 mg	0.5 mL	5 days	47 mg (84%)
BTPyI$_3$ 20 mg	1 mL	BiI$_3$ 16 mg	0.5 mL	5 days	18 mg (50%)
TBMPyI$_2$ 50 mg	3 mL	PbI$_2$ 81 mg	2 mL	5 days	123 mg (94%)
TBMPyI$_2$ 50 mg	3 mL	BiI$_3$ 69 mg	2 mL	2 weeks	88 mg (74%)
BTBMPyI$_2$ 50 mg	3.5 mL	PbI$_2$ 71 mg	1 mL	1 week	111 mg (92%)
BTBMPyI$_2$ 50 mg	3.5 mL	BiI$_3$ 68 mg	1 mL	1 week	83 mg (70%)
MDAPI$_2$ 30 mg	28 mL	PbI$_2$ 57 mg	0.5 mL	5 days	63 mg (72%)
MDAPI$_2$ 30 mg	28 mL	BiI$_3$ 48 mg	0.5 mL	9 days	44 mg (56%)
MDPPI$_2$ 50 mg	35 mL	PbI$_2$ 75 mg	0.5 mL	2 weeks	77 mg (62%)
MDPPI$_2$ 50 mg	35 mL	BiI$_3$ 64 mg	0.5 mL	2 weeks	66 mg (58%)

Table 5.1 Experimental details of the synthesis of perovskites

5.5.2 Characterization techniques

The details about characterization techniques and instruments have already been described in Chapter 3, section **3.4**.

Chapter 6: Conclusions and future perspectives

In the previous chapters, the results of the research done during my PhD have been presented and discussed in detail; the aim of the work was to synthesize and characterize new metal halide hybrid perovskites by focusing the attention on the structure of the organic cation.

The organic species introduced in these materials were designed in such a way to ensure an extended conjugation over their entire structure, so that the optoelectronic properties of the perovskites would arise from the interaction between the inorganic and the organic components and their electronic structures. In addition, the use of quaternary pyridinium salts, without hydrolysable protons, was devised as a way to improve the environmental stability of these materials, since it prevents them from reacting with atmospheric moisture.

Therefore, a series of extended viologens has been synthesized and characterized, and they have been employed for the preparation of lead iodide and bismuth iodide perovskites. All the materials resulted to be water-insensitive, and they can be stored under environmental conditions without special precautions; thermal stability, evaluated for some of them through TG-DTA experiments, also proved to be remarkable. Moreover, the synthesized hybrid materials are semiconductors, and the values of their band gaps, determined by diffuse reflectance UV-visible spectroscopy, vary from 1.05 eV to 2.15 eV, with some of them also in the ideal range for photovoltaic applications.

Two of these hybrid perovskites, namely **AEPyPb$_2$I$_6$** and **AEPy$_3$Bi$_4$I$_{18}$**, have been thoroughly characterized: their crystal structure has been determined, from single-crystal diffraction measurements, they have been proved to be thermally stable up to about 300 °C, their band gap values, of 1.6 eV and 1.64 eV, respectively, have been measured, and both of them have been found to possess an outstandingly bright emission, from PL spectroscopy measurements; additionally, **AEPyPb$_2$I$_6$** electronic band structure has also been derived by DFT calculations. Most notably, the bismuth perovskite **AEPy$_3$Bi$_4$I$_{18}$** shows a comparable stability and band gap to its lead counterpart, but its PL intensity is much higher, with the additional advantage of containing a non-toxic metal.

For all the other perovskites, many fundamental characterizations are still lacking: for example, their crystal structure is still unknown, and PL experiments, aimed at evaluating

their emission properties, have not been performed yet; however, the interesting band gap values found, the absence of reactivity towards water and their solution processability make them extremely promising materials for optoelectronic applications. For these reasons, one of the main purposes in the prosecution of this work will be a deeper characterization of all the synthesized hybrid materials, in particular as regards their optical and electronic properties, besides the determination of their crystal structure, which is also necessary to calculate their electronic band structure.

At the same time, it will be important to verify if the long-term stability in environmental conditions for all the synthesized perovskites is as good as it has been found for **AEPyPb$_2$I$_6$** and **AEPy$_3$Bi$_4$I$_{18}$** and if thin films can be prepared of these materials (which has been already proved feasible for **AEPyPb$_2$I$_6$**), a very important requirement in view of their application in real devices. The implementation in real devices, such as solar cells or LEDs, of these novel organic-inorganic hybrids will also be one of the future goals of the research; the use for light emission of the two already characterized perovskites seems particularly propitious, owing to their intense photoluminescence.

In conclusion, the use of extendedly conjugated quaternary ammonium cations in hybrid perovskites has revealed a very successful strategy to achieve environmentally and thermally stable materials with enhanced optoelectronic properties, and the possibility to tailor the structure of the cations through organic synthesis brings about almost unlimited opportunities in this rapidly expanding field. Additionally, the use of bismuth instead of lead has proved a particularly favorable alternative, giving rise to safer materials characterized by comparable, or even better, performances with the same remarkable stability.

Related papers

The results of the research described in this thesis have also been published in the following papers:

[1] Romagnoli, Lorenza; D'Annibale, Andrea; Blundo, Elena; Polimeni, Antonio; Cassetta, Alberto; Chita, Giuseppe; Panetta, Riccardo; Ciccioli, Andrea; Latini, Alessandro, "Synthesis, Structure, and Characterization of 4,4′-(Anthracene-9, 10-diylbis(ethyne-2,1-diyl))bis(1-methyl-1-pyridinium) Bismuth Iodide $(C_{30}H_{22}N_2)_3Bi_4I_{18}$, an Air, Water, and Thermally Stable 0D Hybrid Perovskite with High Photoluminescence Efficiency". *Cryst. Growth Des.* **2022**, *22*, 7426-7433.

[2] Romagnoli, Lorenza; D'Annibale, Andrea; Blundo, Elena; Patra, Atanu; Polimeni, Antonio; Meggiolaro, Daniele; Andrusenko, Iryna; Marchetti, Danilo; Gemmi, Mauro; Latini, Alessandro, "4,4′-(Anthracene-9,10-diylbis(ethyne-2,1-diyl))bis(1-methyl-1-pyridinium) Lead Iodide $C_{30}H_{22}N_2Pb_2I_6$: A Highly Luminescent, Chemically and Thermally Stable One-Dimensional Hybrid Iodoplumbate". *Chem. Mater.* **2023**, *35*, 1818-1826.

References

[1] Kickelbick, G. *Hybrid Materials: Synthesis, Characterization, and Applications* Wiley-VCH Verlag GmbH & Co. KGaA, Weinheim, **2007**.

[2] Chujo, Y. *Curr. Opin. Solid State Mater. Sci*. **1996**, *1*, 806-811.

[3] Ashby, M. F., Bréchet, Y. J. M. *Acta Materialia* **2003**, *51*, 5801-5821.

[4] Hench, L. L., West, J. K. *Chem. Rev.* **1990**, *90*, 33-72.

[5] Schubert, U., Hüsing, N., Lorenz, A. *Chem. Mater.* **1995**, *7*, 2010-2027.

[6] Gómez-Romero, P., Sanchez, C. *Functional Hybrid Materials* Wiley-VCH Verlag GmbH & Co. KGaA, Weinheim, **2004**.

[7] Faustini, M., Nicole, L., Ruiz-Hitzky, E., Sanchez, C. *Adv. Funct. Mater.* **2018**, 28, 1704158.

[8] Komarneni, S. *J. Mater. Chem.* **1992**, *2*, 1219-1230.

[9] Rurack, K., Martínez-Máñez, R. *The Supramolecular Chemistry of Organic–Inorganic Hybrid Materials* John Wiley & Sons, Inc., Hoboken, **2010**.

[10] de Paiva, L. B., Morales, A. R., Valenzuela Díaz, F. R. *Appl. Clay Science* **2008**, *42*, 8–24.

[11] He, H., Ma, L., Zhu, J., Frost, R. L., Theng, B. K. G., Bergaya, F. *Appl. Clay Science* **2014**, *100*, 22-28.

[12] Okada, A., Usuki, A. *Macromol. Mater. Eng.* **2006**, *291*, 1449-1476.

[13] Zajickova, Z. *J. Sep. Sci.* **2017**, *40*, 25-48.

[14] Peter, J., Nechikkattu, R., Mohan, A., Maria Thomas A., Ha, C.-S. *Mater. Sci. Eng., B* **2021**, *270*, 115232.

[15] Li, G., Wang, L., Pittman Jr., C. U. *J. Inorg. Organomet. Polym.* **2001**, 123-154.

[16] Qi, W., Wu, L. *Polym. Int.* **2009**, *58*, 1217-1225.

[17] Allcock, H. R., *Adv. Mater.* **1994**, *6*, 106-115.

[18] Ogoshi, T., Chujo, Y. *Compos. Interfaces* **2005**, *11*, 539-566.

[19] Mitzi, D. B. *Prog. Inorg. Chem.* **1999**, *48*, 1–121.

[20] Mitzi, D. B. *J. Chem. Soc., Dalton Trans.* **2001**, 1–12.

[21] Zhao, Y., Zhu, K. *Chem. Soc. Rev.* **2016**, *45*, 655-689.

[22] Pan, S., Li, J., Wen, Z., Lu, R., Zhang, Q., Jin, H., Zhang, L., Chen, Y., Wang, S. *Adv. Energy Mater.* **2022**, *12*, 2004002.

[23] Petrus, M. L., Schlipf, J., Li, C., Gujar, T. P., Giesbrecht, N., Müller-Buschbaum, P., Thelakkat, M., Bein, T., Hüttner, S., Docampo, P. *Adv. Energy Mater.* **2017**, *7*, 1700264.

[24] Kim, J. Y., Lee, J.-W., Jung, H. S., Shin, H., Park, N.-G. *Chem. Rev.* **2020**, *120*, 7867–7918.

[25] Lekesi, L.P., Koao, L.F., Motloung, S.V., Motaung, T.E., Malevu, T. *Appl. Sci.* **2022**, *12*, 672.

[26] Le, Q. V., Jang, H. W., Kim, S. Y. *Small Methods* **2018**, *2*, 1700419.

[27] Jia, P., Lu, M., Sun, S., Gao, Y., Wang, R., Zhao, X., Sun, G., Colvin, V. L., Yu, W. W. *Adv. Mater. Interfaces* **2021**, *8*, 2100441.

[28] Sutherland, B. R., Sargent, E. H. *Nat. Photonics* **2016**, *10*, 295–302.

[29] Zhang, Q., Su, R., Du, W., Liu, X., Zhao, L., Ha, S. T., Xiong, Q. *Small Methods* **2017**, *1*, 1700163.

[30] Ahmadi, M., Wu, T., Hu, B. *Adv.Mater.* **2017**, *29*, 1605242.

[31] Kojima, A., Teshima, K., Shirai, Y., Miyasaka, T. *J. Am. Chem. Soc.* **2009**, *131*, 6050–6051.

[32] Green, M. A., Dunlop, E. D., Hohl-Ebinger, J., Yoshita, M., Kopidakis, N., Bothe, K., Hinken, D., Rauer, M., Hao, X. *Prog. Photovolt.: Res. Appl.* **2022**, *30*, 687–701.

[33] Lee, D.-K., Park, N.-G. *Sol. RRL* **2022**, *6*, 2100455.

[34] Yan, J., Savenije, T. J., Mazzarella, L., Isabella, O. *Sustainable Energy Fuels* **2022**, *6*, 243–266.

[35] West, A. R. *Solid State Chemistry and its Applications, Second Edition, Student Edition* John Wiley & Sons, Ltd, Chichester, **2014**.

[36] Johnsson, M., Lemmens, P. *Crystallography and Chemistry of Perovskites. Handbook of Magnetism and Advanced Magnetic Materials* John Wiley & Sons, Ltd, **2007**.

[37] Papavassiliou, G. C. *Mol. Cryst. Liq. Cryst.* **1996**, *286*, 231–238.

[38] Tanaka, K., Takahashi, T., Ban, T., Kondo, T., Uchida, K., Miura, N. *Solid State Commun.* **2003**, *127*, 619–623.

[39] Binek, A., Hanusch, F. C., Docampo, P., Bein, T. *J. Phys. Chem. Lett.* **2015**, *6*, 1249−1253.

[40] Weller, M. T., Weber, O. J., Frost, J. M., Walsh, A. *J. Phys. Chem. Lett.* **2015**, *6*, 3209−3212.

[41] Han. Q., Bae, S.-H., Sun, P., Hsieh, Y.-T., Yang, Y. (M.), Rim, Y. S., Zhao, H., Chen, Q., Shi, W., Li, G., Yang, Y. *Adv. Mater.* **2016**, *28*, 2253–2258.

[42] Stoumpos, C. C., Malliakas, C. D., Kanatzidis, M. G *Inorg. Chem.* **2013**, *52*, 9019−9038.

[43] Shockley, W., Queisser, H. J. *J. Appl. Phys.* **1961**, *32*, 510–519.

[44] Galkowski, K., Mitioglu, A., Miyata, A., Plochocka, P., Portugall, O., Eperon, G. E., Wang, J. T., Stergiopoulos, T., Stranks, S. D., Snaith, H. J., Nicholas, R. J. *Energy Environ. Sci.*, **2016**, *9*, 962-970.

[45] Stranks, S. D., Eperon, G. E., Grancini, G., Menelaou, C., Alcocer, M. J. P., Leijtens, T., Herz, L. M., Petrozza, A., Snaith, H. J. *Science*, **2013**, *342*, 341-344.

[46] Chen, Y., Peng, J., Su, D., Chen, X., Liang, Z. *ACS Appl. Mater. Interfaces* **2015**, *7*, 4471−4475.

[47] Im, J.-H., Lee, C.-R., Lee, J.-W., Park, S.-W., Park, N.-G. *Nanoscale*, **2011**, *3*, 4088–4093.

[48] Papavassiliou, G. C., Koutselas, I. B., *Synth. Met.* **1995**, *71*, 1713–1714.

[49] Papavassiliou, G. C., *Prog. Solid State Chem.* **1997**, *25*, 125–270

[50] Arya, S., Mahajan, P., Gupta, R., Srivastava, R., Tailor, N. K., Satapathi, S., Sumathi, R. R., Datt, R., Gupta, V. *Prog. Solid State Chem.*, **2020**, *60*, 100286.

[51] Zheng, L., Zhang, D., Ma, Y., Lu, Z., Chen, Z., Wang, S., Xiao, L., Gong, Q. *Dalton Trans.*, **2015**, *44*, 10582-10593.

[52] Park, N.-G. *Mater. Today* **2015**, *18*, 65-72.

[53] Kim, H.-S., Lee, C.-R., Im, J.-H., Lee, K.-B., Moehl, T., Marchioro, A., Moon, S.-J., Humphry-Baker, R., Yum, J.-H., Moser, J. E., Grätzel, M., Park, N.-G. *Sci. Rep.* **2012**, *2***,** 591.

[54] Lee, M. M., Teuscher, J., Miyasaka, T., Murakami, T. N., Snaith, H. J. *Science* **2012**, *338***,** 643–647.

[55] Liu, M., Johnston, M. B., Snaith, H. J. *Nature* **2013**, *501*, 395–398.

[56] Ball, J. M., Lee, M. M., Hey, H., Snaith, H. J. *Energy Environ. Sci.*, **2013**, *6*, 1739–1743.

[57] Docampo, P., Ball, J., Darwich, M., Eperon, G. E., Snaith, H. J. *Nat. Commun.* **2013**, *4*, 2761.

[58] Scopus, document search for "planar perovskite solar cells" and "mesoporous perovskite solar cells".

[59] Zhao, X., Park, N.-G. *Photonics* **2015**, *2*, 1139-1151.

[60] Huang, J., Tan, S., Lund, P. D., Zhou, H. *Energy Environ. Sci.* **2017**, *10*, 2284-2311.

[61] Aristidiou, N., Sanchez-Molina, I., Chotchuangchutchaval, T., Brown, M., Martinez, L., Rath, T., Haque, S. A. *Angew. Chem.* **2015**, *127*, 8326 –8330.

[62] Conings, B., Drijkoningen, J., Gauquelin, N., Babayigit, A., D'Haen, J., D'Olieslaeger, L., Ethirajan, A., Verbeeck, J., Manca, J., Mosconi, E., De Angelis, F., Boyen, H.-G. *Adv. Energy Mater.* **2015**, *5*, 1500477.

[63] Alberti, A., Deretzis, I., Pellegrino, G., Bongiorno, C., Smecca, E., Mannino, G., Giannazzo, F., Condorelli, G. G., Sakai, N., Miyasaka, T., Spinella, C., La Magna, A. *ChemPhysChem* **2015**, *16*, 3064−3071.

[64] Kim, N.-K., Min, Y. H., Noh, S., Cho, E., Jeong, G., Joo, M., Ahn, S.-W., Lee, J. S., Kim, S., Ihm, K., Ahn, H., Kang, Y., Lee, H.-S., Kim, D. *Sci. Rep.* **2017**, *7*, 4645.

[65] Ciccioli, A., Latini, A., *J. Phys. Chem. Lett.* **2018**, *9*, 3756-3765.

[66] Noh, J. H., Im, S. H., Heo, J. H., Mandal, T. N., Seok, S. I. *Nano Lett.* **2013**, *13*, 1764–1769.

[67] Hamed, M. S. G., Mola, G. T. *Crit. Rev. Solid State Mater. Sci.* **2020**, 45, 85–112.

[68] Pellet, N., Gao, P., Gregori, G., Yang, T.-Y., Nazeeruddin, M. K., Maier, J., Grätzel, M. *Angew. Chem. Int. Ed.* **2014**, *53*, 3151 –3157.

[69] Lee, J.-W., Kim, D.-H., Kim, H.-S., Seo, S.-W., Cho, S. M., Park, N.-G. *Adv. Energy Mater.* **2015**, *5*, 1501310.

[70] Zheng, Z., Wang, S., Hu, Y., Rong, Y., Mei, A., Han, H. *Chem. Sci.*, **2022**, *13*, 2167-2183.

[71] Zhao, P., Kim, B. J., Jung, H. S. *Mater. Today Energy* **2018**, *7*, 267-286.

[72] Aranda, C. A., Caliò, L., Salado, M. *Crystals* **2021**, *11*, 519.

[73] Urbina, A. *J. Phys. Energy* **2020,** *2*, 022001.

[74] Schileo, G., Grancini, G. *J. Mater. Chem. C* **2021**, *9*, 67-76.

[75] Vidal, R., Alberola-Borràs, J.-A., Habisreutinger, S.N. Gimeno-Molina, J.-L., Moore, D. T., Schloemer, T. H., Mora-Seró, I., Berry, J. J., Luther, J. M. *Nat. Sustain.* **2021**, *4*, 277–285.

[76] Hailegnaw, B., Kirmayer, S., Edri, E., Hodes, G., Cahen, D. *J. Phys. Chem. Lett.* **2015**, *6*, 1543–1547.

[77] Shi, Z., Guo, J., Chen, Y., Li, Q., Pan, Y., Zhang, H., Xia, Y., Wang, W. *Adv. Mater*. **2017**, *29*, 1605005.

[78] Hoefler, S.F., Trimmel, G., Rath, T. *Monatsh Chem.* **2017**, *148*, 795–826.

[79] Wang, M., Wang, W., Ma, B., Shen, W., Liu, L., Cao, K., Chen, S., Huang, W. *Nano-Micro Lett.* **2021**, *13*, 62.

[80] Nasti, G., Abate, A. *Adv. Energy Mater.* **2020**, *10*, 1902467.

[81] Yang, W.-F., Igbari, F., Lou, Y.-H., Wang, Z.-K., Liao, L.-S. *Adv. Energy Mater.* **2020**, *10*, 1902584.

[82] Stoumpos, C. C., Malliakas, C. D., Kanatzidis, M. G. *Inorg. Chem.* **2013**, *52*, 9019–9038.

[83] Yu, B.-B., Chen, Z., Zhu, Y., Wang, Y., Han, B., Chen, G., Zhang, X., Du, Z., He, Z. *Adv. Mater.* **2021**, *33*, 2102055.

[84] Noel, N. K., Stranks, S. D., Abate, A., Wehrenfennig, C., Guarnera, S., Haghighirad, A.-A., Sadhanala, A., Eperon, G. E., Pathak, S. K., Johnston, M. B., Petrozza, A., Herz, L. M., Snaith, H. G. *Energy Environ. Sci.*, **2014**, *7*, 3061-3068.

[85] Krishnamoorthy, T., Ding, H., Yan, C., Leong, W. L., Baikie, T., Zhang, L., Sherburne, M., Li, S., Asta, M., Mathews, N., Mhaisalkar, S. G. *J. Mater. Chem. A*, **2015**, *3*, 23829-23832.

[86] Ghosh, S., Shankar, H., Kar, P. *Mater. Adv.* **2022**, *3*, 3742–3765.

[87] Lee, L. C., Huq, T. N., MacManus-Driscoll, J. L., Hoye, R. L. Z. *APL Mater.* **2018**, *6*, 084502.

[88] Park, B.-W., Philippe, B., Zhang, X., Rensmo, H., Boschloo, G., Johansson, E. M. J. *Adv. Mater.* **2015**, *27*, 6806–6813.

[89] Feray Ü., Deo, M., Mathur, S., Kirchartz, T., Kulkarni, A. *J. Phys. D: Appl. Phys.* **2022**, *55*, 113002.

[90] Sun, J., Yang, J., Lee, J. I., Cho, J. H., Kang, M. S. *J. Phys. Chem. Lett.* **2018**, *9*, 1573−1583.

[91] Zhang, Y., Ma, Y., Wang, Y., Zhang, X., Zuo, C., Shen, L., Ding, L. *Adv. Mater.* **2021**, *33*, 2006691.

[92] Zhou, C., Lin, H., He, Q., Xu, L., Worku, M., Chaaban, M., Lee, S., Shi, X., Du, M.-H., Ma, B. *Mater. Sci. Eng., R.* **2019**, *137*, 38-65.

[93] Li, Y.-T., Han, L., Liu, H., Sun, K., Luo, D., Guo, X.-L., Yu, D.-L., Ren, T.-L. *ACS Appl. Electron. Mater.* **2022**, *4*, 547-567.

[94] Milot, R. L., Sutton, R. J., Eperon, G. E., Haghighirad, A. S., Hardigree, J. M., Miranda, L., Snaith, H. G., Johnston, M. B., Herz, L. M. *Nano Lett.* **2016**, *16*, 7001–7007.

[95] Wang, D., Wen, B., Zhu, Y.-N., Tong, C.-J., Tang, Z.-K., Liu, L.-M. *J. Phys. Chem. Lett.* **2017**, *8*, 876−883.

[96] Stoumpos, C. C., Cao, D. H., Clark, D. J., Young, J., Rondinelli, J. M., Jang, J. I., Hupp, J. T., Kanatzidis, M. G. *Chem. Mater.* **2016**, *28*, 2852–2867.

[97] Mao, L., Ke, W., Pedesseau, L., Wu, Y., Katan, C., Even, J., Wasielewski, M. R., Stoumpos, C. C., Kanatzidis, M. G. *J. Am. Chem. Soc.* **2018**, *140*, 3775−3783.

[98] Zhu, L., Liu, D., Wang, J., Wang, N. *J. Phys. Chem. Lett.* **2020**, *11*, 8502−8510.

[99] Zheng, K., Pullerits, T. *J. Phys. Chem. Lett.* **2019**, *10*, 5881−5885.

[100] Chen, P., Bai, Y., Lyu, M., Yun, J.-H., Hao, M., Wang, L. *Sol. RRL* **2018**, 1700186.

[101] Zhou, C., Tian, Y., Yuan, Z., Lin, H., Chen, B., Clark, R., Dilbeck, T., Zhou, Y., Hurley, J., Neu, J., Besara, T., Siegrist, T., Djurovich, P. I., Ma, B. *ACS Appl. Mater. Interfaces* **2017**, *9*, 44579–44583.

[102] Xu, L.-J., Sun, C.-Z., Xiao, H., Wu, Y., Chen, Z.-N. *Adv. Mater.* **2017**, 1605739.

[103] Zhou, C., Worku, M., Neu, J., Lin, H., Tian, Y., Lee, S., Zhou, Y., Han, D., Chen, S., Hao, A., Djurovich, P. I., Siegrist, T., Du, M.-H., Ma, B. *Chem. Mater.* **2018**, *30*, 2374−2378.

[104] Im, J.-H., Chung, J., Kim, S.-J. Park, N.-G. *Nanoscale Res. Lett.* **2012**, *7*, 353.

[105] Dimesso, L., Quintilla, A., Kim, Y.-M., Lemmer, U., Jaegermann, W. *Mater Sci Eng B.* **2016**, *204*, 27-33.

[106] Panetta, R., Righini, G., Colapietro, M., Barba, L., Tedeschi, D., Polimeni, A., Ciccioli, A., Latini, A. *J. Mater. Chem. A* **2018**, *6*, 10135–10148.

[107] Elsenety, M. M., Kaltzoglou, A., Antoniadou, M., Koutselas, I., Kontos, A. G., Falaras, P. *Polyhedron* **2018**, *150*, 83–91.

[108] Zhou, L., Shi, P.-P., Liu, X.-M., Feng, J.-C., Ye, Q., Yao, Y.-F., Fu, D.-W., Li, P.-F., You, Y.-M., Zhang, Y., Xiong, R.-G. *NPG Asia Mater* **2019**, *11*, 15.

[109] Chen, Y., Sun, Y., Peng, J., Tang, J., Zheng, K., Liang, Z. *Adv. Mater.* **2018**, *30*, 1703487.

[110] Maughan, A. E., Kurzman, J. A., Neilson, J. R. *Inorg. Chem.* **2015**, *54*, 370−378.

[111] Evans, H. A., Lehner, A. J., Labram, J. G., Fabini, D. H., Barreda, O., Smock, S. R., Wu, G., Chabinyc, M L., Seshadri, R., Wudl, F. *Chem. Mater.* **2016**, *28*, 3607−3611.

[112] Umeyama, D., Leppert, L., Connor, B. A., Manumpil, M. A., Neaton, J. B., Karunadasa, H. I. *Angew. Chem. Int. Ed.* **2020**, *59*, 19087 – 19094.

[113] Saparov, B., Mitzi, D. B. *Chem. Rev.* **2016**, *116*, 4558−4596.

[114] Mitzi, D. B., Chondroudis, K., Kagan, C. R. *Inorg. Chem.* **1999**, *38*, 6246−6256.

[115] Véron, A. C., Linden, A., Leclaire, N. A., Roedern, E., Hu, S., Ren, W., Rentsch, D., Nüesch, F. A. *J. Phys. Chem. Lett.* **2018**, *9*, 2438−2442.

[116] Xu, Z., Mitzi, D. B., Medeiros, D. R. *Inorg. Chem.* **2003**, *42*, 1400-1402.

[117] Zheng, X., Chen, B., Dai, J., Fang, Y., Bai, Y., Lin, Y., Wei, H., Zeng, X. C., Huang, J. *Nat. Energy* **2017**, *2*, 17102.

[118] Poli, I., Eslava, S., Cameron, P. *J. Mater. Chem. A* **2017**, *5*, 22325–22333.

[119] Jamaludin, N. F., Sum, T. C., Mathews, N., Soci, C., Mhaisalkar, S. G. *ChemPhysChem* **2018**, *19*, 1075–1080.

[120] Ciccioli, A., Panetta, R., Luongo, A., Brunetti, B., Vecchio Ciprioti, S., Mele, M. L., Latini, A. *Phys. Chem. Chem. Phys.* **2019**, *21*, 24768-24777.

[121] Liu, J.-J., Shan, Y.-B., Dai, W.-X., Huang, C.-C., Lin, M.-J. *Dalton Trans.* **2017**, *46*, 11556–11560.

[122] Wang, Y., Zhang, J., Huang, J., Zhang, H., Fu, H. *CrystEngComm* **2018**, *20*, 2089-2092.

[123] Febriansyah, B., Koh, T. M., John, R. A., Ganguly, R., Li, Y., Bruno, A., Mhaisalkar, S. G., England, J. *Chem. Mater.* **2018**, *30*, 5827−5830.

[124] Lei, Y., Wang, S., Xing, J., Xu, H., Han, J., Liu, W. *Inorg. Chem.* **2020**, *59*, 4349−4356.

[125] Michaelis, L. *Biochem. Z.* **1932**, *250*, 564-567.

[126] Michaelis, L., Hill, E. S. *Gen. Physiol.* **1933**, *16*, 859-873.

[127] Macfarlane, A. J., Williams, R. J. P. *J. Chem. Soc. A* **1969**, 1517-1520.

[128] Schoot, C. J., Ponjee, J. J., van Dam, H. T., van Doorn, R. A., Bolwijn, P. T. *Appl. Phys. Lett.* **1973**, *23*, 64-65.

[129] Shi, Z., Neoh, K. G., Kang, E. T. *Biomaterials*, **2005**, *26*, 501-508.

[130] Wang, L., Sun, S., Zhang, B., Yang, L., Yao, Y., Zhuang, X., Chen, Y. *Eur. Polym. J.*, **2017**, *94*, 222-229.

[131] Fahrenbach, A. C., Sampath, S., Late, D. J., Barnes, J. C., Kleinman, S. L., Valley, N., Hartlieb, K. J., Liu, Z., Dravid, V. P., Schatz, G. C., Van Duyne, R. P., Stoddart, J. F. *ACS Nano*, **2012**, *6*, 9964-9971.

[132] Trabolsi, A., Khashab, N., Fahrenbach, A. C., Friedman, D. C., Colvin, M. T., Cotí, K. K., Benítez, D., Tkatchouk, E., Olsen, J.-C., Belowich, M. E., Carmielli, R., Khatib, H. A., Goddard III, W. A., Wasielewski, M. R., Stoddart, J. F. *Nat. Chem.* **2010**, *2*, 42-49.

[133] Buyukcakir, O., Je, S. H., Choi, D. S., Talapaneni, S. N., Seo, Y., Jung, Y., Polychronopoulou, K., Coskun, A. *Chem. Commun.* **2016**, *52*, 934-937.

[134] Ogawa, M., Balan, B., Ajayakumar, G., Masaoka, S., Kraatz, H.-B., Muramatsu, M., Ito, S., Nagasawa, Y., Miyasaka, H., Sakai, K. *Dalton Trans.* **2010**, *39*, 4421–4434.

[135] Maufroy, A., Favereau, L., Anne, F. B., Pellegrin, Y., Blart, E., Hissler, M., Jacquemin, D., Odobel, F. *J. Mater. Chem. A* **2015**, *3*, 3908–3917.

[136] Ding, J., Zheng, C., Wang, L., Lu, C., Zhang, B., Chen, Y., Li, M., Zhai, G., Zhuang, X. *J. Mater. Chem. A* **2019**,*7*, 23337-23360.

[137] Appel, E. A., Del Barrio, J., Dyson, J., Isaacs, L., Scherman, O. A. *Chem. Sci.* **2012**, *3*, 2278–2281.

[138] Wang, N., Damlin, P., Esteban, B. E., Ääritalo, T., Kankare, J., Kvarnström, C. *Electrochim. Acta*, **2013**, *90*, 171-178.

[139] Katir, N., El Kadib, A., Collière, V., Majoral, J. P., Bousmina, M. *Chem. Commun.* **2014**, *50*, 6981-6983.

[140] Yamashita, Y., Hanaoka, T., Takeda, Y., Mukai, T., Miyashi, T. *B. Chem. So. Jpn.* **1988**, *61*, 2451-2458.

[141] Porter III, W. W., Vaid, T. P., Rheingold, A. L. *J. Am. Chem. Soc.* **2005**, *127*, 16559–16566.

[142] Fortage, J., Tuyèras, F., Peltier, C., Dupeyre, G., Calboréan, A., Bedioui, F., Ochsenbein, P., Puntoriero, F., Campagna, S., Ciofini, I., Lainé, P. P. *J. Phys. Chem. A* **2012**, *116*, 7880–7891.

[143] Bakupog, T., Clennan, E. L., Zhang, X. *Tetrahedron Lett.*, **2015**, *56*, 5591-5594.

[144] Hoffmann, M., Kärnbratt, J., Chang, M.-H., Herz, L. M., Albinsson, B., Anderson, H. L. *Angew. Chem., Int. Ed.*, **2008**, *47*, 4993-4996.

[145] Latini, A., Quaranta, S., Menchini, F., Lisi, N., Di Girolamo, D., Tarquini, O., Colapietro, M., Barba, L., Demitri, N., Cassetta, A. *Dalton Trans.* **2020**, *49*, 2616-2627.

[146] Ge, B.-D., Wei, Q., Sun, A.-H., Lin, C.-Y., Duan, X.-F., Li, J.-H., Wang, G.-M. *Chem. Asian J.* **2019**, *14*, 2086–2090.

[147] Xiao, X., Nagahara, L. A., Rawlett, A. M., Tao, N. *J. Am. Chem. Soc.* **2005**, *127*, 9235-9240.

[148] Liu, J., Lam, J. W. Y., Tang, B. Z. *Chem. Rev.* **2009**, *109*, 5799–5867.

[149] Chauhan, A., Chauhan, P. *J. Anal. Bioanal. Tech.* **2014**, *5*, 212.

[150] Bunaciu, A. A., Udriștioiu, E. G., Aboul-Enein, H. Y. *Crit. Rev. Anal. Chem.* **2015**, *45*, 289-299.

[151] Henderson, R. *Proc. R. Soc. Lond. B.* **1990**, *241***,** 6–8.

[152] Gates-Rector, S., Blanton, T. *Powder Diffr.* **2019**, *34*, 352-360.

[153] Smith, D. K. *Powder Diffr.* **2001**, *16*, 186-191.

[154] Harris, K. D. M., Cheung, E. Y. *Chem. Soc. Rev.* **2004**, *33*, 526-538.

[155] Haeger, T., Heiderhoff, R., Riedl, T. *J. Mater. Chem. C* **2020**, *8*, 14289-14311.

[156] Coats, A. W., Redfern, J. P. *Analyst* **1963**, *88*, 906-924.

[157] Saadatkhah, N., Carillo Garcia, A., Ackermann, S., Leclerc, P., Latifi, M., Samih, S., Patience, G. S., Chaouki, J. *Can. J. Chem. Eng.* **2020**, *98*, 34–43.

[158] Mahajan, A., Kingon, A., Kukovecz, Á., Konya, Z., Vilarinho, P. M. *Mat. Lett.* **2013**, *90*, 165-168.

[159] Paulik, F., Paulik, J. *Analyst* **1978**, *103*, 417-437.

[160] Ozawa, T., *Termochim. Acta* **2000**, *355*, 35-42.

[161] Materazzi, S. *Appl. Spectr. Rev.* **1997**, *32*, 385-404.

[162] Materazzi, S. *Appl. Spectr. Rev.* **1998**, *33*, 189-218.

[163] Kortüm, G., Braun, W., Herzog, G. *Angew. Chem. Int. Ed.* **1963**, *2*, 333-341.

[164] Torrent, J., Barrón, V. *Diffuse reflectance spectroscopy* in Ulery, A. L., Drees, L. R. (Eds.), *Methods of soil analysis part 5: Mineralogical methods* (pp. 367–387). Soil Science Society of America.

[165] Kubelka, P., Munk, F. *Z. Techn. Phys.* **1931**, *12*, 593-601.

[166] Kortüm, G. *Experimental Testing of the "Kubelka-Munk" Theory* in *Reflectance Spectroscopy* **1969**, Springer, Berlin, Heidelberg.

[167] Makuła, P., Pacia, M., Macyk, W. *J. Phys. Chem. Lett.* **2018**, *9*, 6814-6817.

[168] Tauc, J., Grigorovici, R., Vancu, A. *Phys. Status Solidi B* **1966**, *15*, 627−637.

[169] Davis, E. A., Mott, N. F. *Philos. Mag.* **1970**, *22*, 903-922.

[170] Pankove, J. I. *Optical Processes in Semiconductors* **1971**, Courier Corporation.

[171] Sonogashira, K., Tohda, Y., Hagihara, N. *Tetrahedron Lett.* **1975**, *50*, 4467-4470.

[172] Sonogashira, K. *J. Organomet. Chem.* **2002**, *653*, 46−49.

[173] Ziessel, R., Suffert, J., Youinou, M.T. *J. Org. Chem.* **1996**, *61*, 6535-6546.

[174] Winter, S., Weber, E., Eriksson, L., Csöregh, I. *New J. Chem.* **2006**, *30*, 1808-1819.

[175] McIlroy, S. P., Cló, E., Nikolajsen, L., Frederiksen, P. K., Nielsen, C. B., Mikkelsen, K. V., Gothelf, K. V., Ogilby, P. R. *J. Org. Chem.* **2005**, *70*, 1134-1146.

[176] Ogawa, A., Curran, D. P. *J. Org. Chem.* **1997**, *62*, 450–451.

[177] Gemmi, M., Mugnaioli, E., Gorelik, T. E., Kolb, U., Palatinus, L., Boullay, P., Hovmöller, S., Abrahams, J. P. *ACS Cent. Sci.* **2019**, *5*, 1315-1329.

[178] Huang, Z., Willhammar, T., Zou, X. *Chem. Sci.* **2021**, *12*, 1206-1219.

[179] Otten, M. T. *J. Electron. Microsc. Tech.* **1991**, *17*, 221–230.

[180] Jesson, D. E., Pennycock, S. J. *Proc. R. Soc. A.* **1995**, *449*, 273-293.

[181] Zhang, Y. B., Su, J., Furukawa, H., Yun, Y., Gándara, F., Duong, A., Zou, X., Yaghi, O.M. *J. Am. Chem. Soc.* **2013**, *135*, 16336-16339.

[182] Das, P. P., Mugnaioli, E., Nicolopoulos, S., Tossi, C., Gemmi, M., Galanis, A., Borodi, G., Pop, M. M. *Org. Process Res. Dev.* **2018**, *22*, 1365-1372.

[183] Andrusenko, I., Hamilton, V., Lanza, A. E., Hall, C. L., Mugnaioli, E., Potticary, J., Buanz, A., Gaisford, S., Piras, A. M., Zambito, Y., Hall, S. R., Gemmi, M. *Int. J. Pharm.* **2021**, *608*, 121067.

[184] Richter, J. M., Abdi-Jalebi, M., Sadhanala, A., Tabachnyk, M., Rivett, J. P. H., Pazos-Outón, L. M., Gödel, K. C., Price, M., Deschler, F., Friend, R. H. *Nat. Commun.* **2016**, *7*, 13941.

[185] Poli, I., Kim, G.-W., Wong, E. L., Treglia, A., Folpini, G., Petrozza, A. *ACS Energy Lett.* **2021**, *6*, 609–611.

[186] Pazos-Outón, L. M., Szumilo, M., Lamboll, R., Richter, J. M., Crespo-Quesada, M., Abdi-Jalebi, M., Beeson, H. J., Vrućinić, M., Alsari, M., Snaith, H. J., Ehrler, B., Friend, R. H. Deschler, F. *Science* **2016**, *351*, 1430- 1433.

[187] Baroni, S., De Gironcoli, S., Dal Corso, A., Giannozzi, P. *Rev. Mod. Phys.* **2001**, *73*, 515-562.

[188] Perdew, J. P., Burke, K., Ernzerhof, M. *Phys. Rev. Lett.* **1996**, *77*, 3865−3868.

[189] Lanza, A., Margheritis, E., Mugnaioli, E., Cappello, V., Garau, G., Gemmi, M. *IUCrJ* **2019**, *6*, 178-188.

[190] Nederlof, I., van Genderen, E., Li, Y. W., Abrahams, J. P. *Acta Crystallogr. D* **2013**, *69*, 1223-1230.

[191] Mugnaioli, E., Gorelik, T., Kolb, U. *Ultramicroscopy* **2009**, *109*, 758−765.

[192] Palatinus, L., Brázda, P., Jelínek, M., Hrdá, J., Steciuk, G., Klementová, M. *Acta Crystallogr. B* **2019**, *75*, 512-522.

[193] Burla, M. C., Caliandro, R., Carrozzini, B., Cascarano, G. L., Cuocci, C., Giacovazzo, C., Mallamo, M., Mazzone, A., Polidori, G. *J. Appl. Crystallogr.* **2015**, *48*, 306-309.

[194] Sheldrick, G. M. *Acta Crystallogr. C* **2015**, *71*, 3-8.

[195] Petříček, V., Dušek, M., Palatinus, L. *Z. Z. Kristallogr. Cryst. Mater.* **2014**, *229*, 345-352.

[196] Giannozzi, P., Baroni, S., Bonini, N., Calandra, M., Car, R., Cavazzoni, C., Ceresoli, D., Chiarotti, G. L., Cococcioni, M., Dabo, I., Dal Corso, A., de Gironcoli, S., Fabris, S., Fratesi, G., Gebauer, R., Gerstmann, U., Gougoussis, C., Kokalj, A., Lazzeri, M., Martin-Samos, L., Marzari, N., Mauri, F., Mazzarello, R., Paolini, S., Pasquarello, A., Paulatto, L., Sbraccia, C., Scandolo, S., Sclauzero, G., Seitsonen, A. P., Smogunov, A., Umari, P., Wentzcovitch, R. M. *J. Phys.: Condens. Matter* **2009**, *21*, 395502.

[197] Grimme, S., Antony, J., Ehrlich, S., Krieg, H. *J. Chem. Phys.* **2010**, *132*, 154104.

[198] Marini, A., Hogan, C., Grüning, M., Varsano, D. *Comput. Phys. Commun.* **2009**, *180*, 1392-1403.

[199] Blundo, E., Polimeni, A., Meggiolaro, D., D'Annibale, A., Romagnoli, L., Felici, M., Latini, A. *J. Phys. Chem. Lett.* **2021**, *12*, 5456-5462.

[200] Chen, X., Myung, Y., Thind, A., Gao, Z., Yin, B., Shen, M., Cho, S. B., Cheng, P., Sadtler, B., Mishra, R., Banerjee, P. *J. Mater. Chem. A* **2017**, *5*, 24728-24739.

[201] Bernstorff, S., Busetto, E., Gramaccioni, C., Lausi, A., Olivi, L., Zanini, F., Savoia, A., Colapietro, M., Portalone, G., Camalli, M., Pifferi, A., Spagna, R., Barba, L., Cassetta, A. *Rev. Sci. Instrum.* **1995**, *66*, 1661−1664.

[202] Lausi, A., Polentarutti, M., Onesti, S. Plaisier, J. R., Busetto, E., Bais, G., Barba, L., Cassetta, A., Campi, G., Lamba, D., Pifferi, A., Mande, S. C., Sarma, D. D., Sharma, S. M., Paolucci, G. *Eur. Phys. J. Plus* **2015**, *130*, 43.

[203] Eckhardt, K., Bon, V., Getzschmann, J., Grothe, J., Wisser, F. M., Kaskel, S. *Chem. Commun.* **2016**, *52*, 3058−3060.

[204] Park, B.-W., Philippe, B., Zhang, X., Rensmo, H., Boschloo, G., Johansson, E. M. J. *Adv. Mater.* **2015**, *27*, 6806−6813.

[205] D'Annibale, A., Panetta, R., Tarquini, O., Colapietro, M., Quaranta, S., Cassetta, A., Barba, L., Chita, G., Latini, A. *Dalton Trans.* **2019**, *48*, 5397−5407.

[206] Yang, B., Chen, J., Hong, F., Mao, X., Zheng, K., Yang, S., Li, Y., Pullerits, T., Deng, W., Han, K. *Angew. Chem., Int. Ed.* **2017**, *56*, 12471−12475.

[207] Hoye, R. L. Z., Brandt, R. E., Osherov, A., Stevanovic, V., Stranks, S. D., Wilson, M. W. B., Kim, H., Akey, A. J., Perkins, J. D., Kurchin, R. C., Poindexter, J. R., Wang, E. N., Bawendi, M. G., Bulović, V., Buonassisi, T. *Chem. - Eur. J.* **2016**, *22*, 2605−2610.

[208] Altomare, A., Cuocci, C., Giacovazzo, C., Moliterni, A., Rizzi, R., Corriero, N., Falcicchio, A. *J. Appl.Crystallogr.* **2013**, *46*, 1231-1235.

[209] Kabsch, W. *Acta Crystallogr. D* **2010**, *66*, 125−132.

[210] Sheldrick, G. M. *SADABS, Software for Empirical Absorption Corrections*, University of Göttingen: Göttingen, **1996**.

[211] Sheldrick, G. M. *Acta Crystallogr. A* **2015**, *71*, 3-8.

[212] Sheldrick, G. M. *Acta Crystallogr. A* **2015**, *71*, 3-8.

[213] Dolomanov, O. V., Bourhis, L. J., Gildea, R. J., Howard, J. A. K., Puschmann, H. *J. Appl. Crystallogr.* **2009**, *42*, 339-341.

[214] Ozores, H. L., Amorín, M., Granja, J. R. *J. Am. Chem. Soc.* **2017**, *139*, 776–784.

[215] Jellen, M. J., Ayodele, M. J., Cantu, A., Forbes, M. D. E., Garcia-Garibay, M. A. *J. Am. Chem. Soc.* **2020**, *142*, 18513–18521.

[216] Kaae, B. H., Harpsøe, K., Kvist, T., Mathiesen, J. M., Mølck, C., Gloriam, D., Jimenez, H. M., Uberti, M. A., Nielsen, S. M., Nielsen, B., Bräuner-Osborne, H., Sauerberg, P., Clausen, R. P., Madsen, U. *ChemMedChem* **2012**, *7*, 440-451.

[217] Bivaud, S., Balandier, J.-Y., Chas, M., Allain, M., Goeb, S., Sallé, M. *J. Am. Chem. Soc.* **2012**, *134*, 11968–11970.

[218] Hagiwara, S., Ishida, Y., Masui, D., Shimada, T., Takagi, s. *Clay Science* **2013**, *17*, 7-10.

[219] Xie, Y., Wang, T.-T., Yang, R.-X., Huang, N.-Y., Zou, K., Deng, W.-Q., *ChemSusChem 2014, 7*, 2110-2114.

[220] Yuan, K., Zhuang, X., Fu, H., Brunklaus, G., Forster, M., Chen, Y., Feng, X., Scherf, U. *Angew. Chem. Int. Ed.* **2016**, *55*, 6858-6863.

[221] Anderson, H. L., Walter, C. J., Vidal-Ferran, A., Hay, R. A., Lowden, P. A., Sanders, J. K. M. *J. Chem. Soc. Perkin Trans.* **1995**, *1*, 2275-2279.

[222] Barbarella, G., Melucci, M., Sotgiu, G. *Adv. Mater.* **2005**, *17*, 1581-1593.

[223] Turkoglu, G., Cinar, M. E., Ozturk, T. *Thiophene-Based Organic Semiconductors* in *Sulfur Chemistry. Topics in Current Chemistry Collections*, **2019**, Springer, Cham.

[224] Roncali, J. *Chem. Rev.* **1992**, *92*, 711-738.

[225] Mishra, A., Ma, C.-Q., Bäuerle, P. *Chem. Rev.* **2009**, *109*, 1141–1276.

[226] Neenan, T. X., Whitesides, G. M. *J. Org. Chem.* **1988**, *53*, 2489-2496.

[227] Hwang, E., Lusker, K. L., Garno, J. C., Losovyi, Y., Nesterov, E. E. *Chem. Commun.* **2011**,*47*, 11990-11992.

[228] Stang, P. J., Cao, D. H., Saito, S., Arif, A. M., *J. Am. Chem. Soc.* **1995**, *117*, 6273 – 6283.

[229] Sotiriou-Leventis, C., Mao, Z., Rawashdeh, A.-M. M. *J. Org. Chem.* **2000**, *65*, 6017-6023.

[230] Basuray, A. N., Jacquot de Rouville, H.-P., Hartlieb, K. J., Kikuki, T., Strutt, N. L., Bruns, C. J., Ambrogio, M. W., Avestro, A.-J., Schneebeli, S. T., Fahrenbach, A. C., Stoddart, J. F. *Angew. Chem. Int. Ed.* **2012**, *51*, 11872 –11877.

Appendix: ^{1}H NMR and ^{13}C NMR spectra of the organic salts

AEPyI$_2$ ^{1}H NMR

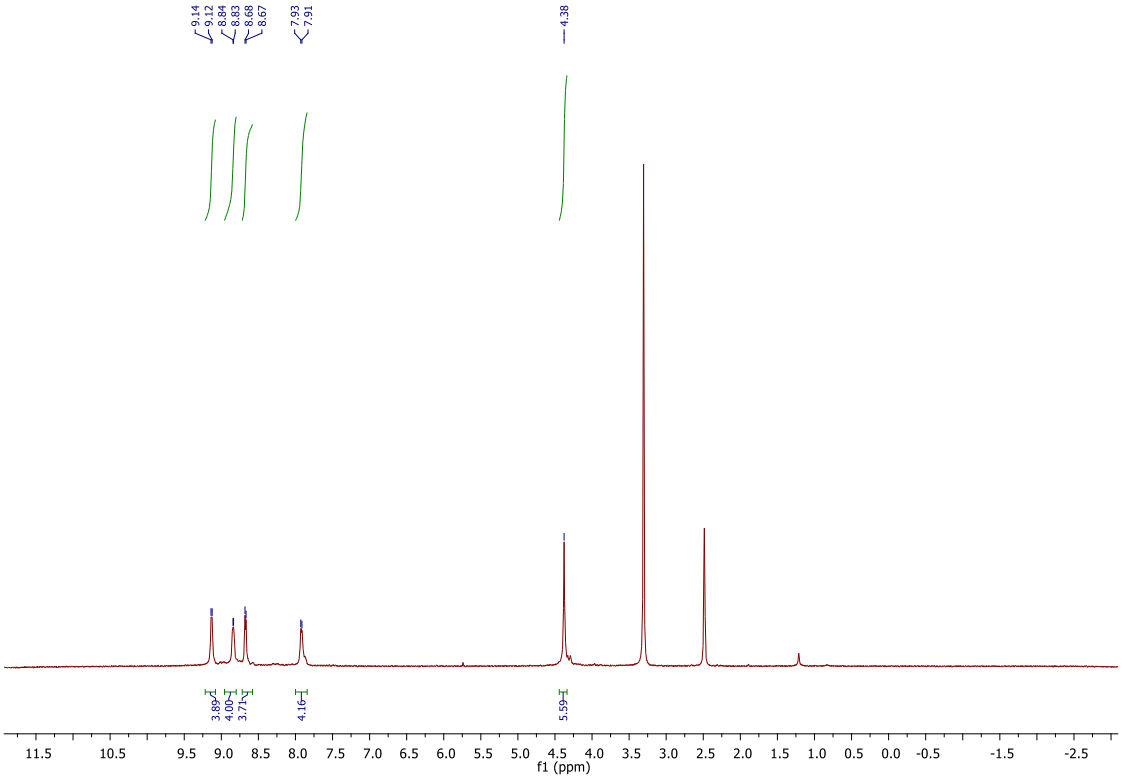

AEPyI$_2$ ^{13}C NMR

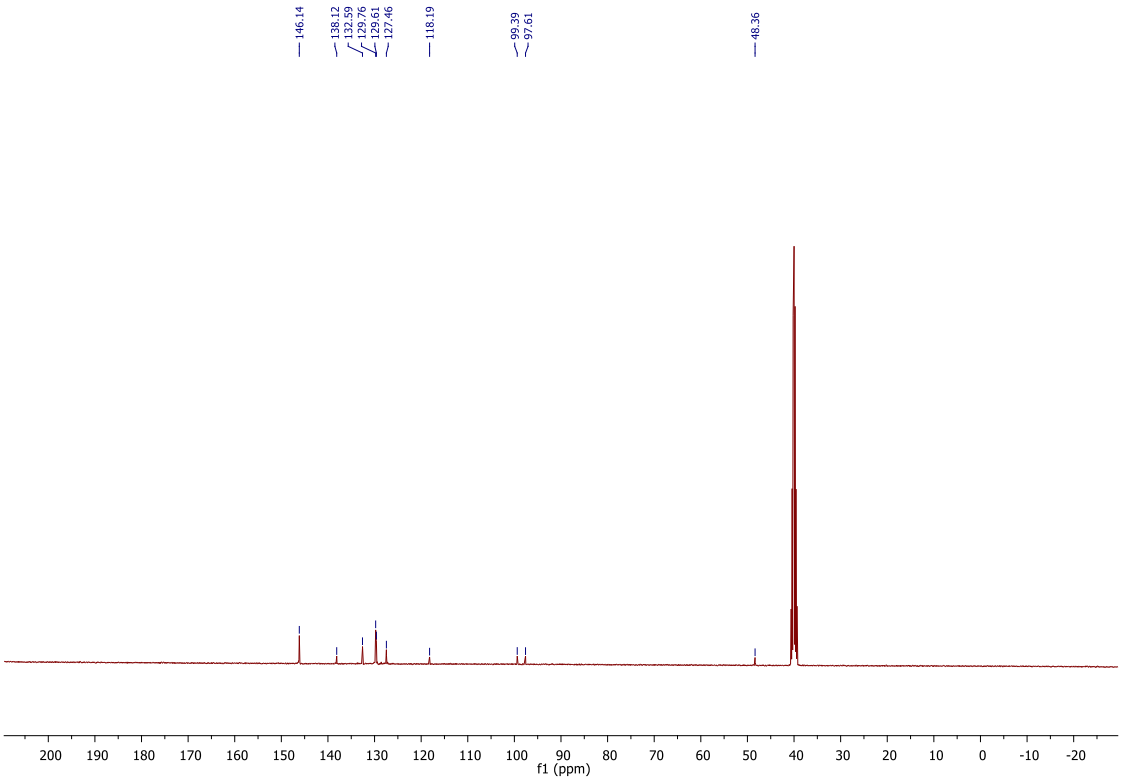

BMPyI$_2$ ^{1}H NMR

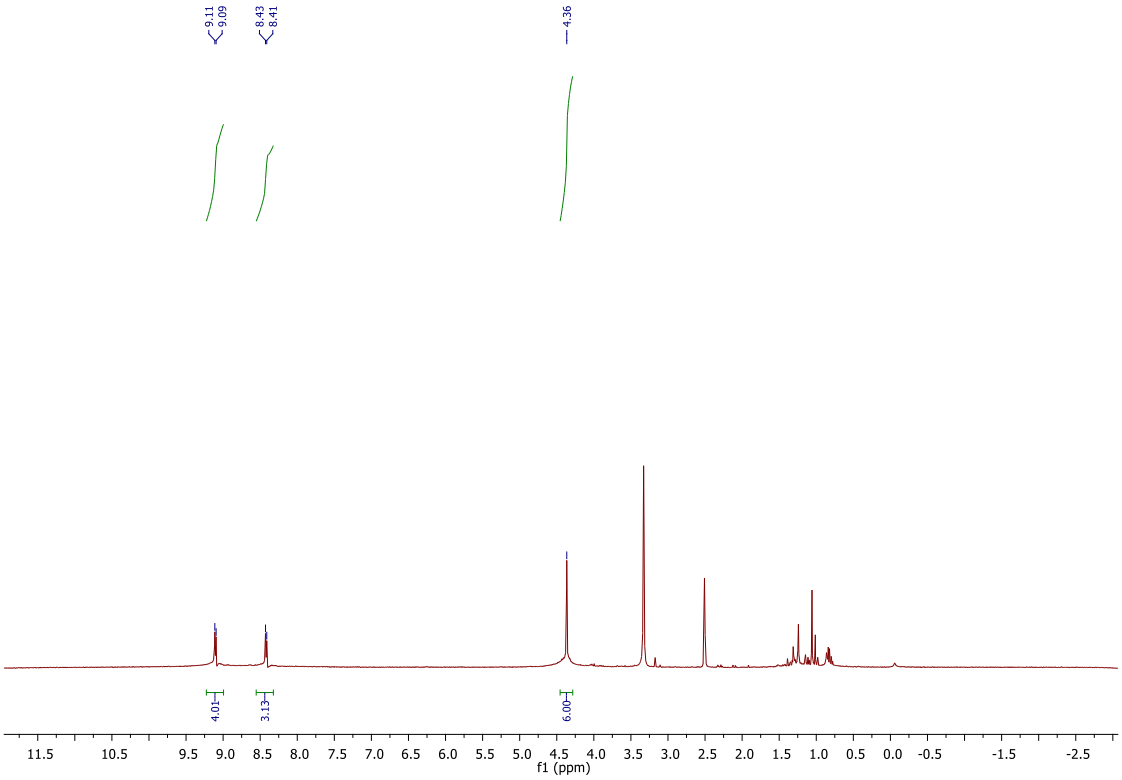

BMPyI$_2$ ^{1}H NMR

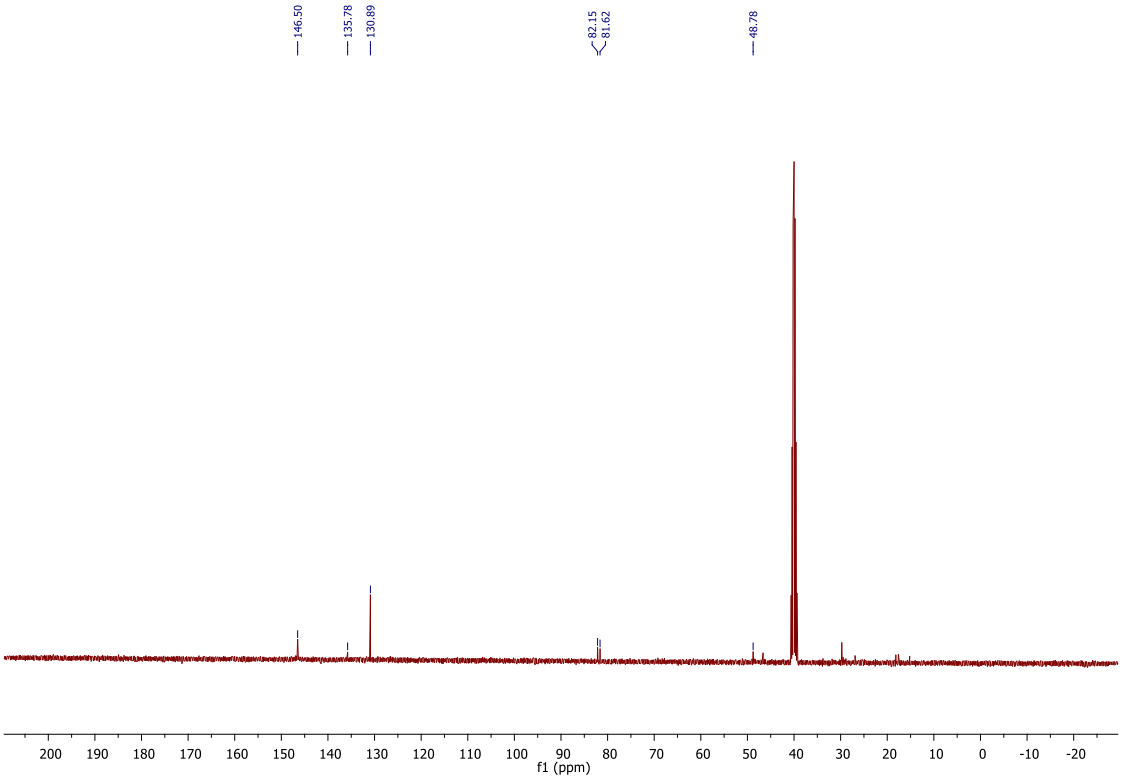

PEPyI$_2$ ^{1}H NMR

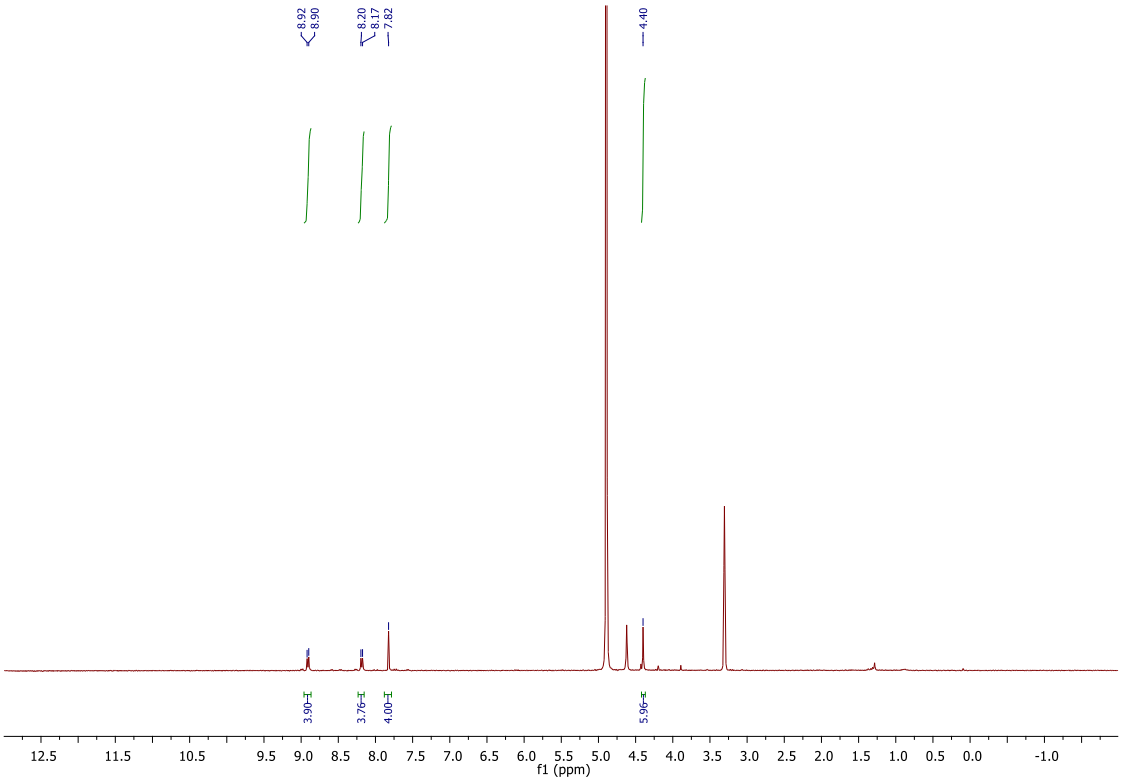

PEPyI$_2$ ^{13}C NMR

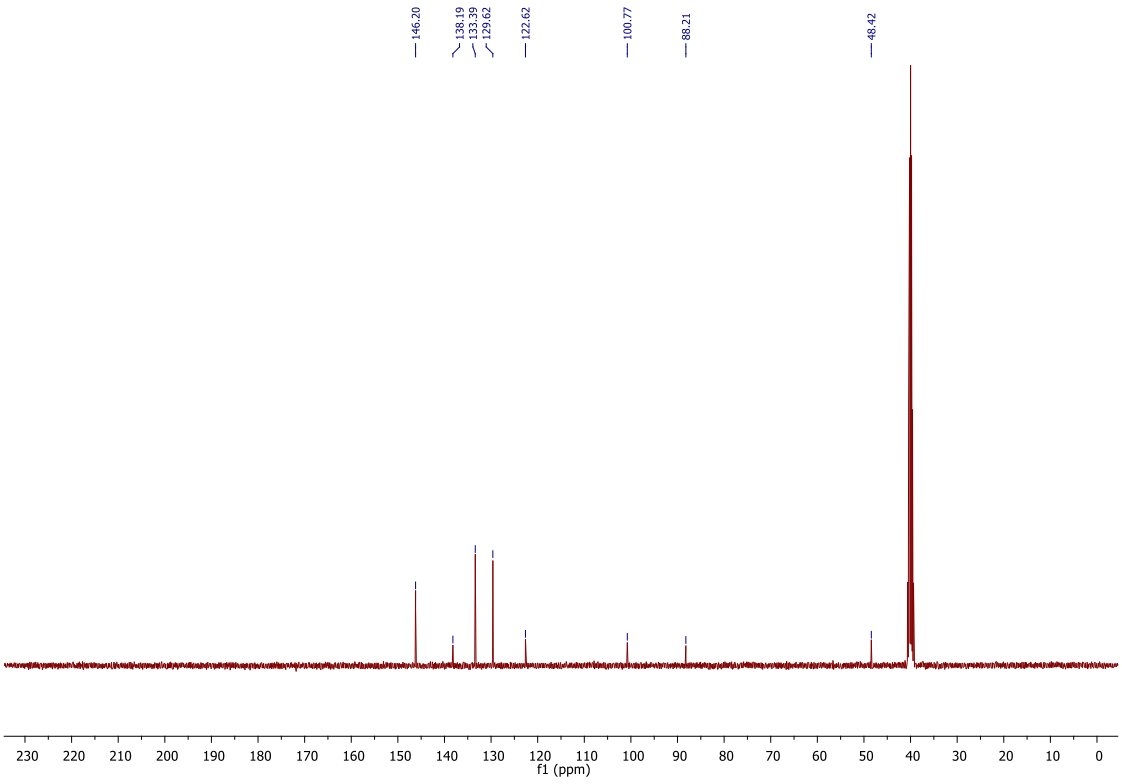

BTPyI$_3$ ^{1}H NMR

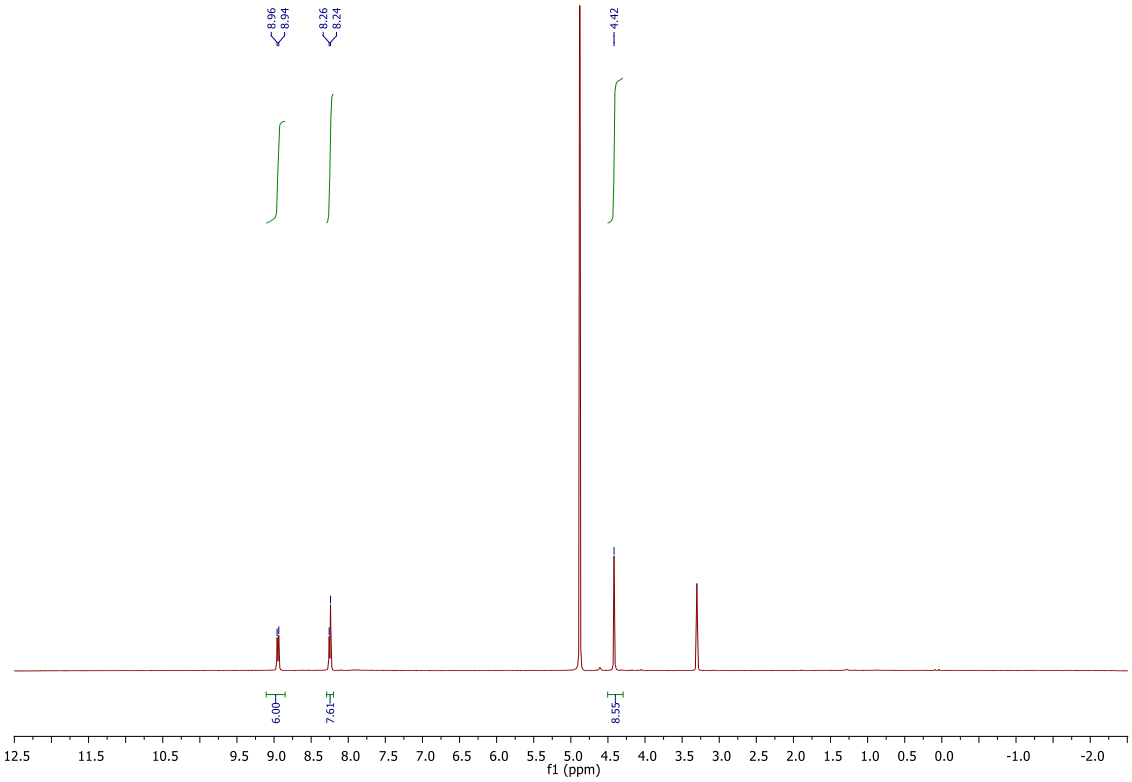

BTPyI$_3$ ^{13}C NMR

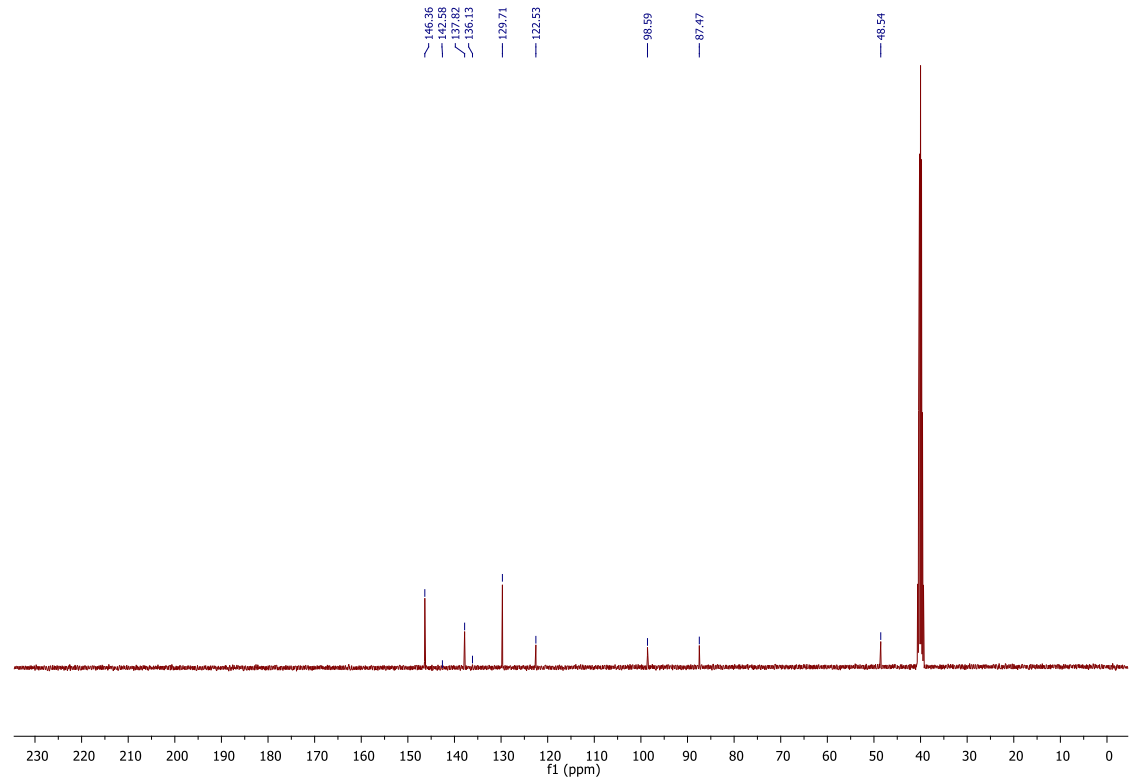

TBMPyI$_2$ ^{1}H NMR

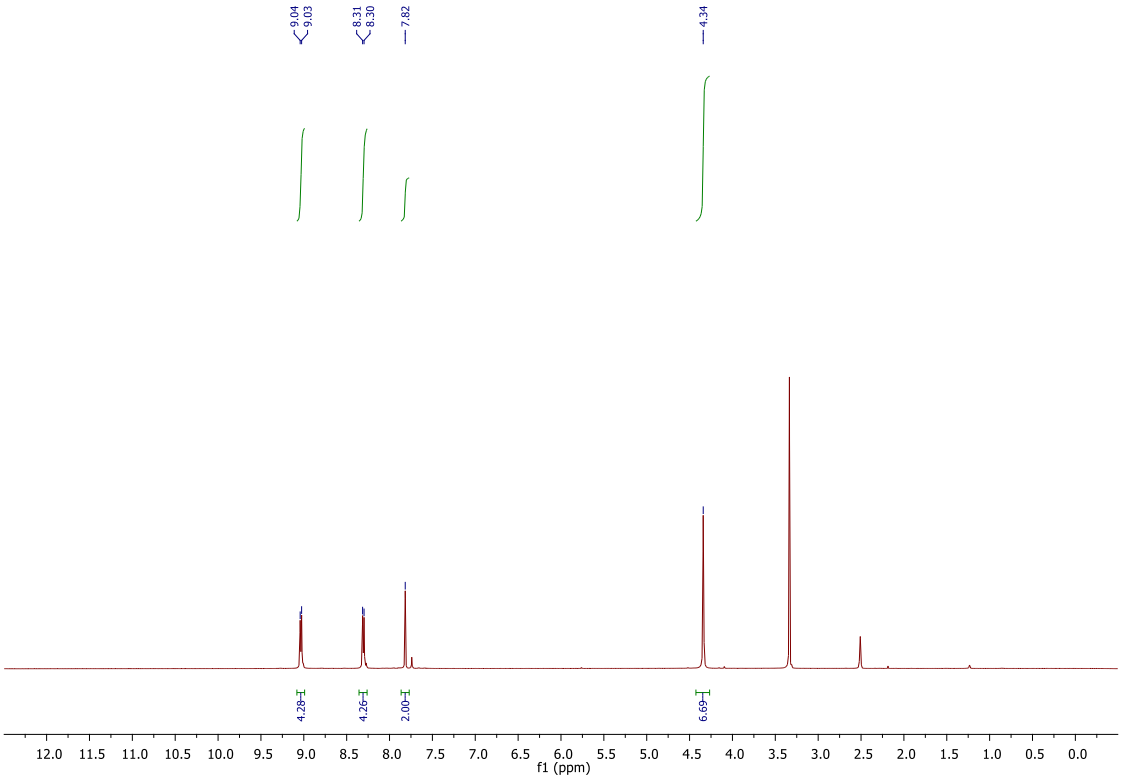

TBMPyI$_2$ ^{13}C NMR

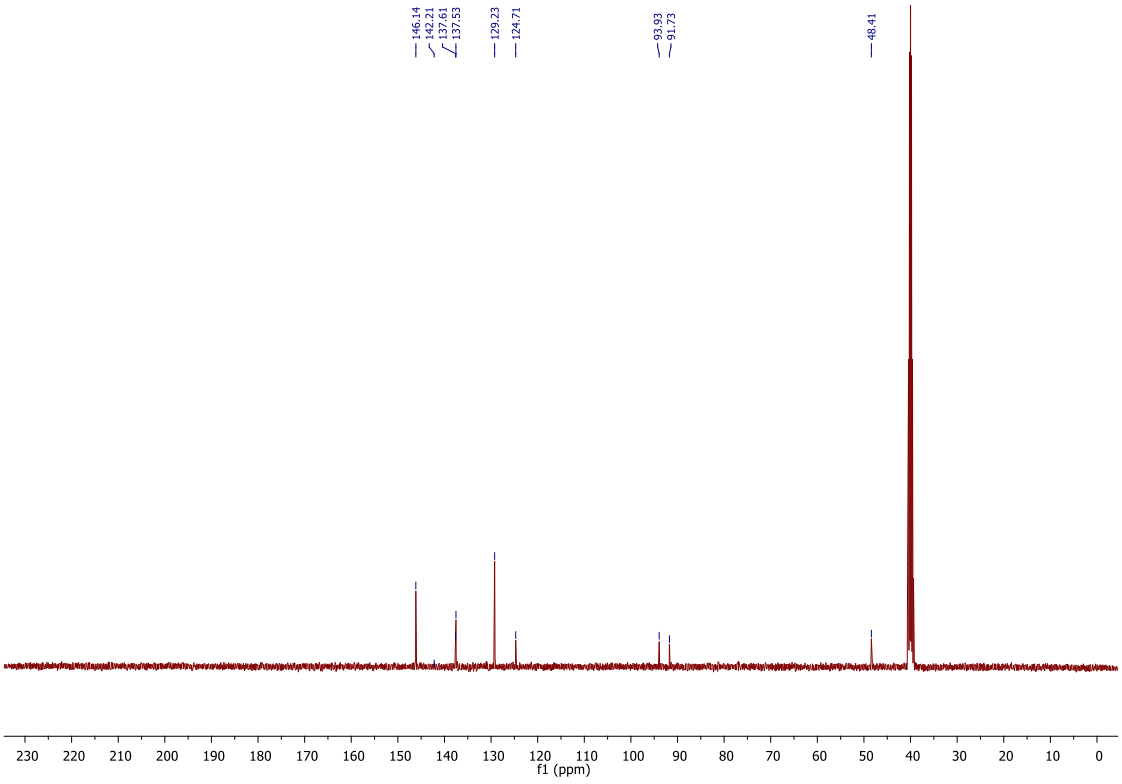

BTBMPyI$_2$ ^{1}H NMR

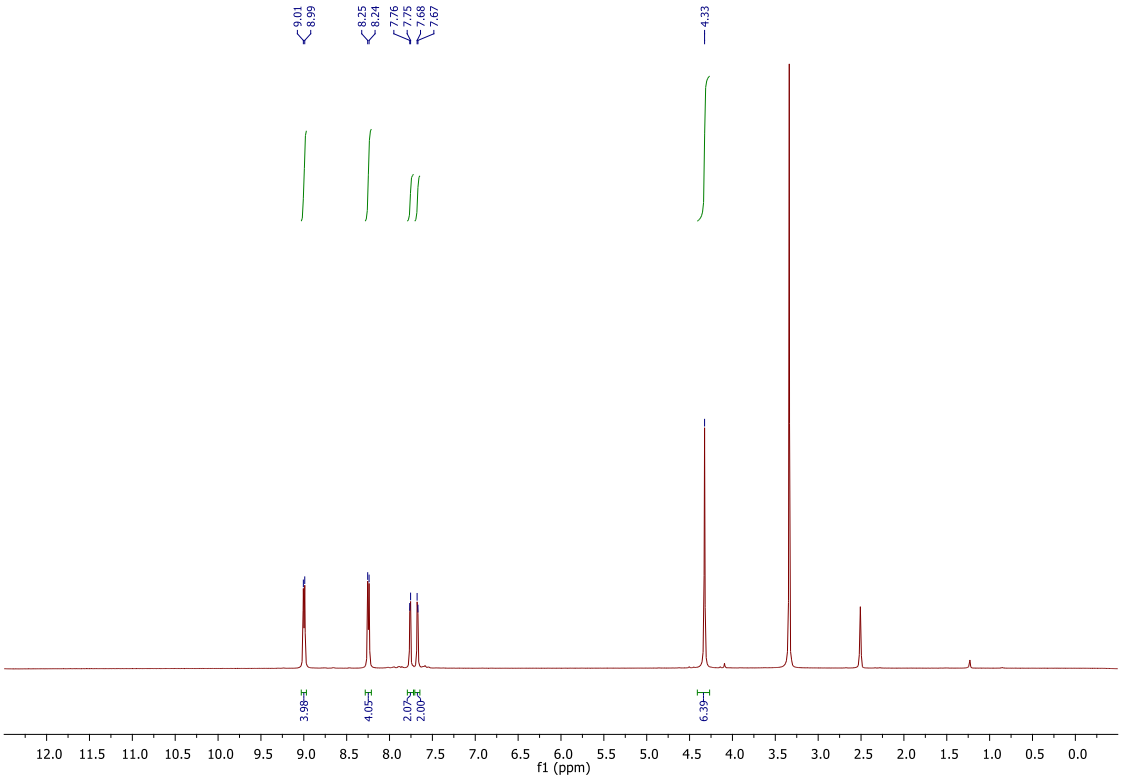

BTBMPyI$_2$ ^{13}C NMR

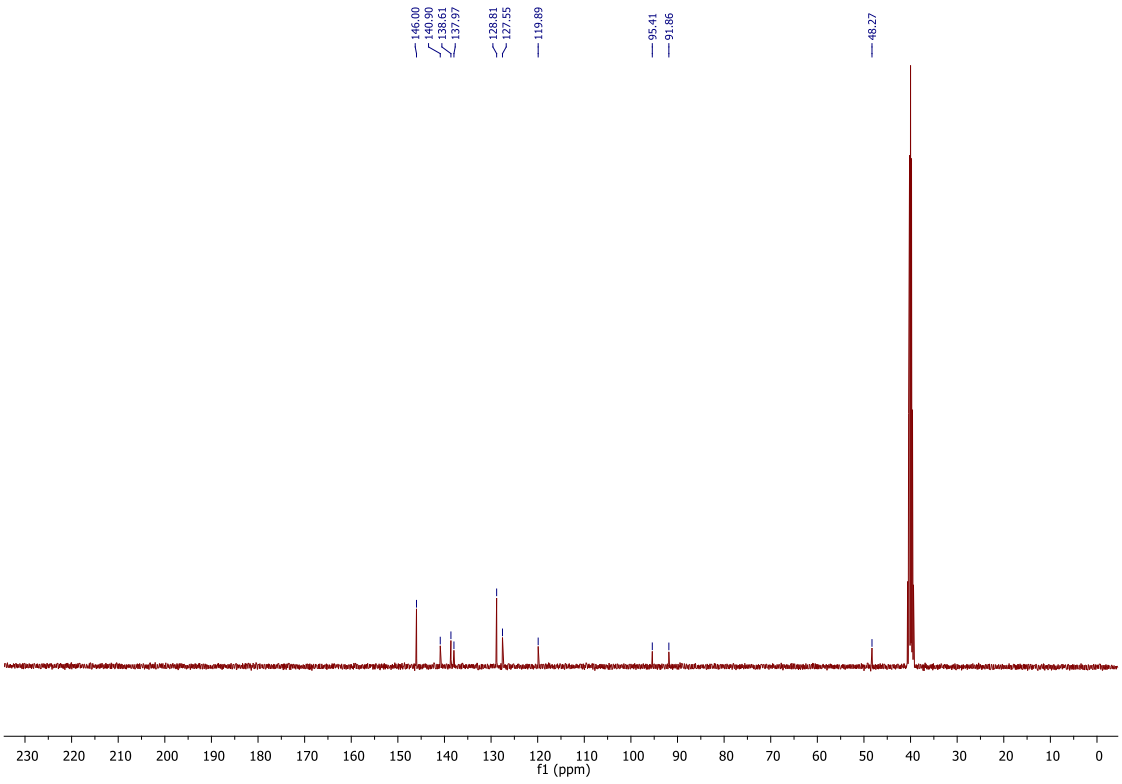

MDAPI$_2$ ^{1}H NMR

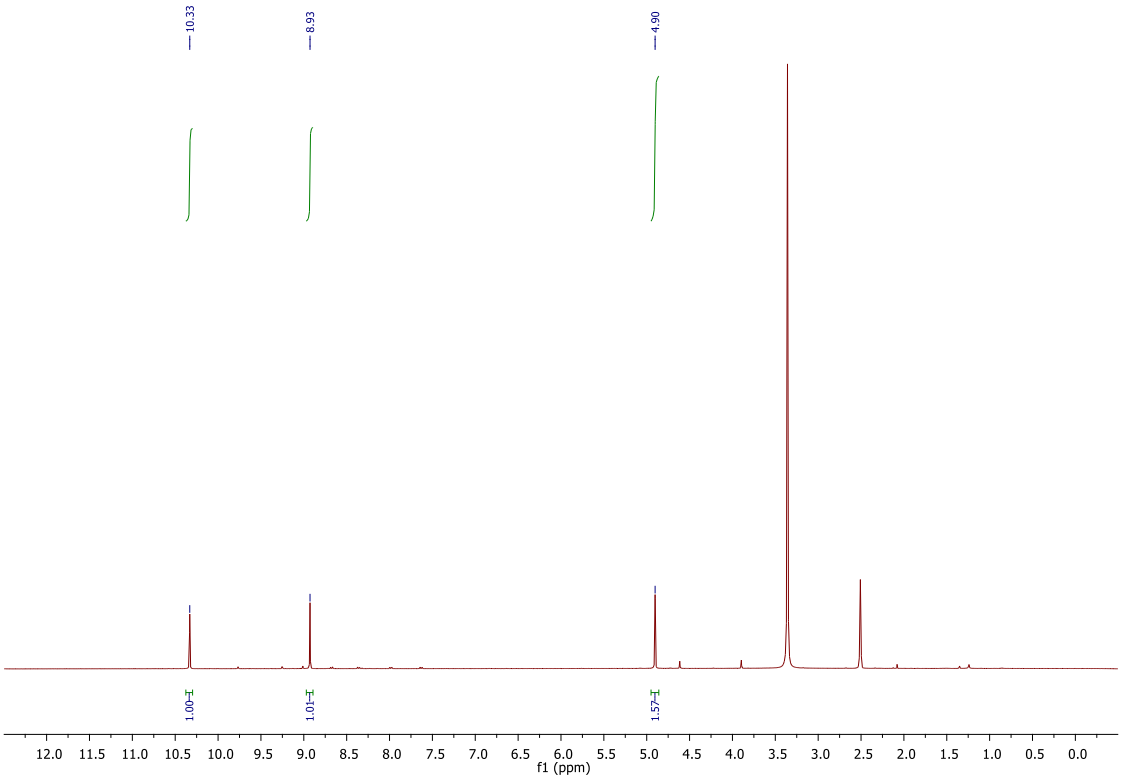

MDAPI$_2$ ^{13}C NMR

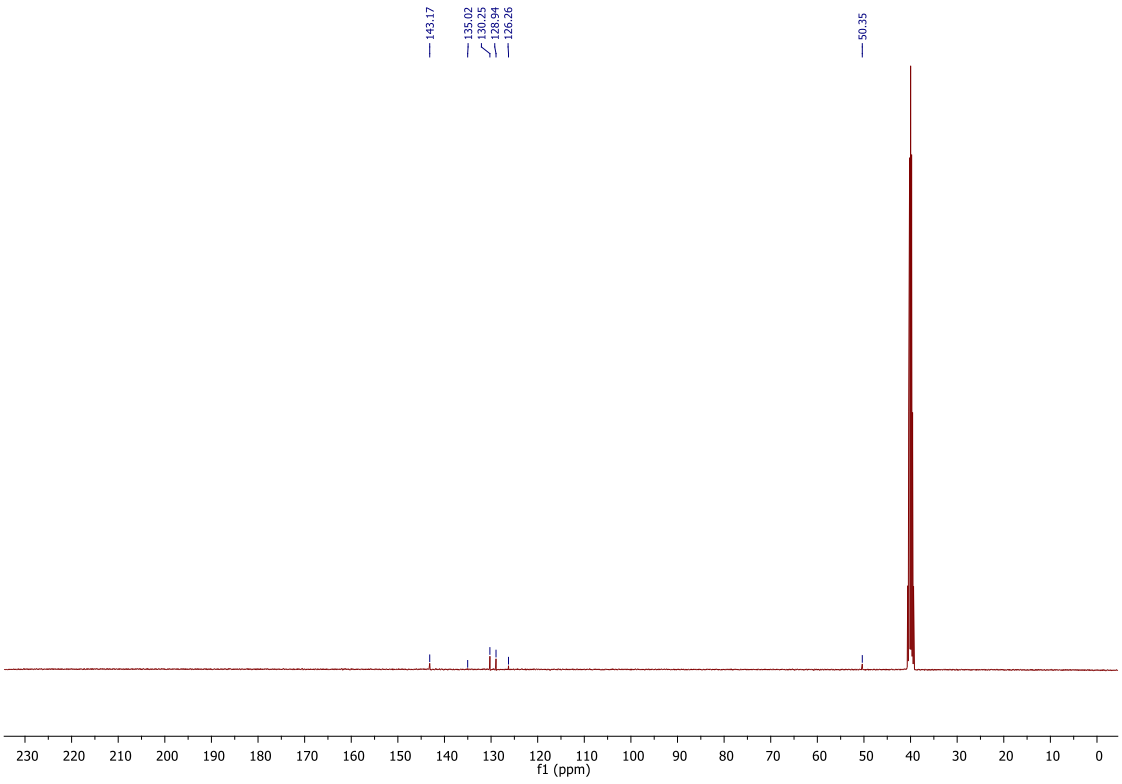

MDPPI$_2$ ^{1}H NMR

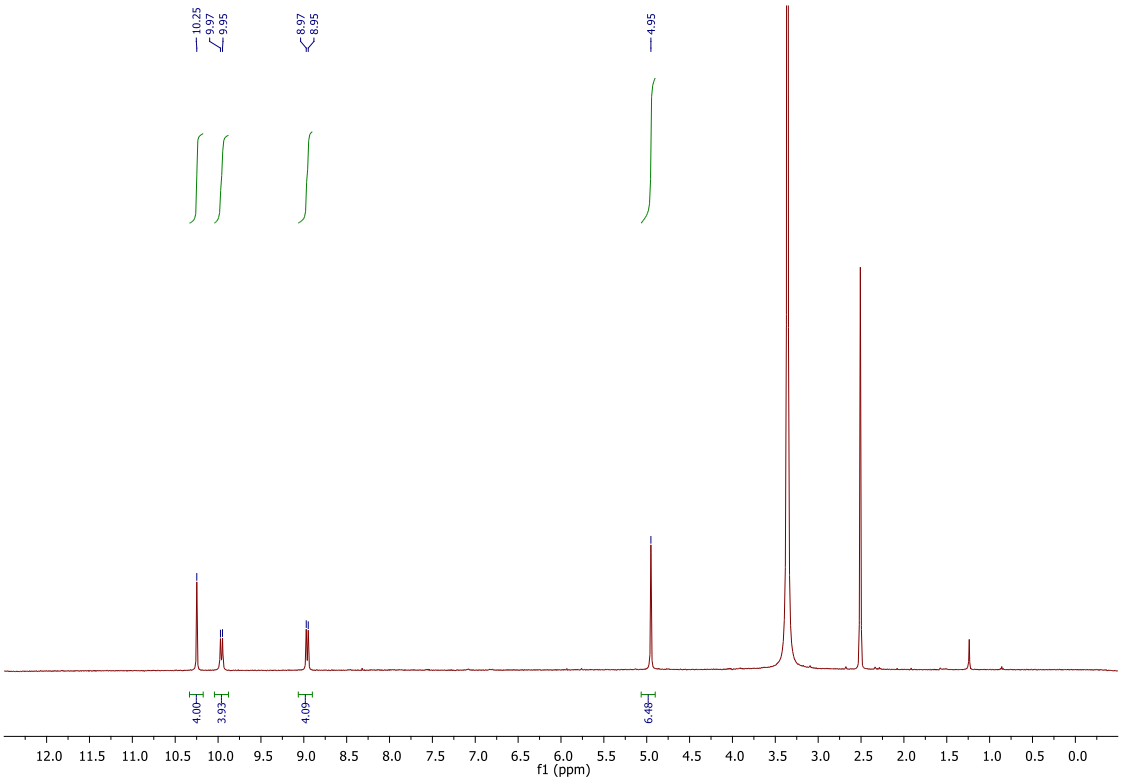

MDPPI$_2$ ^{13}C NMR